LRP 804/05 May 2005

Papers presented at the

20th IAEA Fusion Energy Conference

Vilamoura, Portugal
Novembre 1-6, 2004

ISSN 0458-5895

Table of content

Invited overview paper

Invited oral papers

Contributed papers

Progress in the Understanding and the Performance of Electron Cyclotron Heating and Plasma Shaping on TCV

J.-M. Moret 1), S. Alberti 1), Y. Andrèbe 1), K. Appert 1), G. Arnoux 1), R. Behn 1), Y. Camenen 1), S. Cirant 2), R. Chavan 1), S. Coda 1), I. Condrea 1), A. Degeling 1), B.P. Duval 1), D. Fasel 1), A. Fasoli 1), F. Gandini 2), T.P. Goodman 1), M. Henderson 1), J.-P. Hogge 1), J. Horacek 1), P.F. Isoz 1), B. Joye 1), A. Karpushov 1), I. Klimanov 1), P. Lavanchy 1), J.B. Lister 1), X. Llobet 1), J.-C. Magnin 1), B. Marletaz 1), P. Marmillod 1), Y. Martin 1), A. Martynov 1), J.-M. Mayor 1), A. Mück 1), P. Nikkola 1), S. Nowak 2), P.J. Paris 1), I. Pavlov 1), A. Perez 1), R.A. Pitts 1), A. Pochelon 1), L. Porte 1), F. Ryter 3), O. Sauter 1), A. Scarabosio 1), M. Siegrist 1), U. Siravo 1), A. Sushkov 4), G. Tonetti 1), M.Q. Tran 1), H. Weisen 1), M. Wischmeier 1), A. Zabolotsky 1), G. Zhuang 1)

1) Centre de Recherches en Physique des Plasmas, Association EURATOM - Confédération Suisse, École Polytechnique Fédérale de Lausanne, CRPP-EPFL, CH-1015 Lausanne, Switzerland
2) Istituto di Fisica del Plasma, Euratom-ENEA-CNR Association, Milano, Italy
3) Max Planck Institut für Plasmaphysik, Euratom Association, Boltzmannstrasse 2, D-85748 Garching, Germany
4) Russian Research Centre, Kurchatov Institute, 123182 Moscow, Russia

e-mail contact of main author: jean-marc.moret@epfl.ch

Abstract. Powerful ECH with an adaptable launching geometry and plasma shaping capability are exploited on TCV to create and control high performance regimes, with 3MW of 2nd and 1.5MW of 3rd harmonic (X3) and real time optimisation of the absorption by mirror feedback. Full X3 absorption with launching parallel to the resonant surface was obtained. Electron temperature profile stiffness was measured as a function of the shape up for a large range of temperature gradients and confirmed that the diffusivity is lower at negative triangularity and high elongation. The link between shear and transport was verified by interleaved modulation of co- and counter-ECCD. ECCD efficiency and fast electron generation and transport measurements demonstrate the role of transport on the driven current profile. Stationary electron ITBs were created and the role of the current profile in transport reduction was clarified by improving or destroying the barrier with a small induced electric field.

1. Introduction

Powerful electron cyclotron heating (ECH) with a highly adaptable launching geometry and plasma shaping capability make the TCV tokamak (Tokamak à Configuration Variable) a unique tool to address a number of crucial research areas for the next generation burning plasma experiments and for the improvement of the tokamak concept. One challenge for TCV is the achievement and control of high performance regimes with sustained increased energy confinement properties, exempt from macroscopic instabilities, in dominant electron heating and low collisionality to simulate the conditions generated by α-heating in a reactor plasma. Local modifications in the pressure and current distributions involving external heat and current sources together with tuning in the main plasma shape and divertor configuration are required for the creation and optimisation of these regimes. Both methods are exploited on TCV. Its ECH and current drive (ECCD) system amounts to a total power of up to 4.5MW, 3MW at the second harmonic (X2) and 1.5MW at the third harmonic (X3). The flexibility in the launching geometry, that was privileged during the design of the system, is now complemented with a real time optimisation of the wave absorption using an appropriate feedback on the mirror angles. This results in an unsurpassed power density with a precise control of the location and extent of the power deposition region that is specific to ECH systems.

This overview presents recent developments on the understanding of the plasma-wave interaction at high ECH and ECCD power level as well as studies of fundamental plasma phenomenology such as electron heat transport. Based on this knowledge significant progress in the performance of advanced operational regimes has been achieved and is also reported.

Birth distribution of the resonant fast electrons and their diffusion due to transport have been experimentally determined with perturbative techniques. These observations show that collisional diffusion in velocity space and cross-field transport operate on comparable time scales and that the latter plays a key role in determining the driven current profile and the ECCD efficiency. (Section 2.)

It was possible to extend the range of one key parameter for the electron energy transport, the normalised electron temperature gradient, by a factor four compared to the highest value obtained on other tokamaks. This was performed using off-axis heating at the high power density available. In these conditions the stiffness of the electron temperature profile and the associated heat diffusivity as a function of the plasma triangularity were investigated. It is observed that the lowest heat diffusivity is obtained with the most negative triangular shapes. (Section 3.)

The link between the local magnetic shear and the anomalous electron transport was experimentally tested by a local modulation of the plasma current profile obtained by interleaving co and counter off-axis modulated ECCD with a constant total power. The modulation in the heat diffusivity due to the change in the magnetic shear appears as a localised source term in the electron temperature dynamical response and typical signatures for such a term are observed on the amplitude and phase profile of the temperature response. (Section 4.)

Stationary electron internal transport barriers (eITB) have been created both in fully ECCD driven discharges or with a residual inductive current component using a combination of off-axis co-ECCD to broaden the current channel and centrally absorbed ECH or counter-ECCD to control the depth of the central current trough and thus the strength of the barrier. Several properties of the eITB have been studied. Its formation, observed to occur in less than 1 ms, is considerably faster than the current diffusion time and comparable to the energy confinement time. The role of the current profile in the creation of the barrier was clarified by applying to a fully ECCD driven discharge a small electric field, corresponding to a negligible ohmic power of 3 kW. This electric field, due to the electrical conductivity profile, induces a centrally peaked current density which in the counter direction further enhances the barrier strength, while in the co-direction weakens or even destroys the barrier. (Section 5.)

Third harmonic ECH opens the possibility to heat plasmas with densities above the X2 cut-off. Vertically launched X3 waves propagating parallel to the resonant surface are used and a real time optimisation of the wave absorption in which the mirror angle tracks the maximum in the absorption curve was developed. Experimental measurements of X3 absorption were performed to validate ray/beam-tracing codes and full Fokker-Planck modelling. Injecting 1.35 MW of X3-ECCD into an ELMy H-mode ohmic target gave access to a new ELM regime in which the ELM frequency is decreased and the energy released by each ELM increased by a factor 10 compared to the ohmic case. (Section 6.)

The threshold power for L to H-mode transition using X2 heating was determined at densities below the X2 cut-off. This is found to be higher than the lowest threshold obtained in ohmic

conditions at higher densities. It was also demonstrated that in these conditions, X3 heating with a similar power level can be used to assist the transition. (Section 7.)

2. Dynamics of suprathermal electron generation and transport

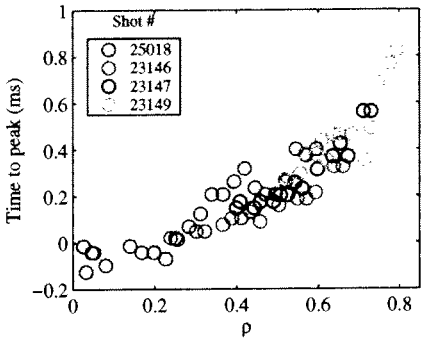

FIG. 1. Time lag from the end of a central ECCD pulse to the ECE peak, as a function of ρ_V (normalised radial coordinate proportional to the square root of the plasma volume), calculated by taking into account the estimated relativistic down-shift (plasma current 230kA, density 1.5-2.1×10^{19}m^{-3}, electron temperature 1.5keV, elongation 1.6, power 0.45-0.9MW).

The physics of ECCD is largely determined by the relaxation phenomena governing the behaviour of suprathermal electrons. In the past few years, a combination of quasi-linear modelling and direct experimental measurements in TCV has shown in particular that cross-field transport of suprathermal electrons plays a pivotal role in regulating the current profile and, in the uniquely high-power conditions of TCV, the ECCD efficiency as well [1]. In recent experiments [2] we have sought to probe the suprathermal (ECE) electron dynamics by studying the response of high field side (HFS) electron cyclotron emission to short, low duty cycle, periodic, localised ECCD pulses. The pulses are applied with one or two 0.45MW sources (with identical aiming) and are defined by a 0.2ms ramp-up, a 0.25ms flat top and a 0.1ms ramp-down, with a periodicity of 8 to 10ms. The measurement is performed with a second harmonic X-mode ECE radiometer, operating in the 78-114GHz range with 24 channels of 0.75GHz bandwidth [3], with coherent averaging applied over up to 200 pulses, resulting in a good signal-to-noise ratio in spite of a low (<40kW) average power. In order to extract quantitative information on the suprathermal population, we have employed the simple model of a bi-Maxwellian energy distribution, with uniform suprathermal temperature; this temperature can then be estimated from the relativistic shift of the spatial symmetry point of the signal distribution, as well as from equating the pulse decay time with the collisional slowing-down time. The optical thickness, thus ultimately the density, of the suprathermal population can then be derived from the radiative temperature through known formulas (note that the suprathermal population is invariably optically thin).

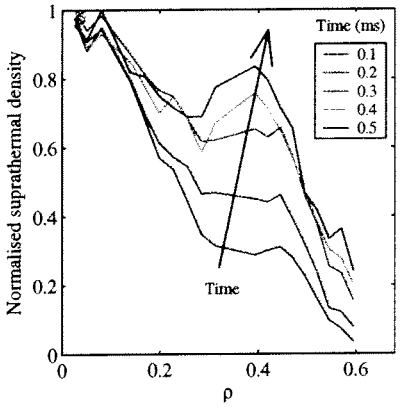

FIG. 2. Successive snapshots of normalised suprathermal density after on-axis ECCD turn-on (t = 0s).

The time to peak, calculated from the power turn-off time, is shown in Figure 1 as a function of minor radius, as a composite over several shots, with central heating in all cases. The overlapping data are in satisfactory agreement, with most of the scatter attributed to density variations. Ray tracing calculations place the ECH deposition in the region $\rho = 0-0.2$, which is confirmed by the measurements to be a region of zero delay, within the ECE time resolution of 0.05ms. The effect of radial transport on the shape of the suprathermal profile is evidenced by the successive snapshots of the normalised suprathermal density profile after power switch on, shown in Figure 2. A substantial broadening of the profile

around the deposition region is clearly observed. While quantitative details can be strongly affected by the approximations inherent in our simple model, model-independent analysis techniques, such as System Identification techniques, have also been applied in order to determine the characteristic relaxation times and the power deposition profile. Initial results suggest that the latter is anomalously broad in the presence of significant cw ECH power. Further studies are planned to test this conclusion.

3. Influence of the shape on electron temperature stiffness and thermal diffusivity

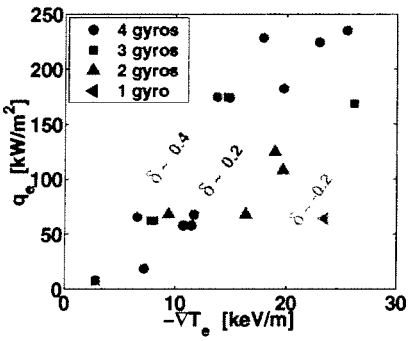

FIG. 3. Electron heat flux versus electron temperature gradient at ρ_V = 0.5 (normalised radial coordinate proportional to the square root of the plasma volume) for various triangularities.

Electron heat transport investigations have been performed in L-mode plasmas [4][5] at plasma triangularities between -0.2 and +0.4, using spatially localised central and off-axis ECH to independently vary the electron temperature, T_e and its normalised gradient, R/L_{T_e}, where $L_{T_e} = \nabla T_e/T_e$. Because of the large power density installed, an unusually large range of values for R/L_{T_e} and for the heat flux, q_e was obtained. Figure 3 shows that at constant heat flux, larger gradients and thus better confinements are generated at lower or negative triangularity, as for the case of ohmic or centrally heated plasmas [6][7]. A strong dependence of the electron heat diffusivity, χ_e on T_e is observed, Figure 4. For the three points with the lowest χ_e, the TEM are calculated to be stable. There is no such clear dependence of χ_e observed on R/L_{Te} or R/L_{ne}, in contrast to the results from local gyro-fluid simulations (GLF23) [8].

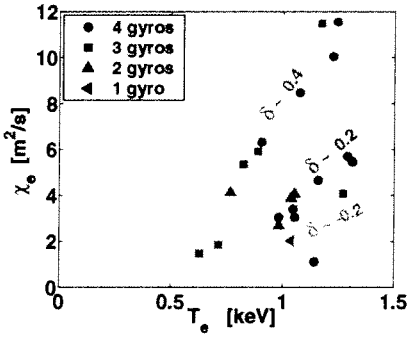

FIG. 4. Electron heat diffusivity versus electron temperature at ρ_V = 0.5 for various triangularities.

The experimental values of heat diffusivity are compared in Figure 5 to the predictions from the critical gradient model [9] for TCV and ASDEX-Upgrade. TCV data extends over a wider range of R/L_{T_e} and indicates also a strong dependence on triangularity.

The micro-instabilities responsible for the anomalous electron heat transport in these plasmas are determined using the local gyro-fluid (GLF23) and global collisionless gyro-kinetic linear simulations (LORB5). Ion temperature gradient (ITG) and trapped electron modes (TEM) are found to be unstable. The TEM are the most unstable modes, except at the lowest R/L_{T_e} values where they are stabilised and where ITG modes dominate. In all these plasmas, the high $Z_{eff}T_e/T_i$ values lead to complete stabilisation of the electron temperature gradient (ETG) modes. The plasma collisionality ν_{eff} is found to strongly reduce the electron heat transport, which is consistent with the stabilisation of TEM with increasing ν_{eff} in the simulations. However, the variation of ν_{eff} with δ in the experimental data prevents us to quantify the intrinsic dependence of χ_e on δ.

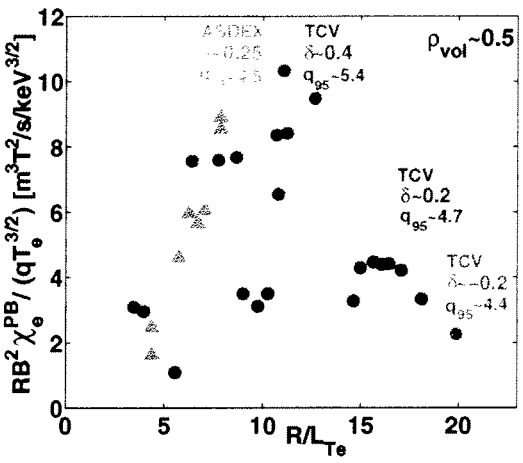

FIG. 5. Inter-machine comparison of gyro-Bohm normalised heat conductivity versus normalised temperature gradient at ρ_V = 0.5: ASDEX Upgrade (green), TCV at three different triangularities (red, blue, magenta).

4. Shear modulation experiments with ECCD

Shear-modulation experiments have been performed by using two X2 clusters of 2 gyrotrons with 0.45MW each. The launchers are oriented toroidally for driving ECCD in opposite directions, and poloidally for having an identical deposition radius, r_{dep}. The power is switched on alternatively in the two beams for driving alternate ECCD at constant instantaneous ECH heating. Modulation frequencies from 5Hz to 70Hz have been used, but the analysis is mostly performed at the lowest frequency, using Thomson scattering data. The goal of the experiment is the study of the electron transport dependence on magnetic shear.

Because the modulated ECCD is localised in a narrow layer inside a conductive medium, the electrodynamic plasma response must be taken into account in estimating the actual current distribution. A model using magnetically coupled lumped circuits is applied for calculating the modulation amplitude of the current distribution, the main effect on shear being shown in Figure 6. The estimated modulation of the current density profile and shear (±40%) is supported by the evolution of the internal inductance, by voltage-current characteristic and sawteeth behaviour.

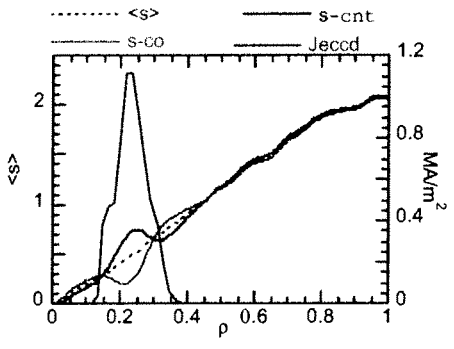

FIG. 6. Calculated magnetic shear profiles for co and counter-ECCD.

A striking feature is a strong oscillation in T_e, more than 30% peak-to-peak in the plasma core, in spite of constant input heating power. Small and negligible density oscillations are also observed, although a process different from energy confinement is acting on particles. The phase of the T_e oscillations confirms that the heat wave is generated inside r_{dep}, and propagates outwards.

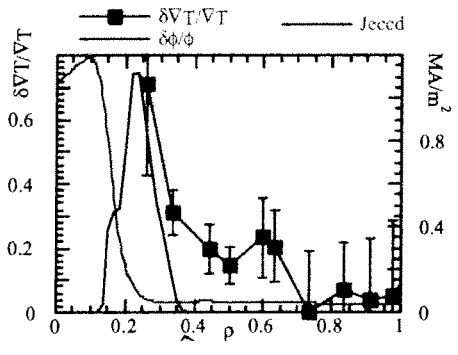

FIG. 7. Relative modulation amplitude of ∇T_e (full squares) and relative heat flux modulation amplitude (red solid line) (shot #24867).

This oscillation can be interpreted as a change either in the thermal diffusivity χ_e or in the heat flux q_e, with an associated gradient modulation expressed as $\tilde{\nabla T_e}/\nabla T_e = \tilde{q_e}/q_e - \tilde{\chi_e}/\chi_e$. The main contribution to $\tilde{q_e}$ is the modulation of the ohmic power due to modulation of the resistivity and current density. As shown in Figure 7, this modulation is very small compared to the heat flux

associated with the additional heating outside r_{dep}, while at and inside r_{dep}, the gradient modulation can only be explained by a relative modulation of 40% of χ_e. This is confirmed by a local power balance, and is consistent with the 4% increase in the global energy content, taking into account the fact that only 25% of the volume is involved and that ohmic input is decreased when T_e is increased. The thermal diffusivity modulation is in phase with that of the magnetic shear; it decreases where the shear is low, and at all internal radii. The relative modulation in χ_e is of the same order of that estimated for the shear. This provides an important information on the issue of magnetic shear damping of drift-wave, fine-scale turbulence [10].

5. Electron internal transport barrier formation and control

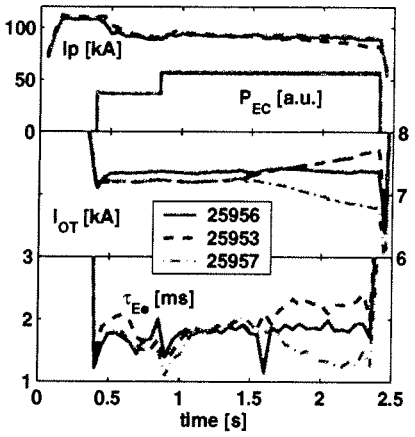

FIG. 8. Time traces of typical eITB scenarios with an inductive current perturbation in the latter phase of the discharge to probe the eITB with an additional positive or negative j_Ω contribution.

Electron internal transport barriers (eITB) have been extensively studied in the TCV tokamak, with an emphasis on steady-state scenarios. This is why the eITB presented are fully sustained by non-inductive currents, in our case by bootstrap current and ECCD. With the powerful and flexible ECCD system installed, the full plasma current can even be sustained non-inductively with off-axis beams only [11]. This allows the control of reverse shear scenarios in steady state.

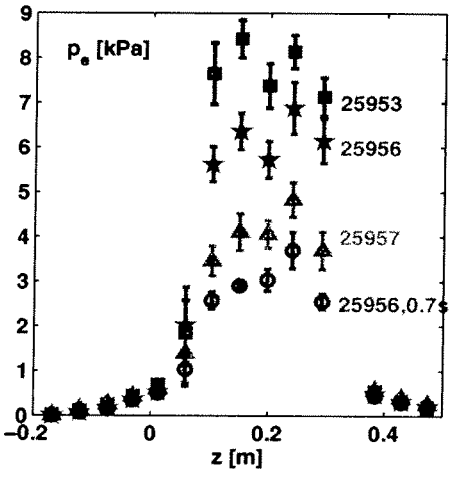

FIG. 9. Thomson scattering pressure profiles corresponding to the discharges shown in Figure 8, time-averaged in the steady-state period [1.9s,2.35s], except for the open circles, averaged over [0.6s,0.8s]

The usual scenario for our recent eITB physics studies is shown in Figure 8. First a stationary L-mode ohmic plasma is created, at low plasma current around I_p = 90kA. At 0.4s, two co-ECCD off-axis beams (0.9MW) are launched and the ohmic transformer current, I_{OT} is kept constant. Then the plasma evolves from a peaked, monotonic inductive current density profile j_Ω to a non-monotonic total profile fully sustained by j_{CD} plus j_{BS}, the ECCD and bootstrap current density profiles respectively [11]. This evolution occurs on the resistive current redistribution time, τ_{CRT} which is typically around 0.1-0.2s [12]. After that time, most of the inductive current has vanished and the safety factor, q attains a flat or reverse profile and the eITB forms rapidly, in less than 1ms [13][14]. One additional gyrotron (0.45MW) heating near the centre of the plasma is turned on at 0.8s. This enhances the eITB so that it can be clearly observed in the pressure profiles, as seen in Figure 9. Note that the global electron energy confinement time actually increases with this additional heating in the centre, Figure 8, since the power is

deposited in an improved confinement region. It can be speculated that the microinstabilities have been stabilised and thus there is no longer any power degradation in the core.

FIG. 10. Time evolution of line integrated soft X-ray emissivity of select chords of the MPX

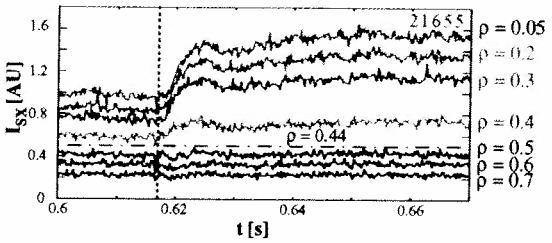

The barrier formation is best observed with the Multiwire Proportional X-Ray camera (MPX) with an appropriate high spatial and time resolution [15], Figure 10. The sudden increase in soft X-ray emissivity is dominated by an electron temperature increase. The radial location between chords with increasing and flat signals $\rho = 0.44$ corresponds to the barrier foot. The line integrated signal of chords viewing inside the barrier cannot be used to determine the effective rise time of the local temperature but the local emissivity profile may be obtained assuming a constant emissivity on a given flux surface and applying a minimum Fisher inversion method [16]. In the case shown in Figure 11, the eITB forms at $\rho = 0.3$ in a narrow region and the temperature rise then propagates rapidly inwards and outwards, with a characteristic time less than 1ms. This observation provides a unique test for validating theories on ITB.

FIG. 11. Inverted soft X-ray emissivity: a) profile snap shot plotted every 0.75ms around ITB formation; b) temporal evolution at selected radial locations.

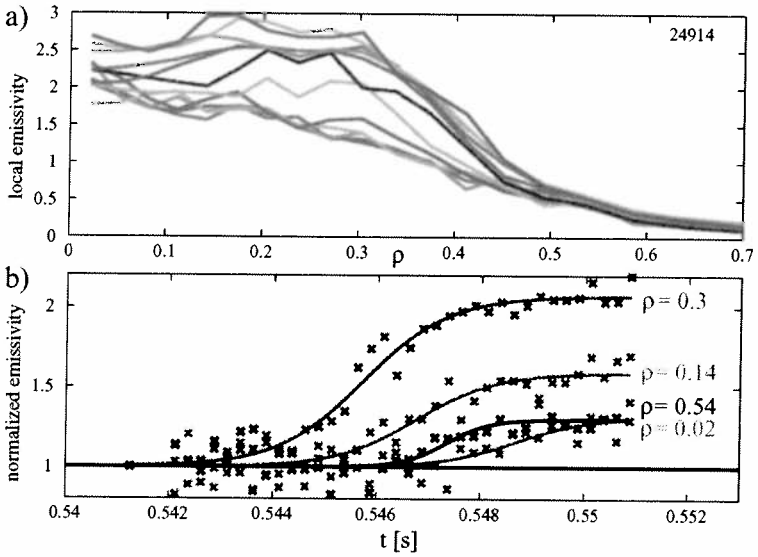

Once the discharge has reached steady-state, at 1.4s the waveform of I_{OT} is changed such that is induces a ±30mV constant surface loop voltage [17]. This drives an inductive current with a well-known profile that peaks on-axis within about one τ_{crt} and reaches steady-state in less than 1s. The additional ohmic power is negligible, ~3kW, as compared to the total EC power, 1.35MW, and even to the central ECH, 0.45MW. Then the effect of only perturbing the current profile, at constant input power can be tested. As clearly seen from Figure 8, the electron confinement time varies from ~1.4ms with +30mV and $I_p \cong 90$kA, to ~2.3ms with −30mV and $I_p \cong 70$kA. Since the total plasma current is higher with the additional inductive current, the effective confinement improvement, normalised to standard scaling laws, actually almost doubles between these two cases. This is confirmed by the pressure profiles shown in Figure 9.

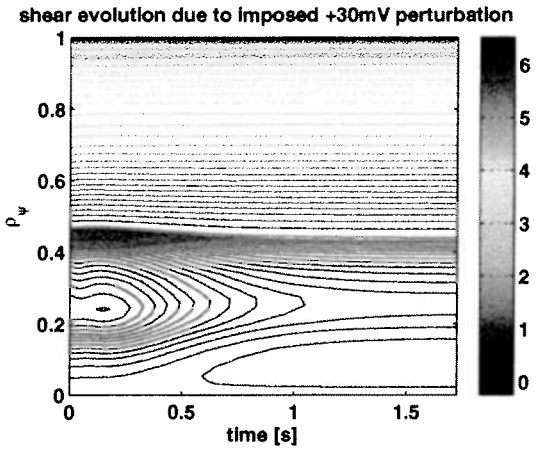

FIG. 12. Time evolution of magnetic shear due to an imposed surface loop voltage perturbation of +30mV on a plasma corresponding to the eITB discharges shown in Figure 8 at 1.4s, with V_{loop}=0 over the whole minor radius.

In Figure 12, we show the time evolution of the magnetic shear due to the addition of a loop voltage of +30mV. The ASTRA code [18] is used, keeping everything else constant, in particular the transport coefficient [12]. First the reverse shear is slightly enhanced, since the positive inductive current density perturbation comes from the edge, and then the q profile becomes essentially monotonic. This transient behaviour, which lasts about 0.1-0.2s, is actually observed with larger perturbations [19]. The final q profile is monotonic or flat with +30mV, and much more reverse with –30mV [12], corresponding to a degradation and an improvement of confinement respectively. Therefore these experiments show clearly that current profile is the primary cause for improved and anomalous electron transport in these eITB discharges. This is consistent with previous experiments where co- and counter-ECCD were added in the centre [20][21]. They are also consistent with global linear gyrokinetic simulations which show that TEM are the most unstable micro-instabilities in these discharges with $T_e \gg T_i$ and their growth rate is strongly reduced when shear decreases and becomes negative [22]. These results are also obtained with GLF23 [8], which has been used within the ASTRA code to simulate self-consistently a similar discharge. The simulations confirm that reverse magnetic shear is sufficient to form an eITB, and the bootstrap current provides a significant contribution to create and maintain the non-monotonic current profile [23]. The simulations also show that it is difficult to determine if the confinement is improved in a small region around q_{min} or in the whole core region inside the foot of the barrier, since the central ECH beam is not localised enough. In any case, it is always better to heat in the centre to maximise the bootstrap fraction and the global electron thermal energy confinement time [23].

6. Third-harmonic, top-launch ECH

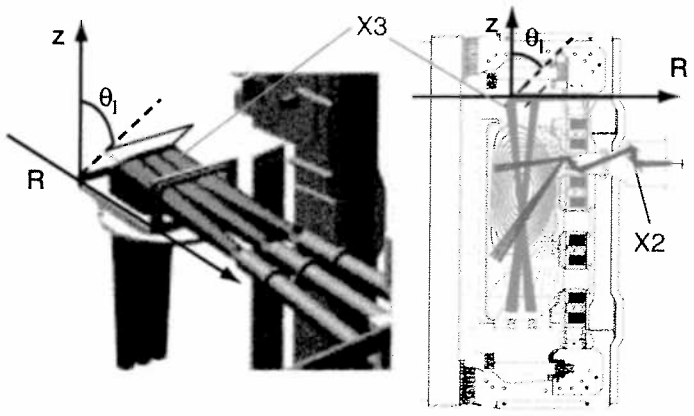

FIG. 13. View of the X3 top-launch mirror. The three RF beams are directed on one single focusing mirror with radial and poloidal steering capabilities. The poloidal angle can be controlled in real time. On the poloidal cross section, the maximum steering range is outlined in red.

In the moderate magnetic field of TCV (1.5T), the X3 system broadens the operational space with the possibility of heating plasmas at high density, well

above the cutoff density of the X2 system ($4.2\times10^{19}m^{-3}$). To compensate for the weak absorption coefficient, top-launch injection is used that maximizes the ray path along the resonance layer, sketched in Figure 13. The main characteristic of this launching scheme is the sensitivity of the absorption to the poloidal injection angle, θ as it is shown in Figure 14, where, with 0.45MW of injected power, the level of absorption is indicated by the variation of the central temperature deduced from the soft X-ray emission measurement along a central vertical viewing line [24].

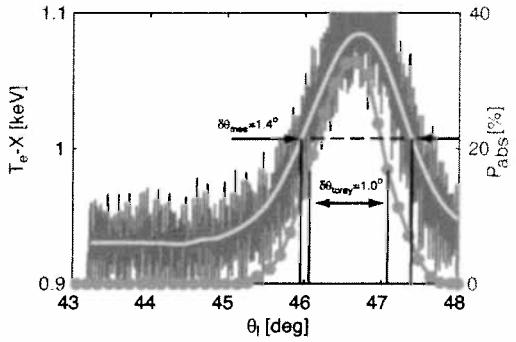

FIG. 14. Soft-X ray temperature versus poloidal injection angle θ (in blue). In red the predicted absorption calculated with the TORAY-GA code.

To maintain the maximum absorption in plasma discharges with unexpected variations of both density (refraction) and temperature (relativistic shift), a real time control of the injection angle has been developed. The feedback system consists in a synchronous demodulation of the plasma temperature response to a harmonic perturbation of the injection angle at 13Hz. This produces a feedback signal which is proportional to the actual value of $dT_e/d\theta$ and the mirror is controlled to track the maximum of the absorption curve where this derivative is zero.

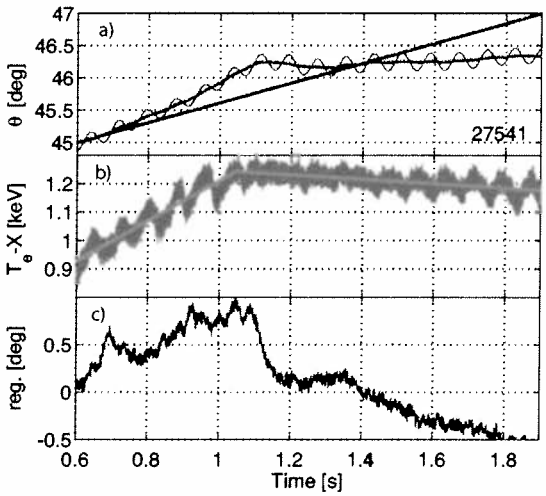

FIG. 15. a) Pre-programmed (green) and feedback controlled (red) mirror angle. b) Central plasma temperature. c) Error signal.

The capabilities of the feedback are presented in Figure 15 where the mirror poloidal angle was pre-programmed to perform a linear sweep crossing the maximum absorption. The feedback controlled mirror-angle reached the optimum angle faster than the pre-programmed sweep and then (t = 1.1s) maintained this optimum angle despite the externally imposed ramp. A stable real-time optimisation of the injection angle has been obtained on a wide variety of L-mode plasmas and further development for H-modes are presently under way.

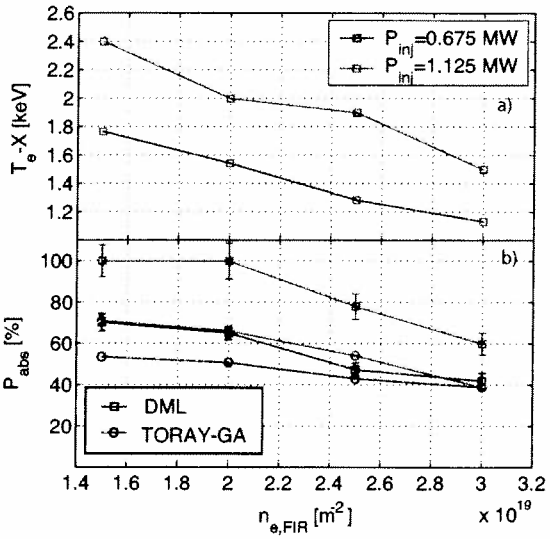

FIG. 16. a) Central temperature versus line integrated density for two levels of X3 injected power. The temperature of the ohmic target is 0.9keV. b) Absorbed fraction measured (DML squares) and predicted by TORAY-GA (circles).

The X3 absorption studies were significantly simplified with the real-time optimisation of the launcher. The absorbed fraction versus plasma density at different levels of the injected power are presented in Figure 16 with target plasma parameters: elongation 1.6, triangularity 0.1, I_p = 230kA. The absorbed power is measured using the response of the diamagnetic flux to a modulation of the injected power [25]. The difference between the measured absorbed fraction and that predicted by the TORAY-GA code is to be associated with the existence of a suprathermal population generated by the X3 wave itself. At higher electron densities this difference is lower since a fast thermalisation of the suprathermal population occurs. First comparisons between the absorption predicted by the ray tracing-code, TORAY-GA and the beam-tracing code have been made [26].

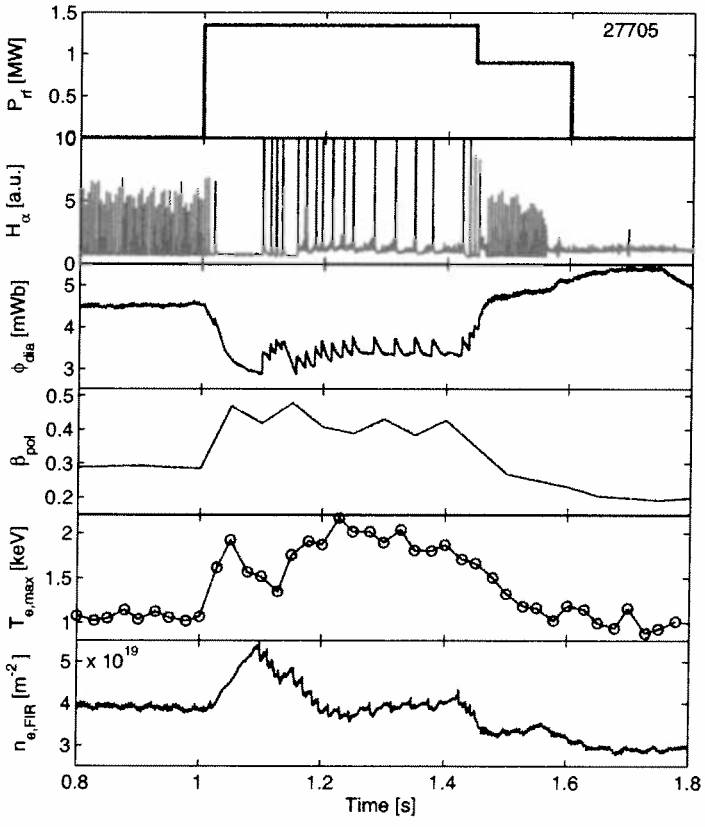

FIG. 17. Temporal evolution plasma parameters in a quasi-stationary ELMy H-mode with X3 heating, from top to bottom: injected X3 power, H_α emission, diamagnetic flux, poloidal β, central electron temperature, line averaged density.

Until X3 heating was installed on TCV the only routinely available ELMy H-modes were ohmic H-modes [27]. Initial results with low power X3 heating ($P_{X3} < P_\Omega$, where P_Ω is the ohmic power) applied to ELMy plasmas indicate that the ELM frequency decreases with increasing power but the ELM regime remains unchanged [28]. In

recent experiments $P_{X3} \cong 3P_{\Omega}$ has been obtained and the effects are significantly different. Figure 17 shows the temporal evolution of a quasi-stationary ELMy H-mode plasma heated with 1.35MW top launch X3. The ELM regime exhibits a clear transition at the application of the additional heating accompanied by a reduction in the ELM frequency and an increase by a factor 10 in the stored energy released at each ELM. At 1.42s one of the X3 gyrotrons was switched off and the plasma immediately went back to the low power regime, indicating that there is a minimum additional heating power to maintain the large ELM regime.

7. H-mode Threshold Power with ECH

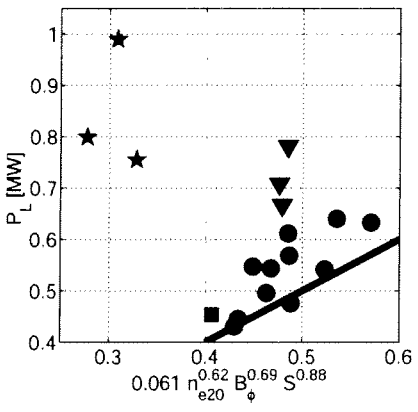

FIG. 18. LH transition power threshold for ohmic favourable (circles) and unfavourable (triangles) ion ∇B drift, X2 unfavourable (stars) and X3 favourable (square).

The LH threshold power was measured in discharges with additional ECH-X2 power. Only densities below the cut-off density were investigated. The LH transitions obtained in these conditions with an unfavourable ion ∇B drift exhibit a higher threshold power than the lowest ohmic threshold, Figure 18 (stars), in agreement with previous results showing that the threshold power increases with decreasing density below a given density [29]. The minimum in the threshold power is then located between the two groups of data. These experiments show that the threshold density can be lowered with the ECH but at the cost of more power. The TCV ECH-X3 system has a higher cut-off density, $11.5\times10^{19}\,m^{-3}$, motivating an experiment to close the gap between the ohmic and ECH-X2 data. The mirror angle was slowly tilted during the heating pulse in order to vary the total interaction volume and thus the power absorption. An LH transition occurred when the absorbed power measured using modulation on the diamagnetic flux [25] reached approximately 0.2MW (Figure 18, square). This X3-assisted LH transition was obtained at a power and a density in agreement with the ohmic LH transitions. This similarity suggests that the underlying transition physics does not depend on the heating scheme and that the increase in threshold power observed in the ECH-X2 data is a general property of the low density transitions. The minimum H-mode threshold power with favourable ion ∇B drift is 0.45MW for this particular plasma shape, at a line averaged density of $4.5\times10^{19}\,m^{-3}$.

8. Outlook

The powerful ECH system of TCV and its highly adaptable launching system are now fully deployed and have proved to be unique tools to achieve high performance regimes both in H-mode plasmas and in ITB scenarios. These capabilities can now be exploited to further optimise the performances of these plasmas and to pursue the investigations of the involved physical mechanisms in studies of fast particle generation and relaxation, heat transport and related turbulence modelling and detrimental instability mitigation.

Acknowledgment. This work was supported in part by the Swiss National Science Foundation.

References

[1] CODA, S., et al., Nucl. Fusion **43** (2003) 1361.

[2] CODA, S., et al., 30th EPS Conf. on Control. Fusion and Plasma Phys., 2003, St. Petersburg, Russian Federation, Europhys. Conf. Abstr. **27A** (2003) P-3.134.
[3] BLANCHARD, P., et al., Plasma Phys. Contr. Fusion **44** (2002) 2231.
[4] CAMENEN, Y., et al., 10th EU-US TTF Workshop, 2004, Varenna, Italy.
[5] POCHELON, A., et al., this conf., paper EX/P9-1.
[6] MORET, J.-M., et al., Phys. Rev. Lett. **79** (1997) 2057.
[7] POCHELON, A., et al., Nucl. Fusion **39** (1999) 1807.
[8] WALTZ, R.E., et al., Phys. Fluids B, **4** (1992) 3138.
[9] IMBEAUX, F., et al., Plasma Phys. Contr. Fusion **43** (2001) 1503.
[10] KENDL, A., SCOTT, B., 29th EPS Conf. on Plasma Phys. and Control. Fusion, 2002, Montreux, Switzerland, Europhys. Conf. Abstr. **26B** (2002) P-3.211.
[11] GOODMAN, T. P., et al, Nucl. Fusion **43** (2003) 1619.
[12] ZUCCA, C., et al, Varenna-Lausanne Theory Conference, 2004, Varenna, Italy.
[13] HENDERSON, M.A., et al., accepted in Phys. Rev. Lett.
[14] HENDERSON, M.A., et al, this conf., paper EX/P3-3.
[15] SUSHKOV A.V. et al., 29th EPS Conf. on Plasma Phys. and Control. Fusion, 2002, Montreux, Switzerland, Europhys. Conf. Abstr. **26B** (2002) P4-118.
[16] ANTON, M., et al., Plasma Phys. Contr. Fus. **38** (1996) 1849.
[17] GOODMAN, T. P., et al, 30th EPS Conf. on Control. Fusion and Plasma Phys., 2003, St. Petersburg, Russian Federation, Europhys. Conf. Abstr. **27A** (2003) P3-208.
[18] PEREVERZEV, G.V., et al., Max Planck - IPP Report, IPP 5/42 (1991).
[19] SAUTER, O., et al, submitted to Phys. Rev. Lett.
[20] HENDERSON, M.A., et al., Phys. Plasmas **10** (2003) 1796.
[21] HENDERSON, M.A., et al., Plasma Phys. Control. Fusion **46** (2004) A275.
[22] BOTTINO A., "Modelling of global electrostatic microinstabilities in tokamaks: effects of ExB flow and magnetic shear", PhD Thesis, 2004, École Polytechnique Fédérale de Lausanne, Switzerland.
[23] FABLE, E., SAUTER, O., Varenna-Lausanne Theory Conference, 2004, Varenna, Italy.
[24] HOGGE, J.P., et al., Nucl. Fusion, **43** (2003) 1353.
[25] MANINI, A., et al., Plasma Phys. Control. Fusion, **44** (2002) 139.
[26] ALBERTI, S., et al., this conf., paper EX/P4-17.
[27] MARTIN, Y., et al., 18th IAEA Conf. on Fusion Energy, 2000, Sorrento, Italy, paper EXP/ 5-30.
[28] PORTE, L., et al., 19th IAEA Conf. on Fusion Energy, 2002, Lyon, France, paper EX/P5-15.
[29] FIELDING, S.J., et al., Plasma Phys. Control. Fusion **38** (1996) 1091.

EX/9-1

Effect of Plasma Shape on Electron Heat Transport in the Presence of Extreme Temperature Gradient Variations in TCV

A. Pochelon, Y. Camenen, R. Behn, A. Bortolon, A. Bottino, S. Coda, B.P. Duval, E. Fable, T.P. Goodman, M.A. Henderson, A.N. Karpushov, J.-M. Moret, A. Mück, E. Nelson-Melby, L. Porte, O. Sauter, A. Scarabosio, G. Zhuang and the TCV Team 1),
F. Ryter 2)
1) Centre de Recherches en Physique des Plasmas CRPP EPFL
Association EURATOM-Confédération Suisse
CH-1015 Lausanne, EPFL, Switzerland
2) Max-Planck-Institut für Plasmaphysik, EURATOM-IPP Association, Garching, Germany

e-mail contact of main author: Antoine.Pochelon@epfl.ch

Abstract. Electron heat transport experiments are performed in L-mode discharges at various plasma triangularities, using radially localised electron cyclotron (EC) heating to vary the normalised electron temperature gradient R/L_{Te} (where $1/L_{Te}= \nabla T_e/T_e$) and the electron temperature T_e over a large range. Local gyro-fluid (GLF23) and global collisionless gyro-kinetic (LORB5) linear simulations allow the determination of the unstable micro-instabilities. Ion temperature gradient (ITG) and trapped electron (TE) modes are found unstable. TE modes are the most unstable modes, except at the lowest R/L_{Te} values where they are stabilised and ITG modes dominate. High $Z_{eff}T_e/T_i$ values lead to a complete stabilisation of the electron temperature gradient (ETG) modes. Experimentally, a strong dependence of the electron heat diffusivity χ_e on T_e is observed. No such clear dependence of the heat diffusivity χ_e is observed on R/L_{Te} or R/L_{ne}, in contrast to results from GLF23 simulations. The electron heat transport is reduced with triangularity. However, this effect can be partly, or totally, attributed to an increase in the plasma collisionality, leading to a stabilisation of TE modes.

1. Introduction

Plasma shape is one of the fundamental parameters in a tokamak that strongly influences plasma properties and performance, placing also strong constraints on technological and construction choices in machine design. Increasing the elongation allows higher plasma current and also influences other operational limits such as the pressure [1,2] and density limits [3]. The triangularity and elongation have a strong influence on the core stability, e.g. sawteeth [4], and edge plasma, in particular on H-mode pedestal and ELMs [5,6].

This paper addresses the issue of the role of plasma shape on the energy confinement, focusing on the role of triangularity on the *local* electron heat transport properties in electron temperature gradient variation experiments using localised electron cyclotron (EC) power deposition. *Global* confinement studies in Ohmic [7-9] and in central EC heated L-mode plasmas [10,11] showed the beneficial role of low or negative triangularity on the electron energy confinement time. This result is in contradiction with similar studies of the influence of triangularity on H-mode confinement, where the confinement time was observed to increase with plasma triangularity [5,6], due to the contribution of the edge pedestal. Triangularity also strongly modifies the ELM stability [12]. The use of L-mode plasmas should help minimise the influence of the edge features on global confinement, allowing a more direct study of the genuine effect of plasma shape on core local electron heat transport. A better understanding of transport dependence on plasma shape may also provide ways of influencing the access to eITB regimes. Such studies have commenced elsewhere with an H-mode edge, with the strong influence of ELM activity [13,14].

The specificity of the present study [15-17] lies in: 1) the comparatively large range of both *normalised electron temperature gradients* $R/L_{Te}=R\,\nabla T_e/T_e$ [18,19], and *electron temperatures* explored, by changing respectively the radial EC power distribution and the total EC heating power; 2) the study of the influence of plasma shaping, in particular the

triangularity δ, which is varied from D- to inverse-D-shape. In addition, a third parameter, the plasma *collisionality*, plays a significant role. While the first two parameters are operationally controlled, the third parameter may not always be controlled.

2. Electron temperature gradient variation and temperature variation experiments

2.1. TCV and EC system: The TCV tokamak (R_o = 0.88 m, a < 0.255 m, B_T < 1.54 T, $I_p \leq$ 1 MA) has been designed to investigate the effects of plasma cross-section shaping. Plasma edge triangularity -0.7 < δ < 1 and elongation 0.9 < κ < 2.8 have been achieved [9]. The auxiliary heating relies on EC waves at the 2nd harmonic (X2) and 3rd harmonic (X3) frequencies. The X2 EC waves are produced at 82.7 GHz by six gyrotrons delivering a total nominal power of 3 MW and are coupled to the plasma from the low field side (LFS), using six launchers independently steerable during the discharge [20].

2.2 Plasma discharges and experimental conditions: The experiments are performed in a moderately elongated L-mode plasma, κ = 1.6, in a limiter configuration. The electron transport has been studied at three plasma triangularities, δ = -0.2, +0.2 and +0.4, while the plasma current I_p and the toroidal magnetic field B_T are kept constant (I_p = 220 kA and B_T = 1.44 T), resulting in a slight safety factor variation q_{95} from 4.4 to 5.5 (δ=-0.2, +0.4 respectively). Cross-field electron heat transport is investigated by depositing up to 1.8 MW X2 EC power in the plasma to vary the normalised electron temperature gradient R/L_{Te} and by distributing the power at two different radial locations: one "central", at a deposition radius of ρ_1 = 0.35, just outside the q = 1 surface $\rho_{q=1}$, and one far off-axis at ρ_2 = 0.7. The normalised radius is defined as ρ = sqrt(V/V_{LCFS}), where V and V_{LCFS} are the volumes delimited by the flux surface labelled by ρ and by the last closed flux surface, respectively.

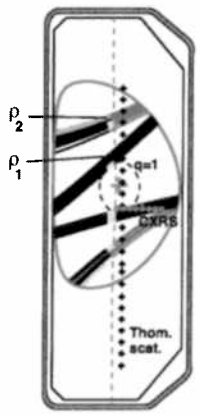

FIG. 1. ECH at two different deposition locations and line of sight of relevant diagnostics

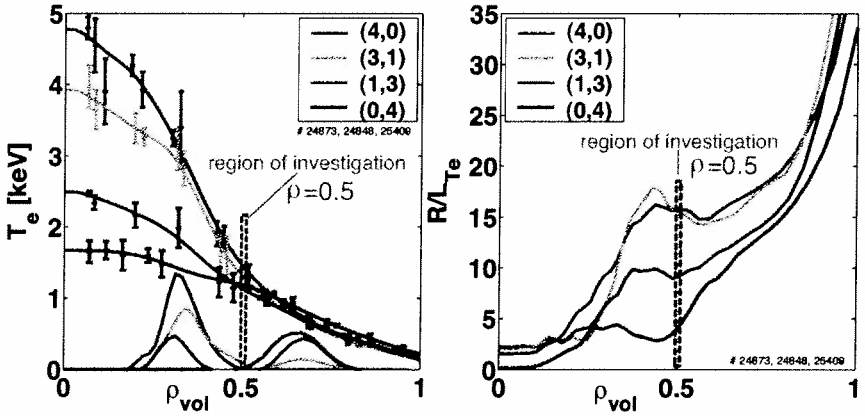

FIG. 2a. Electron temperature profile variations obtained at constant edge heat flux when changing the EC power deposition locations from central to far off-axis, for a triangularity δ=0.2. The numbers in parenthesis represent the nb. of EC beams deposited ("centrally", far off-axis), 0.45MW per beam.
FIG. 2b. Corresponding variations - up to a factor of 4 - of the normalised temperature gradient R/L_{Te}.

The central density range is fixed such as to avoid excessive refraction of the EC beams and to ensure full single pass absorption for the far off-axis deposition (1.5 < n_{eo} < 2.7×10^{19} m^{-3}). The width of the EC beams, narrow compared to the plasma minor radius, leads to radially localised EC power deposition. The EC power deposition width at half maximum $\Delta\rho_{EC}$ never exceeds 0.1 and the power absorption from the linear ray tracing code TORAY-GA [21]

always exceeds 95%. A poloidal view of the plasma cross-section and EC wave launch is shown in FIG. 1, for a case with simultaneous central and far off-axis EC power deposition.

Thomson scattering, essential for this study, measures the electron temperature T_e and density n_e every 25 ms along the full plasma height with a spatial resolution of 4.5cm, typically 2×8 points in a full profile. Profile information is only used after steady state of the current profile is reached, that is when reaching stationary internal inductance l_i, and then averaged over 12 measurements (~ 300ms).

2.3 Electron temperature profile and discharge response: Varying the amount of EC power deposited at ρ_1 only, from 0.45 to 1.8 MW, does not change the shape of the T_e profile plotted on a logarithmic scale, and R/L_{Te} only varies by 10% in the confinement region. This behaviour, already observed in several tokamaks, is known as profile stiffness [18]. To change the value of R/L_{Te}, far off-axis distribution of part or total EC power is needed, e.g. following the scheme developed in ASDEX Upgrade to study electron heat transport as a function of the normalised electron temperature gradient [19]. Far off-axis EC power deposition leads to low R/L_{Te} values whereas central deposition leads to high R/L_{Te} values. Intermediate R/L_{Te} values are achieved by sharing the deposited EC power centrally and far off-axis. Keeping the total EC power constant, the variation of R/L_{Te} can be obtained at constant electron heat flux at the plasma edge, q_e^{edge}, without large changes of the electron temperature at the investigation radius, ρ=0.5. FIG. 2a shows the variation of the T_e profile, from peaked to flat, when changing gradually the EC power distribution from fully central to far off-axis. This variation is obtained at constant edge T_e, as q_e^{edge} is kept constant. The corresponding R/L_{Te} profiles exhibit a factor of 4 variation in the region delimited by the two power deposition locations $\rho_1 < \rho < \rho_2$, typically at ρ=0.5, FIG. 2b. Varying the total EC power also permits electron temperature variations at constant R/L_{Te}.

In these experiments, cross-field electron heat transport is studied by calculating the electron thermal diffusivity χ_e defined by $q_e = -n_e \chi_e \left\langle |\nabla\rho|^2 \right\rangle \frac{\partial T_e}{\partial \rho}$, where the brackets indicate averaged over the flux surface. As a linear relation between the electron heat flux q_e and the electron temperature gradient ∇T_e is assumed, the effects of off-diagonal terms in the transport matrix are not included. The electron heat flux is calculated in steady-state taking into account the contributions of the Ohmic power, the localised EC power deposited at ρ_1 and ρ_2, and the power transferred by the electrons to the ions. A radially uniform loop voltage is assumed for the calculation of the Ohmic power and the EC power is obtained from TORAY-GA. The ion temperature profile, needed to estimate the power transfer to the ions, is obtained from Charge Exchange Recombination Spectroscopy (CXRS, see FIG. 1). The power balance is strongly dominated by the EC power, which allows, by changing the EC power distribution, for a large variation of q_e between ρ_1 and ρ_2, while keeping constant q_e^{edge}. The low plasma density results in a low equipartition power flow from electrons to ions and a high T_e/T_i ratio. The radiated power P_{rad} measured by XUV-bolometer photodiodes never exceeds 20% of the total power P_{tot}. Moreover, the ratio P_{rad}/P_{tot} remains below 5% for ρ<0.8 and may be neglected in the region of investigation $\rho_1<\rho<\rho_2$.

The sawtooth activity present in these discharges confirms the expected deposition location as just outside $\rho_{q=1}$: the sawtooth period increases (sawtooth stabilisation) while increasing the power deposited at ρ_1, from 2-3ms in Ohmic to above 10ms with the total EC power. The observed sawtooth stabilisation indicates deposition just outside $\rho_{q=1}$ [22], confirming the TORAY ray tracing calculations. ASTRA transport calculations, using the experimental power balance heat conductivity χ_e^{PB}, the density and geometry, and assuming neoclassical conductivity and current profile steady-state conditions, yield a q-profile, without

the assumptions of a particular radial heat transport model [23]. The location of $\rho_{q=1}$ ranges from 0.28 to 0.34, FIG. 3, and, at the powers used, $\rho_{q=1}$ is always present. Since stationary conditions are required for diagnostics and transport analysis purposes, the imposed temperature profile variations produce asymptotic current profile changes (l_i is modified) [24]. The toroidal rotation velocity profile, measured form CXRS of C^{6+}-lines, is non-monotonic in Ohmic discharges [25], with a maximum close to $\rho_{q=1}$. Power deposition outside q=1, e.g. at mid-radius, further peaks the central velocity profile increasing the velocity shear in the core.

3. Micro-instabilities

Local gyro-fluid (GLF23 [26]) and global collisionless gyro-kinetic (LORB5 [27]) linear simulations indicate the micro-instabilities potentially responsible for anomalous heat transport in these experiments. Ion temperature gradient (ITG) and trapped electron (TE) modes are found to be unstable. TCV data are depicted in the stability diagram, FIG. 4, which shows that TE modes are generally the most unstable, except at the lowest R/L_{Te} values where they stabilise and ITG modes dominate. The dashed lines indicate the pure TE threshold for a fluid model [28]. In all these EC dominated plasmas, the high values of $Z_{eff}T_e/T_i$, a parameter determining the electron temperature gradient (ETG) mode threshold [29], leaves the ETG modes stable (R/L_{Te} is 50% of the threshold at mid-radius ρ=0.5).

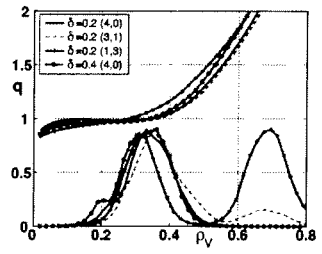

FIG. 3. q profiles from ASTRA with different EC power distribution (norm. to 0.9) and δ.

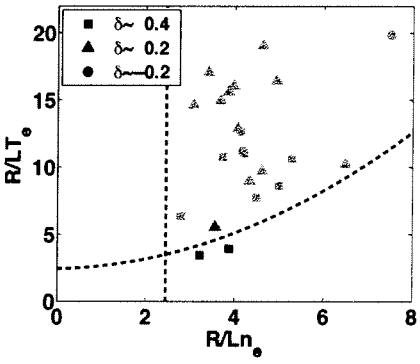

FIG. 4. Experimental values at mid-radius of the driving gradients for TE modes, R/L_{Te} and R/L_{ne}. From GLF23 simulations, TE modes are most unstable (yellow), except for the lowest values of R/L_{Te}, where ITG modes are most unstable (blue). The dashed lines indicate the pure TE mode threshold for a fluid model.

The ranges of the different relevant parameters at the investigation radius (ρ=0.53) for different power deposition distributions, total power and for two triangularities δ=0.2 and 0.4, is given in the following table (f_t: trapped particle fraction, ν_{eff}: collisionality [32], $s = \frac{r}{q}\frac{dq}{dr}$):

T_e [keV]	T_i [keV]	T_e/T_i	f_t	R/L_{Te}	R/L_{Ti}	R/L_{ne}	$n_{e19}\,Z_{eff}$	ν_{eff}	q	s
0.6–1.3	0.2–0.5	2-4	0.54–0.55	4-20	3.5-6.5	3-7.5	3.4-11.5	0.25-0.8	1.5-1.9	1.1-1.6

4. Inter-machine comparison within heuristic transport model

The "heuristic" model developed by Imbeaux and co-workers [30,31] has the form:

$$\chi_e = \chi_0 + \lambda\, q\, T_e^{3/2} (R/L_{Te} - R/L_{Te}^{crit})\, H\,(R/L_{Te} - R/L_{Te}^{crit}),$$

where q is the safety factor, λ and R/L_{Te}^{crit} are coefficients to be adjusted, H is the Heaviside function, with the possibility of specifying different exponents for the $T_e^{3/2}$ and (R/L_{Te} - R/L_{Te}^{crit}) terms. To test the dependencies of this model against TCV data, the electron heat diffusivity in the gyro-Bohm normalised form is plotted against R/L_{Te} in FIG. 5a. ASDEX Upgrade data have been added for comparison. While ASDEX Upgrade data show a clear offset linear dependence on R/L_{Te}, the three different triangularities in TCV exhibit different levels of transport. A saturation of the diffusivity is observed at δ=0.2 and high R/L_{Te}. The experimental T_e and R/L_{Te} ranges are shown in FIG. 5b. This broad two-dimensional range

may be the cause of the larger spread of TCV data in FIG. 5a, implying that the dependences on $T_e^{3/2}$ or R/L_{Te} may not be adequate.

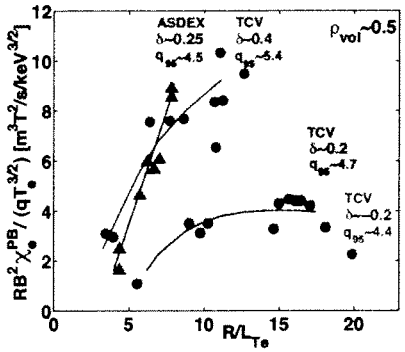

FIG. 5a. Inter-machine comparison of normalised heat conductivity (gyro-Bohm) versus normalised temperature gradient: ASDEX Upgrade (triangles), TCV at three different triangularities (circles).

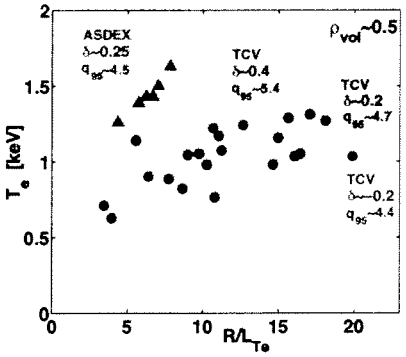

FIG. 5b. Range of data used in FIG 5a, showing that TCV data occupy a wide range in the T_e-R/L_{Te} space.

5. χ_e dependencies: experiment, heuristic modelling

We concentrate on plasma configuration with triangularity δ=0.4, suggested by the observed constancy of n_eZ_{eff} (see FIG. 10). Plotting the heat diffusivities against the driving terms of the TE modes (R/L_{Te}, R/L_{ne}) in FIG. 6a,b, we observe that χ_e globally tends to increase with R/L_{Te}, but that for a fixed value of the driving terms, χ_e exhibits large variations. These two parameters are therefore not sufficient to explain the variation of χ_e. Surprisingly, T_e alone appears to be a more adequate variable to describe the variation of χ_e, FIG. 6c. The diffusivity χ_e shows a strong dependence on T_e with little scatter despite the large range of R/L_{Te} and R/L_{ne} explored. In fact, the trend of χ_e to increase with R/L_{Te} can be attributed to the correlation of T_e and R/L_{Te} shown in FIG. 5b. The experimental observation of a strong χ_e-dependence on T_e does not exclude a weak dependence of χ_e on R/L_{Te} or R/L_{ne}, but is in contrast to the results from GLF23 simulations, which indicate a clear χ_e-dependence on R/L_{Te} or R/L_{ne}. Note that in FIG. 6c, the two lowest χ_e points are not TE, but ITG mode dominated.

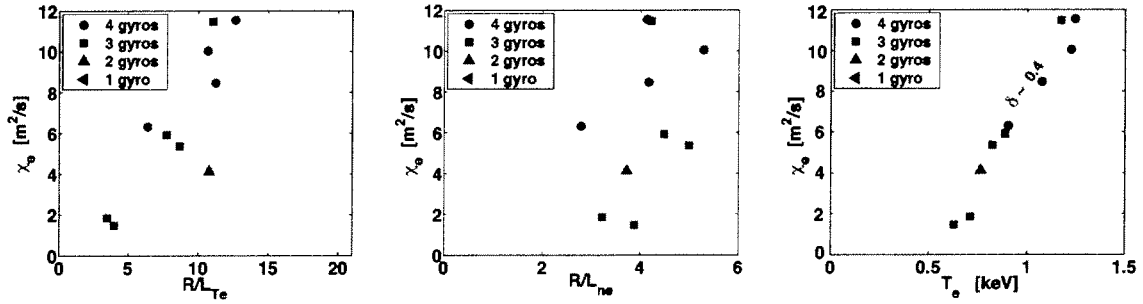

FIG. 6a,b,c. Plotting the dependence of the electron heat diffusivity at δ=0.4 data against different variables at nearly constant n_eZ_{eff} (see FIG. 10). No clear dependence of χ_e is found on R/L_{Te}, FIG. 6a, or R/L_{ne}, FIG. 6b. A strong dependence on T_e, however, is observed, FIG. 6c.

We compare different forms of the model with the aim of specifying a better form for the heuristic critical gradient model for the diffusivity χ_e and heat flux q_e [30,31]. The most standard form:

$\chi_e \sim T_e^{3/2}(R/L_{Te}-R/L_{Te}^{crit})$, with a heat flux as $q_e \sim n_eT_e^{5/2}(R/L_{Te}-R/L_{Te}^{crit})R/L_{Te}$

or a non-linear form in R/L_{Te}, suggested by the weak dependence of χ_e on R/L_{Te} visible in Fig. 5a and FIG. 6:

$\chi_e \sim T_e^{3/2}(R/L_{Te}-R/L_{Te}^{crit})/R/L_{Te}$, with a heat flux as $q_e \sim n_e T_e^{5/2}(R/L_{Te}-R/L_{Te}^{crit})$.

TCV data, for the diffusivities (FIG. 5a) as well as for the heat fluxes (FIG. 7), are better represented by the second, non-linear formulation.

6. TCV data at different shapes and collisionalities

The heat fluxes at different triangularities follow a linear law as a function of R/L_{Te} or of ∇T_e, FIG. 8. A heat flux threshold above which the heat flux is enhanced is suggested from the diagram. This representation clearly shows a beneficial effect of reducing triangularity for a given q_e. Plotting χ_e versus T_e, for different triangularities, FIG. 8, also demonstrates the beneficial role of reducing the triangularity (an extension of the diagram of FIG. 6c).

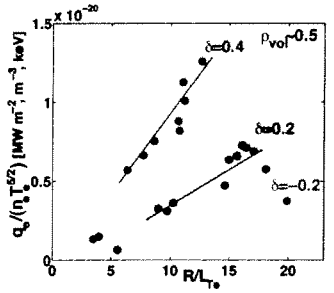

FIG. 7. Test of the heat flux dependence on R/L_{Te}. It suggests a linear dependence of q_e on R/L_{Te} rather than a quadratic one.

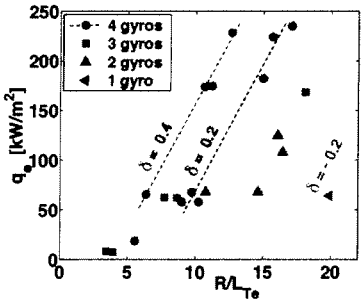

FIG. 8. A large range of heat fluxes q_e and normalised gradients R/L_{Te} are explored at different triangularities. At constant heat flux, larger gradients are generated at lower triangularity.

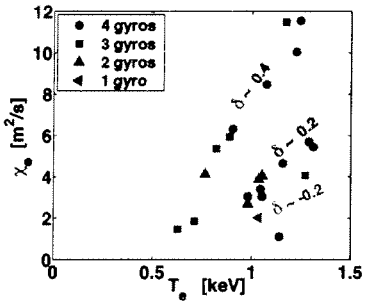

FIG. 9. Electron heat diffusivity versus electron temperature, showing a clear step-linear dependence for δ=0.4

The dependence on triangularity of the local electron heat transport is similar to the global confinement time dependence of centrally heated discharges reported earlier [10,11]. This trend can further be illustrated in the present study with "central" (i.e. just outside $\rho_{q=1}$) and far off-axis deposition by the confinement enhancement factor H_{98L}, FIG. 10, which increases when 1) the triangularity is reduced, and 2) the power is deposited the closest to the magnetic axis. FIG. 11 shows that the parameter $n_e Z_{eff}$ determining the collisionality ($\nu_{eff} \sim 0.1\, R n_e Z_{eff}/T_e^2$, see [32]) is relatively constant for all the δ=0.4 data, which were used to find the

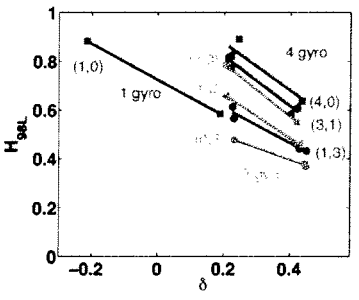

FIG. 10. Confinement enhancement factor for different deposition location and total power

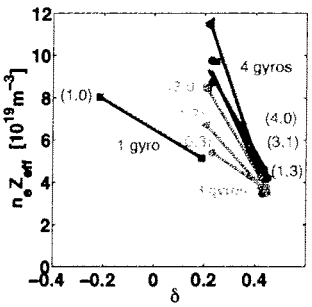

FIG. 11. Variation of $n_e Z_{eff}$ with triangularity.

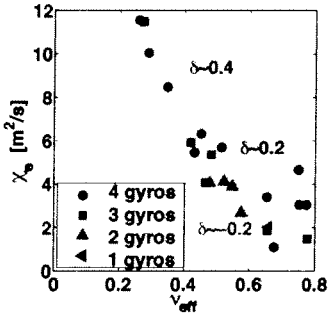

FIG. 12. Plasma collisionality ν_{eff} reduces strongly χ_e.

regression of FIG. 6c. Plotting all the χ_e data versus collisionality, FIG.12, reveals a possibly crucial role of collisionality in this transport study, where shape, heat deposition location and total heat flux are varied independently. The electron heat transport is found to decrease strongly with plasma collisionality ν_{eff}, which is consistent with the stabilisation of TE modes while increasing ν_{eff} in GLF23 simulations. However, the strong data correlation of ν_{eff} with δ and temperature prevents us from establishing the dependence of χ_e on δ and ν_{eff} independently.

To test whether theory predicts an influence of plasma shape on TE mode micro-instability-driven transport, simulations were performed using the linear collisionless gyrokinetic code LORB5. Measured experimental profiles at a single triangularity, δ=0.2, have been maintained while the triangularity was varied. FIG. 13a and b show that the spatial distribution of the convective cells is affected by the change of plasma triangularity. Growth rate and transport (estimated by mixing-length arguments) both increase slightly with triangularity, FIG. 14, in the same direction as the experiment, particularly in the toroidal mode number range $15<n<25$. The effect is however too small to demonstrate a significative effect of shape, here triangularity, on the TE mode growth rate and transport.

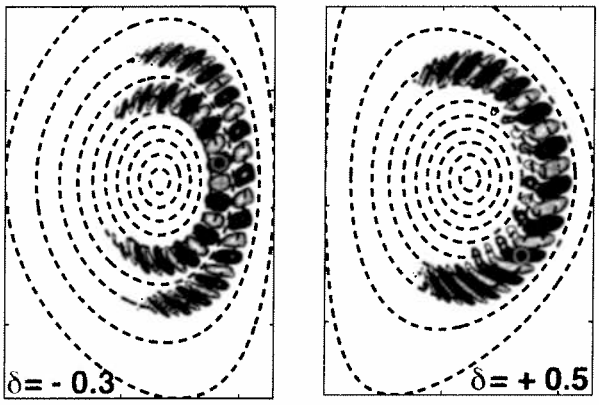

FIG. 13a,b. Poloidal cross-section of the electro-static potential for a TE mode at δ=-0.3 (a), and δ=0.5 (b). The spatial structure changes with triangularity.

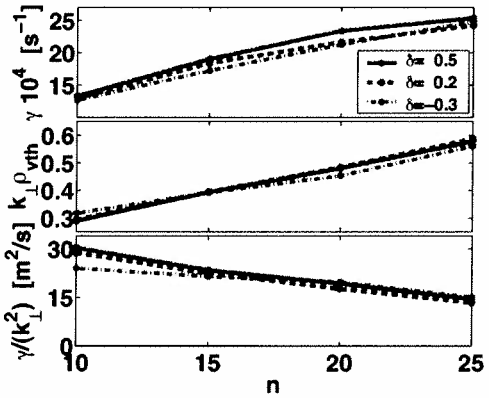

FIG. 14. TE mode growth rate γ, normalised radial extension, mixing length transport vs. toroidal mode number, indicating a slight increase of transport quantities at high positive δ.

7. Discussion and conclusions

The present TCV experiments involve imposed variations of plasma triangularity. The value of n_eZ_{eff}, hence collisionality, was found to undergo important changes while varying plasma triangularity. Whether the dependence of n_eZ_{eff} on triangularity is an issue of plasma-wall interaction or an issue of particle transport through the last closed surface remains open. It was noted however that a higher gas injection is required in TCV in highly positive triangularity plasma to maintain a constant density, which could explain a lower n_eZ_{eff}.

In addition to triangularity variations, variations in both power deposition distribution *and* total power, allow discriminating between the effects of R/L_{Te} and T_e, an extension over experiments at constant total power in which R/L_{Te} and T_e remain correlated. The experimental data suggest a saturation of χ_e at high R/L_{Te} and a linear dependence of the normalised heat flux $q_e/n_eT_e^{5/2}$ on R/L_{Te}, providing more information for a heuristic model and supporting recent simulations obtained elsewhere [33]. Note that a saturation of χ_e with R/L_{Te} had already been predicted earlier for ITG modes [34]. A clear dependence of χ_e on T_e is observed at all triangularities. In TCV data, χ_e is found to decrease with the triangularity.

However, the triangularity effect on χ_e can be explained by the variation of collisionality, which plays a determining role in stabilising TE modes. From the linear collisionless gyrokinetic LORB5 results, χ_e is not expected to vary significantly with triangularity.

This work was partially supported by the Swiss National Science Foundation.

Acknowledgements: The authors would like to acknowledge fruitful discussions with C. Angioni and L. Villard.

References

[1] TROYON, F., et al., Plasma Phys. Controlled Fusion **26** (1984) 209.
[2] HOFMANN, F., et al., Phys. Rev. Lett. **81** (1998) 2918.
[3] GREENWALD, M., et al., Nucl. Fusion **28** (1988) 2199.
[4] REIMERDES, H., POCHELON, A. et al., Plasma Phys. Contr. Fusion **42** (2000) 629.
[5] STOBER, J. et al., Plasma Phys. Control. Fusion **42** No 5A (May 2000) A211.
[6] SAIBENE, G., SARTORI, R., et al., Plasma Phys. Control. Fusion **44** (2002) 1769.
[7] WEISEN, H., et al., Nucl. Fusion **37** (1997) 1741.
[8] MORET, J-M., et al., Phys. Rev. Lett. **79** (1997) 2057.
[9] HOFMANN, F., et al., Plasma Physics and Controlled Fusion, **43** (2001) A161.
[10] POCHELON, A., GOODMAN, T.P., HENDERSON, M.A., et al., Nucl. Fusion **39**, No.11Y (1999) 1807.
[11] POCHELON, A., et al., Proc. of 26th EPS Conf. on Controlled Fusion and Plasma Physics, Maastricht, June1999, ECA Vol. **23J** (1999) 1089.
[12] BECOULET, M., HUYSMANS, G., SARAZIN, Y., et al., Plasma Phys. Controlled Fusion **45** (2003) A93.
[13] CRISANTI, F., LOMAS, P., TUDISCO, O. et al., Plasma Phys. and Controlled Fusion **45** (2003) 379.
[14] RIMINI, F.G., BECOULET, M., et al., this conference, EX/P3-11.
[15] CAMENEN, Y., POCHELON, A., et al. IAEA TM on ECRH, Klosterseeon, July 2003, Germany.
[16] POCHELON A., CAMENEN, Y., RYTER, F., CODA, S., EU-TTF Topical meeting on electron transport, February 19-20 2004, Milano, Italy.
[17] CAMENEN, Y., POCHELON, A., et al., 10th EU-US TTF Workshop, Sept. 6-9, 2004, Varenna, Italy.
[18] RYTER, F., et al., Plasma Phys. and Controlled Fusion **43** (2001) A323.
[19] RYTER, F., TARDINI, G. et al., Nucl. Fusion **43** (2003) 1396.
[20] GOODMAN, T.P., ALBERTI, S., HENDERSON, M.A., POCHELON, A., TRAN, M.Q., 19th Symp. on Fusion Technology, Lisbon, Portugal, 1996, Vol. **I** (1996) 565.
[21] MATSUDA, K., IEEE Trans. on Plasma Sci. **17** (1989) 6.
[22] ANGIONI, C., GOODMAN, T.P., et al., Nucl. Fusion **43** (2003) 455.
[23] FABLE, E., SAUTER, O., Theory of Fusion Plasmas, 30 Aug. – 3 Sept. 2004, Varenna, Italy.
[24] POCHELON, A., ARNOUX, G., CAMENEN, Y., SCARABOSIO, A., ALBERTI, S., et al., 19th IAEA FEC, Lyon 2002, IAEA-CN-94/EX/P5-14.
[25] SCARABOSIO, A., et al., 46th Ann. Meeting of the Div. of Plasma Physics, APS, Savannah 2004.
[26] WALTZ, R.E., STEABLER, G.M., et al., Phys. of Plasmas **4** (1997) 2482.
[27] BOTTINO, A. et al., Phys. of Plasmas **11** (2004) 198.
[28] NORDMAN, H., WEILAND, J., et al., Nucl. Fusion **30** (1990) 983.
[29] JENKO, F., et al., Phys. of Plasmas **8** (2001) 4096.
[30] IMBEAUX, F., RYTER. F., GARBET, X., Plasma Phys. and Controlled Fusion **43** (2001) 1503.
[31] GARBET, X., et al., Plasma Phys. and Controlled Fusion **46** (2004) 1351.
[32] ANGIONI, C., et al., Physics of Plasmas **10** (2003) 3225.
[33] PEETERS, A., et al., subm. for publication, 2004.
[34] FIVAZ, M., PhD EPFL Thesis No.1692 (1997), Lausanne Report LRP 582/97.

Assessment of Plastic Flow and Fracture Properties with Small Specimens Test Techniques for IFMIF-Designed Specimens

P. Spätig 1), E. N. Campitelli 2), R. Bonadé 1), N. Baluc 1)

1) Fusion Technology-Materials, CRPP EPFL, Association EURATOM-Confédération Suisse, 5232 Villigen PSI, Switzerland
2) Laboratory for Materials Behavior, Nuclear Energy and Safety Research Department, 5232 Villigen PSI, Switzerland

e-mail contact of main author: philippe.spatig@psi.ch

Abstract. The primary mission of the International Fusion Material Irradiation Facility (IFMIF) is to generate a material database to be used for the design of various components, for the licensing and for the assessment of the safe operation of a demonstration fusion reactor. IFMIF is an accelerator-based high-energy neutron source whose irradiation volume is quite limited (0.5 l for the high fluence volume). This requires the use of small specimens to measure the irradiation-induced changes on the physical and mechanical properties of materials. In this paper, we developed finite element models to better analyze the results obtained with two different small specimen test techniques applied to the tempered martensitic steel F82H-mod. First, one model was used to reconstruct the load-deflection curves of small ball punch tests, which are usually used to extract standard tensile parameters. It was shown that a reasonable assessment of the overall plastic flow can be done with small ball punch tests. Second, we investigated the stress field sensitivity at a crack tip to the constitutive behavior, for a crack modeled in plane strain, small-scale yielding and fracture mode I conditions. Based upon a local criterion for cleavage, that appears to be the basis to account for the size and geometry effects on fracture toughness, we showed that the details of the constitutive properties play a key role in modeling the irradiation-induced fracture toughness changes. Consequently, we suggest that much more attention and efforts have to be paid in investigating the post-yield behavior of the irradiated specimens and, in order to reach this goal, we recommend the use of not only tensile specimens but also that of compression ones in the IFMIF irradiation matrices.

1. Introduction

The aggressive irradiation environment of a fusion reactor will lead to very specific material problems. These problems have been continuously addressed but many challenging issues remain to be solved in order to operate a power generating fusion reactor. Indeed, while important progresses in physics of fusion plasma have been accomplished, efforts are still necessary to better understand the irradiation effects on all the identified material candidates but also on the materials under development that will be close to the neutron flux escaping the burning plasma. These materials will undergo severe neutron fluence resulting in significant neutron-induced changes in their chemical, physical and mechanical properties. Up to now, the material fusion research community has made extensively use of fission neutron irradiation, e.g. [1,2] and/or accelerator facilities [3] to investigate the effects of irradiation on materials. As a matter of fact, the overall fusion material development has been guided by the results of irradiations whose neutron spectra do not reflect that of a fusion reactor environment. The maximum neutron energy available from a fast reactor is about 2 MeV only, leaving open all the issues related to the irradiation damage produced by the high energy neutron range of the fusion spectra, which reaches 14 MeV resulting from the deuteron-triton reactions. One specific issue related to the fusion neutron spectrum is the production of gaseous impurities (helium and hydrogen isotopes) in the material bulk simultaneously with the creation of atomic displacement damage. The extended exposures of the first wall of DEMO reactor will produce about 20 displacment per atoms per full power year (dpa/FPY), 180 atom parts per million of helium per FPY (appm/FPW) and 709 hydrogen appm/FPY [4]. Despite all the material fusion development based on the great deal of irradiation data collected over the years from fission neutron sources and accelerator based facilities, the limits of employing these types of irradiation have been identified. First, the results and conclusions obtained from a given neutron spectrum can be transferred only up to some extend to that of the fusion reactor. For instance, the effect of the correct ratios of He/dpa and H/dpa along with the appropriate primary recoil spectrum on the irradiation-

induced changes can certainly not be properly inferred from fission neutron spectra or any other irradiation experiment. Second, there will be always an intrinsic issue of reliability as long as no experimental validation has been performed to prove the validity of the data transfer. As a consequence, there is a fundamental need to build an intense high energy neutron source to serve, on the one hand, as a tool for fundamental investigations on the current material candidates as well as for the development of new and emerging materials and, on the other hand, to qualify materials for the design, the construction and the operation of a demonstration reactor.

2. The International Fusion Material Irradiation Facility

The details of the International Fusion Materials Irradiation Facility (IFMIF) design, the description of its major components and a discussion of its suitability for fusion materials research can be found in [5]. We briefly summarize hereafter the main characteristics of the facility. The neutrons are produced by stripping the protons from two 40 MeV deuteron beams in a liquid lithium target through the nuclear reactions $^{7}Li(d,2n)^{7}Be$, $^{6}Li(d,n)^{7}Be$. This choice is mediated by the desire to reproduce as close as possible the irradiation damage conditions occurring in the first wall and breeding blanket of a fusion reactor. The irradiation volume is located behind a stable liquid Li jet onto which two 125 mA deuteron beams are delivered. The high anisotropic (forward directed) neutron emission of the stripping process generates a rather high flux but in a relatively small useful irradiation volume. This volume is subdivided into three regions: i) the high flux test region ii) the medium flux region and iii) the low flux test region. The irradiation damage production in terms of displacement per atom (dpa) in these regions in a full power year (fpy) of operation is respectively, 20-55 dpa/fpy, 1-20 dpa/fpy and 0.1-1 dpa/fpy. In its current design, the high-flux, medium-flux and low-flux irradiation volumes are respectively of the order of 0.5 liter, 6 liters and 100 liters. In the high-flux region, mainly reduced activation materials for the first wall and blanket will be irradiated in instrumented capsules. The specimens will be tested after irradiation in hot cells. Among the materials foreseen to be irradiated in this region, we mention the tempered martensitic and the oxide dispersion strengthened steels, the vanadium alloys, the SiC_f-SiC composites, the refractory metals and alloys. Twelve separated rigs have been designed in which the irradiation temperature will be independently controlled between 250°C and 1100°C. The medium and low flux volumes will be devoted to fully instrumented in-situ tests such as creep fatigue, crack growth tests, stress corrosion tests, radiation induced conductivity, electrical degradation, tritium diffusion and release experiments. The materials concerned by these last experiments are ceramic insulators, rf-windows, ceramic breeder materials, Be-neutron multipliers and superconducting materials.

In order to use effectively the irradiation volume of the high flux volume in particular, specimens as well as the corresponding test techniques have to be miniaturized. The miniaturization of the specimens is also driven by the need of reducing the strong neutron flux gradient intrinsic to this type of source and therefore to obtain a reasonable irradiation damage homogeneity through a given specimen. In addition, it is also highly desirable to miniaturize the specimens form the point of view of handling, testing and managing radioactive materials. Over the last decades, numerous techniques applied to non-standard specimens have been developed to extract a host of mechanical and physical properties and to benchmark them with respect to the standard mechanical testing methods. Reviews and recommendations for small specimen techniques have been published e.g. [6,7]. A review of all the miniaturized and sub-sized specimens foreseen for IFMIF can be found in [8]. Among these techniques, some are simply based upon a scaling-down of the standard counterparts (tensile, fatigue, fracture toughness, for example). Other non-standard techniques have also emerged like for instance the small ball punch that we discuss hereafter. On a phenomenological basis, correlations between parameters obtained from the non-standard techniques with the usual parameters measured on standards tests have been established. However, there still remains some lack of understanding of the underlying physical processes that control the various calibration factors and their material and irradiation dependence. In order to gain insight into these processes, modeling, in the

broadest sense of the term, constitutes an inseparable tool for the correct interpretation of the results. In this line of thinking, we developed finite element models that we applied to investigate the plastic flow properties from ball punch tests and to study the influence of the constitutive behavior on the attainment of a local criterion for cleavage, criterion often considered to account for the size/geometry effects of the specimens on fracture toughness.

3. Plastic flow assessment from small ball punch tests

The small ball punch (SPT) tests have been developed to extract the tensile and fracture properties [9] and to assess the so-called ductile to brittle transition temperature [10]. In *FIG. 1*, the ball punch test experimental device is presented. It consists in deforming a center-loaded clamped disk with a spherical puncher; the load-displacement curve is then recorded. The spherical puncher is a 0.5 mm radius (R1) hard steel ball. The ball is pushed with a rod through a 1 mm hole in the upper die (D1) (a small tolerance of 0.05 mm and oil lubrication are necessary). The diameter of the hole in the lower die is 1.5 mm (D2) having a machined round billet radius of 0.2 mm (R2). The sample (in black) is a disc of 3 mm diameter (D3) and a thickness varying between 0.23 and 0.27 mm approximately (T). More details about the experimental procedure can be found in [11]. Using ABAQUS 6.4-1 code, a finite element model was developed and validated with two different steels (austenitic and tempered martensitic) [11]. Making use of our finite element model, we discuss below the expectations and limitations of the ball punch test technique in assessing the potential irradiation-induced changes in the constitutive behavior. Let us first recall that, in order to simulate a SPT curve, it is necessary to assign a constitutive behavior to the sample disk in the form of a uniaxial true stress–platic true strain relationship, $\sigma(\varepsilon_p)$. Actually, the ABAQUS code requires this input to model the multiaxial stress state that develops in the deformed disk using the von Mises stress potential and associated J_2 flow rule. Thus, the fundamental idea of modeling the SPT curves obtained on irradiated disks is to determine, with a series of successive simulations, a true stress - true strain relationship that allows reconstruction of the SPT curve. Let us emphasize that, after irradiation, the true stress – true strain relationship can usually not be readily established by conventional tensile test owing to the onset of necking taking place at very low strain, preventing the assessment of the post-yield behavior. In the following, we focus our attention on the behavior of the 7-9Cr class of reduced activation tempered martensitic steel, using the F82H-mod steel, produced in the framework of material development for fusion structural applications.

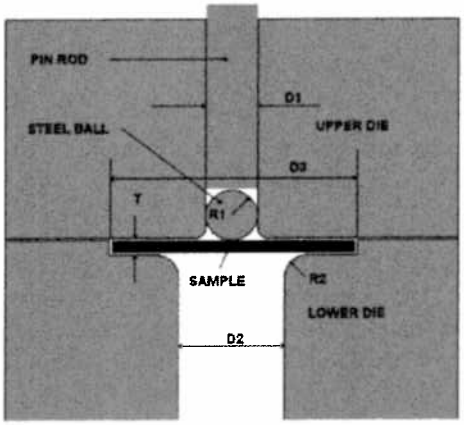

FIG. 1 Experimental ball punch test device

A typical experimental SPT load-deflection curve obtained at room temperature is shown in *FIG. 3*. Along with the experimental data, we present five simulated curves, among which two deal with the constitutive behaviors of this steel in the unirradiated condition and three are related to possible constitutive behavior that may result from irradiation-induced changes. Therefore, five specific true stress–true strain relationships have been employed to calculate the corresponding five SPT curves in *FIG. 3*. These true stress–true strain relationship are shown in *FIG. 2*.

Let us discuss first the curves obtained for the unirradiated material. The two $\sigma(\varepsilon_p)$ curves for the unirradiated case were obtained by extrapolating the experimental standard tensile curve, whose true uniform strain is limited to 5%. We have already demonstrated that the constitutive behavior of a variety of tempered martensitic alloys can be successfully described in the framework of a simplified model of net storage of dislocations with plastic strain [12,13]. In this model, the increase of the post-yield component of the flow stress σ_{pl}

scales with $\rho^{1/2}$, where ρ is the total dislocation density. When the storage rate of dislocations balances the annihilation rate, the net storage is zero and the flow stress does not increase any more. Hence, within the framework of this simplified model, a saturation stress is expected. The corresponding $\sigma(\varepsilon_p)$ curve is plotted in blue in *FIG. 3*. The red curve in *FIG. 3* was obtained by extending the curve beyond necking with a linear slope [11]. Simulating the SPT curves with one or the other of stress-strain relationships assigned to the disk leads to a significant difference in the quality of the fit at deflections larger than 0.4 mm. Clearly, an excellent agreement between the simulation and the experimental SPT curves was found when using the $\sigma(\varepsilon_p)$ curve without saturation. In fact, the maximum load and the deflection at maximum load were well reproduced while the $\sigma(\varepsilon_p)$ curve with saturation failed to satisfactorily simulate the SPT curve at deflections larger than 0.4 mm. It must be underscored here that the SPT curves permit to sample intermediate to large strains, about 60% in terms of equivalent plastic strain at maximum load. Such strains are much larger than those measured by tensile tests. Therefore, the small ball punch test technique, when used in conjunction with finite element modeling, allows evaluation of the $\sigma(\varepsilon_p)$ curve over a plastic strain range that has not been explored yet. From the simulations of the unirradiated F82H-mod punch curves, we concluded that a linear strain-hardening stage beyond necking controls the plastic flow of the tempered martensitic steel.

We have studied the effect of irradiation hardening on the shape of the SPT curves by constructing three different true stress-true strain curves representing possible constitutive behaviors of the irradiated F82H-mod steel. We arbitrarily selected an irradiation hardening (difference between the yield stresses of the unirradiated and irradiated material) of 300 MPa and constructed three different post-yield behaviors. For the first one, the same strain-hardening as that of the unirradiated material was chosen, the second one accounts for a loss of strain-hardening and the third one considers an initial softening of 100 MPa over the initial 5 % of plastic strain followed by a moderate strain-hardening regime identical to that of the unirradated case above 5 %. For an in-depth discussion of the origin of such a softening and subsequent moderate strain-hardening, we refer to [14]. In *FIG. 2*, these three

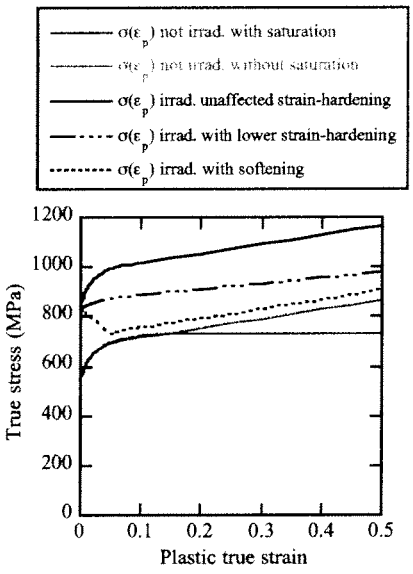

FIG. 2 Five different constitutive behaviors used as input to simulate the corresponding SPT load-deflection curves

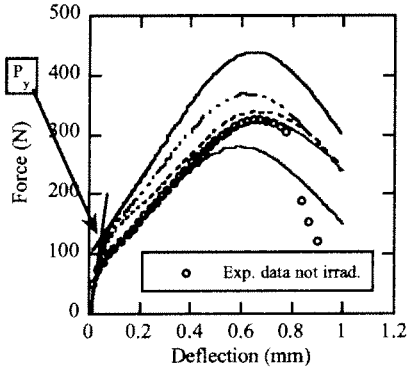

FIG. 3 Five simulated SPT load-deflection curves and one experimental curve obtained in the unirradiated condition. The colors correspond to those of the $\sigma(\varepsilon_p)$ curves of figure 2 used as input for the simulations

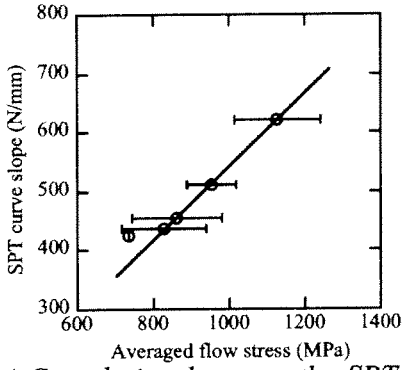

FIG. 4 Correlation between the SPT curve slope and the averaged flow stress determined between ε = 0.1 and 0.8.

curves are referred as to *unaffected strain–hardening* curve, *lower strain-hardening* curve, and *with softening* curve respectively. The SPT curves calculated after having assigned these three constitutive behaviors to the punch disk are plotted in *FIG. 3*. Interestingly, it is observed that the load P_y, determined by the intersection of the two slopes of the load–displacement curve drawn on both side of the yielding zone, is practically independent of the post-yield behavior. This fact confirms a previous observation we made [11], *i.e.*, that P_y is mainly mediated by the yield stress $\sigma_{0.2}$. Furthermore, this also supports the use of a simple and direct calibration between P_y and $\sigma_{0.2}$. Consequently, it is reasonable to estimate the irradiation hardening from the P_y increase itself provided that a good calibration is established. As far as the post-yield behavior is concerned, it can be stated that its major role is reflected in the slope of the load-deflection curve beyond 0.2 mm. In the deflection range 0.2 mm up to 0.6 mm, the equivalent plastic strain in the disk, while not uniform at all in the disk, varies from about 0.1 to 0.6. Looking at the $\sigma(\varepsilon_p)$ curve, in *FIG. 2*, it can be seen that in this strain range, the flow stress increase is moderate. Using a very crude approximation, albeit quite reasonable, the material can be regarded as deforming at a constant averaged flow stress over the strain range 0.1-0.6. For the *unaffected strain–hardening* curve for instance, the averaged flow stress is about 1100 MPa ± 100 MPa over the strain range 0.1-0.6. Actually, the slope of the SPT load-deflection curve beyond 0.2 mm tends to scale with the averaged flow stress over the strain range 0.1-0.6 as it can be seen in *FIG. 4*. Thus, these slopes can be seen as the signature of the averaged strain-hardening capacity of the materials defined as the difference between the averaged flow stress and the yield stress.

Finally we would like to emphasize the following point. As already mentioned, the simple uniaxial $\sigma(\varepsilon_p)$ relationships cannot be obtained by tensile tests on irradiated materials owing to the occurrence of necking at small strain. Thus, in principle, a so-called inverse methodology has to be used, where the $\sigma(\varepsilon_p)$ curves are adjusted until a good fitting of the SPT curve is obtained. Following the above discussion, it is believed that the irradiation hardening can be satisfactorily obtained from the P_y-$\sigma_{0.2}$ calibration as well as the average strain-hardening capacity while the fine details of the $\sigma(\varepsilon_p)$ shape may certainly not be unambiguously extracted.

4. Effect of the constitutive behavior on fracture toughness

The tempered martensitic steels, like the F82H-mod, undergo a so-called ductile to brittle fracture mode transition from high-temperature microvoid coalescence to low-temperature cleavage [15]. As a consequence of neutron irradiation, the transition between the ductile and brittle regimes is shifted to higher temperatures. It is therefore of primary importance to characterize both the fracture properties of the unirradiated materials and to develop a methodology, based upon an understanding of the fundamental mechanisms, to assess the changes in fracture toughness under irradiation in order to safely manage reactor structures. As mentioned above, the fusion reactor structural materials will be qualified after irradiation in IFMIF. Consequently, fracture toughness data obtained ***only*** on sub-sized specimens, which ***do not*** meet the usual requirements of the ASTM standards, will have to be considered in the material database for designers. In other words, the standard fracture mechanics does not apply and models have to be developed that account for the size and geometry of the specimens on fracture toughness. This can be successively achieved only if strong efforts are done to better understand the whole sequence of micro- to macro-mechanisms controlling fracture. Modeling has become a key element that must be

integrated in the analysis of the experimental results. Of course, modeling has to be understood at a multiscale level where, at the continuum level, finite element analysis is a well appropriate tool. It is evidently not possible to discuss here all the details of the models currently used to account for the specimen size and geometry effects on fracture toughness. However, we briefly remind the underlining ideas of the methodology and we address only one specific point in this section.

In order to characterize the fracture toughness in the brittle regime, we can make use of the so-called local approach to cleavage to deal with the size/geometry problem. This approach is described in details in the work of Nevalainen and Dodds [16] where the model for cleavage requires the attainment of a critical stress σ^* within a critical stressed volume V^* to trigger cleavage. Other models based on the same general idea have also been used to account for the constraint loss effect on fracture toughness. While differing in the details, they involve a critical stress σ^* but acting over a critical distance λ^* or a critical area A^* [17,18]. Applications of these simple models have been successful in predicting fracture toughness in the transition region for various alloys. In particular, the constraint adjustments have been recently applied to the existing fracture toughness database of the F82H-mod steel in the transition with the ultimate goal of using a similar master curve approach as that developed for the reactor pressure vessel steel [19].

In this study, we investigate the possible effects of the irradiation hardening (increase of the yield stress) and of the post-yield behavior on the critical applied stress intensity factor necessary for the attainment of the critical condition for cleavage. In order to do so, we simulate the stress/strain fields ahead of a crack tip for plane strain and elastic-plastic small-scale yielding conditions (SSY). A fully circular model, based upon the modified boundary layer model, that contains a small notch radius ρ_o in the middle was built, in a quite similar way as the semi-circular model described in [20]. The opening of the crack was performed in mode I by imposing the standard elastic displacements, Δx and Δy, of the nodes on the outer circular boundary and considering a T-stress equal to zero. Δx and Δy are written as:

$$\Delta x = K\frac{1+\upsilon}{E}\sqrt{R/2\pi}\cos\left(\frac{\theta}{2}\right)\left(3-4\upsilon-\cos\theta\right) \qquad \Delta y = K\frac{1+\upsilon}{E}\sqrt{R/2\pi}\sin\left(\frac{\theta}{2}\right)\left(3-4\upsilon-\cos\theta\right)$$

where is r is the radial distance from the crack tip and θ is the angle between the crack plane and the direction to the node, ν is the Poisson ratio and E the Young modulus. Note that the imposed displacements scale with the applied stress intensity factor K. 2D linear reduced integration elements were used. To limit the effect of the initial tip radius on the stress field at the crack tip, we ran simulations such that the crack tip opening displacement δ assures that the ratio δ/ρ_o is larger than 4.

For the unirradiated F82H-mod steel, the fracture toughness in SSY condition is about 100 MPa $m^{1/2}$ at 170 K, temperature at which we ran a series of simulations. The corresponding measured constitutive behavior in the unirradiated condition is presented in *FIG. 5*. The necking begins at 0.05 and then the curve is simply linearly extrapolated. We selected three possible hypothetical true stress-true strain curves for the irradiated condition. All the three curves exhibit an irradiation hardening of 100 MPa but different post-yield behaviors. In the first case, the strain-hardening is not affected by irradiation. In the second case, the curves shows a Lüders-type strain region without strain-hardening up to 0.03 followed by the same strain-hardening law as that of the unirradiated material. In the third case, we consider a moderate softening (-50 MPa) over a strain of 0.03 also followed by the same strain-hardening law as that of the unirradiated material. As mentioned, the fracture toughness at 170 K is about 100 MPa $m^{1/2}$ so we imposed the corresponding elastic displacement field on the outer boundary of the mesh and assigned the $\sigma(\varepsilon_p)$ unirradiated curve as the constitutive behavior of the material. Then, we assume that the local critical condition for cleavage is given by $\sigma^* = 2000$ MPa acting over an area $A^* = 1\text{x}10^{-8}$ m^2. These last values for the (σ^*-A^*) criterion are quite similar to those already used for the F82H-mod steel to model the fracture toughness-temperature curve [18]. Then, we simulate the stress fields that develop

at the crack when one or the other of the three constitutive behaviors for the irradiated materials was selected and we search the required applied stress intensity factor K to reach the cleavage condition σ*-A*. The results are summarized in Table I below where the strong influence of the post-yield behavior on the attainment of σ*-A* can be clearly seen. Therefore, it of a prime importance to establish the true stress-true strain relationship over a significant strain range (about 0.05). This is particularly evident if we want to predict the fracture toughness change after irradiation based upon a σ*-A* criterion. Unfortunately, we already mentioned that the tensile testing of the irradiated specimens does not allow getting this information due to the necking at low strain. Consequently, we recommend foreseeing in the IFMIF specimen matrices the inclusion of new type of specimens like compression or torsion ones, which would permit to investigate the true stress-true strain relationship over a significant strain range.

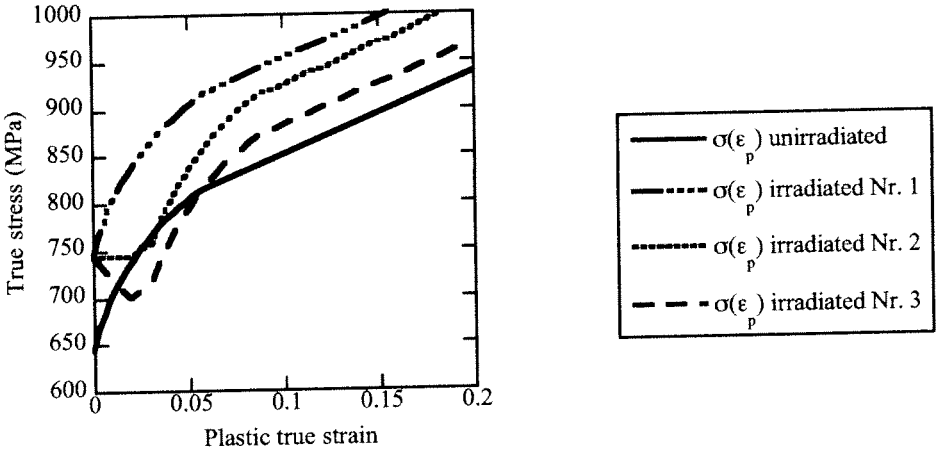

FIG 5. Four different constitutive behaviors used as input to simulate the stress field at a crack tip.

Table I Applied stress intensity factor K to reach the selected cleavage criterion σ*-A*

Constitutive relationship	Applied K to reach: $\sigma^* = 2000$ MPa - $A^* = 1 \times 10^{-8}$ m^2
$\sigma(\varepsilon_p)$ unirradiated	100 MPa m$^{1/2}$
$\sigma(\varepsilon_p)$ irradiated Nr. 1	56 MPa m$^{1/2}$
$\sigma(\varepsilon_p)$ irradiated Nr. 2	66 MPa m$^{1/2}$
$\sigma(\varepsilon_p)$ irradiated Nr. 3	85 MPa m$^{1/2}$

5. Conclusions

In this paper, we reported new developments for the analysis of small ball punch tests (SPT) as well as on the stress/strain fields at the tip of a stationary crack based upon finite element simulations. We showed that it is possible to reconstruct the entire SPT load-deflection curves. We discussed the influence of the yield stress and of the post-yield behavior on the overall shape of the SPT curve. We concluded that the yield stress, measured by standard tensile tests, can be fairly evaluate through a calibration with the yield load of the SPT curve, independently of the post-yield behavior. A very good estimation of the strain-hardening capacity of the materials after irradiation can also be done by considering the slope of the SPT curves at deflection larger than 0.2 mm. However, a precise determination of the shape of the $\sigma(\varepsilon_p)$ curves is certainly more critical. As far as the fracture toughness is concerned, we studied the influence of the irradiation hardening and of moderate variations in the constitutive behavior on the applied stress intensity factor necessary to reach a local criterion for cleavage. It was found that these moderate variations in the constitutive properties lead to significant ones in fracture toughness. Hence, we identify a real need to better characterize the post-yield behavior of the irradiated specimens and recommend to foresee in the IFMIF irradiation matrices not only tensile specimens but also compression or

torsion ones that would allow precise determination of the strain-hardening in the low to moderate strain range.

Acknowledgments

The Paul Scherrer Institute is acknowledged for providing access to its facilities. This work has been supported by the EFDA Technology Programme. The financial support of the Swiss National Foundation is gratefully acknowledged.

References

[1] HISHINUMA, A., et al. "Current status and future R&D for reduced-activation ferritic/martensitic steels", J. Nucl. Mater. **258-263** (1998) 193.

[2] RENSMAN, J., et al., "Tensile properties and transition behavior of RAFM steel plate and welds irradiated up to 10 dpa at 300°C", J. Nucl. Mar. **307** (2002) 245.

[3] MARMY, P., et al., "Pirex II – A new irradiation facility for testing fusion first wall materials", Nucl. Inst. Meth. Phys. Res. **B47** (1990) 37.

[4] EHRLICH, K., MÖSLANG, "IFMIF – An international fusion materials irradiation facility", Nucl. Inst. Meth. Phys. Res. **B139** (1998) 72.

[5] MÖSLANG, A., et al., "Suitability and feasibility of the International Fusion Materials Irradiation Facility (IFMIF) for fusion materials studies", Nucl. Fusion **40** (2000) 619.

[6] LUCAS, G.E., "The development of small specimen mechanical test techniques", J. Nucl. Mater. **117** (1983) 327.

[7] LUCAS, G.E., et al., "Recent progress in small specimen test technology", J. Nucl. Mater. **307-311** (2002) 1600.

[8] JUNG, P., et al., "Recommendation of miniaturized techniques for mechanical testing of fusion materials in an intense neutron sources", J. Nucl. Mater. **232** (1996) 186.

[9] MAO, X., TAKAHASHI, H., "Development of a further miniaturized specimen of 3 mm diameter for TEM small punch tests", J. Nucl. Mater **150** (1987) 42.

[10] SONG, S.H., et al., "Temper embrittlement of a CrMo low-alloy steel evaéuated by means of small punch testing", Mater. Sci. Eng. A **281** (2000) 75.

[11] CAMPITELI, E.N, et al., "Assessment of the constitutive properties from small ball punch test: experiment and modeling", *accepted in* J. Nucl. Mater (2004).

[12] BONADE, R., et al., "Plastic Flow of Martensitic Model Alloys", *accepted in* Mat. Sci. Engng A (2004).

[13] BONADE, R., et al., "Tensile Properties of a Tempered Martensitic Iron-Chromium-Carbon Model Alloy", J. Nucl. Mater **329-333** (2004)

[14] ODETTE, G.R., et al., "Modeling the multiscale mechanics of flow localization-ductility loss in irradiation damaged bcc alloys", J. Nucl. Mater **307-311** (2002) 171.

[15] ODETTE, G.R., "On the ductile to brittle transition in martensitic steels–Mechanisms, models, and structural implications", J. Nucl. Mat. **212-215** 45 (1994).

[16] NEVALAINEN, M., DODDS, R.H., "Numerical investigation of 3-D constraint effects on brittle fracture in SE(B) and C(T) specimens", Inter. J. Fract. **74** (1995) 131.

[17] RITCHIE, R.O., et al., "On the relationship between critical tensile stress and fracture toughness in mild steel", J. Mech. Phys. Sol. **21** (1973) 395.

[18] ODETTE, G.R., et al. "Developing fracture assessment methods for fusion reactor materials with small specimens", Small Specimen Test Techniques, ASTM STP 1329

[19] ODETTE, G.R., "A master curve analysis of F82H using statistical and constraint loss size adjustments of small specimen data", J. Nucl. Mater **329-333** (2004) 1243.

[20] GAO., X., et al. "Calibration of Weibull stress parameters using fracture toughness data" Inter. J. Fract. **92** (1998) 175.

Third-harmonic, top-launch, ECRH experiments on TCV Tokamak

S. Alberti 1), G. Arnoux 1), L. Porte 1), J.P. Hogge 1), B. Marletaz 1), P. Marmillod 1), Y. Martin 1), S. Nowak 2), and the TCV Team 1)

1)Centre de Recherches en Physique des Plasmas CRPP EPFL
Association EURATOM-Confédération Suisse
CH-1015 Lausanne, Switzerland
2)Istituto di Fisica del Plasma
EURATOM-ENEA-CNR Association, Milano, Italy

e-mail contact of the first author: stefano.alberti@epfl.ch

Abstract In the moderate magnetic field of TCV (1.5T), the recently installed X3 system (3 gyrotrons @118GHz, 0.45MWeach, 2s) broadens the operational space with the possibility of heating plasmas at high density, well above the cutoff density of the X2 system. To compensate the significantly weaker absorption coefficient compared to the absorption of X2, the top-launch injection allows to maximize the ray path along the resonance layer thus maximizing the optical depth. To maintain the maximum absorption in plasma discharges with a dynamic variation of both density (refraction) and temperature (relativistic shift) a real time control system on the poloidal injection angle has been developped and succesfully tested on TCV. Comparisons of the absorption calculated with the TORAY-GA ray-tracing code and the beam-tracing code, ECWGB, which includes diffraction effects, are presented. An experimental study of the X3 absorption versus plasma density in an L-mode plasma shows that with a total injected power of 1.35 MW full single-pass absorption is reached with a significant fraction of the absorbed power associated to the presence of suprathermal electrons. Compared to ohmic/low-power-heating of ELMy H-modes, it has been possible to enter into a significantly different ELMy regime with an injected power of 1.35MW .

1. Introduction

The recently completed ECH system on the TCV Tokamak, with a total of 4.5MW of installed power (4.1 MW of injected power), and with a highly flexible launching mirror system allowing real time control of the toroidal and poloidal mirror angles, is, at present, the most relevant ECH system for ITER. It consists of 9 gyrotrons grouped in three "clusters" of three gyrotrons each[1]. Two of the clusters operate at 82.7 GHz (0.45MW/gyrotron, 2s) and are used for heating and/or current drive, coupling to the X-mode EC plasma wave from the low-field side and being absorbed at the 2^{nd} harmonic resonance (X2). The third cluster operates at 118GHz (0.45MW/gyrotron, 2s), couples to X-mode from the top of the vacuum vessel and provides the ECH power which is absorbed at the 3^{rd} harmonic resonance (X3)[2].

In the moderate magnetic field of TCV (1.5T), the X3 system broadens the operational space with the possibility of heating plasmas at high density, well above the cutoff density of the X2, where the cutoff for the X2 and X3 waves are 4.2 $10^{19}[m^{-3}]$ and 11.5 $10^{19}[m^{-3}]$, respectively. To compensate the significantly weaker absorption coefficient compared to the absorption of X2, the top-launch injection maximizes the ray path along the resonance layer thus maximizing the optical depth.

2. Experimental setup

As shown in Figure 1, on the left, the three waveguides radiate the rf beams onto a single elliptical mirror. This mirror is made of copper and has a 700mm focal length, focusing the beam inside the plasma. Assuming a gaussian distribution, its minimum waist is w_0 =33mm in E-field. The mirror can be steered radially from 800m to 960mm from pulse to pulse and the

poloidal injection angle θ_l can vary from 40 to 50 degrees during the shot with a maximum speed of 20 deg/s.

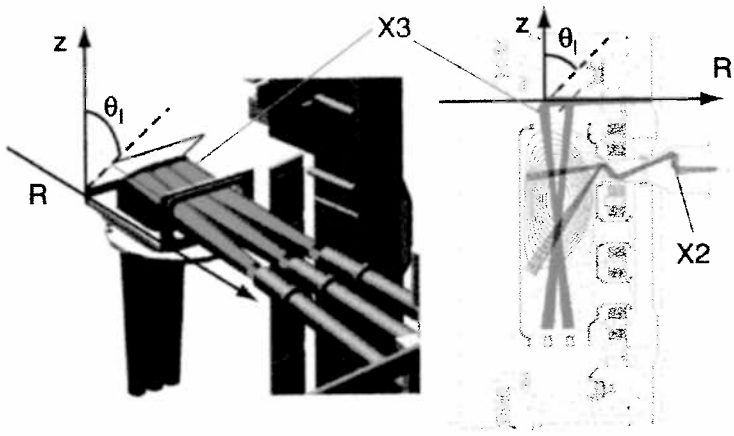

FIG.1. On left side, view of the X3 top-launch mirror. The three RF beams radiated from the HE_{11} waveguides are directed on one single focusing mirror which has radial and poloidal steering capabilities. The poloidal angle, θ_l, can be controlled in real time. On the right side, a poloidal cross section of TCV, with shown, in red, the rf beam paths corresponding to the maximum radial steering range of the X3 launcher. In blue, the poloidal steering range of the X2 launcher.

The main characteristic of the X3 top-launch heating is its sensitivity of the absorption versus poloidal injection angle as it is shown in Figure 2 [2,3,4]. For a given plasma equilibrium shown in Figure 2b) and a fixed launcher radial position, the plasma response versus poloidal injection angle is shown in Figure 2a). With 0.45 MW of injected power, the level of absorption is indicated on this figure by the variation of the central temperature (T_e-X, blue curve) deduced from the soft X-ray emission measurement along a central vertical view line (two-foil method). As a comparison, the calculated absorption with the TORAY-GA code is shown in red. A good agreement between the experiment and the simulation is found.

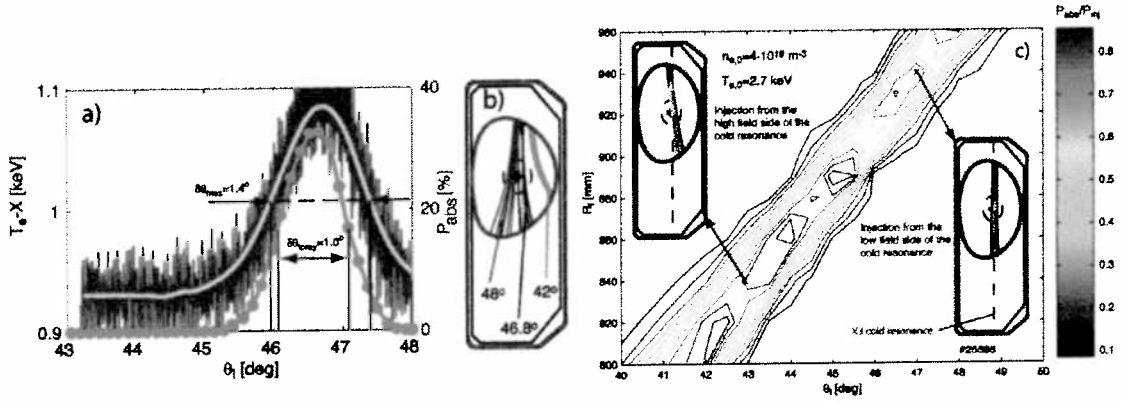

FIG.2. a) Blue trace: plasma temperature, Te-X, versus poloidal injection angle (the yellow trace is the result of low-pass filtering the blue trace). In red, the absorbed fraction as predicted by TORAY-GA. b) Cross section of the plasma with ray trajectories for different injection angles. Contour plot of absorbed fraction versus poloidal injection angle and radial position of the mirror.

The main point to be noticed is the fairly narrow angular range where the X3 wave is absorbed. The calculated X3 top-launch absorption versus poloidal injection angle and radial position of the launcher is shown in Figure 2c). The target plasma cross section is shown in the inserts and the absorption has been calculated on an experimentally obtained plasma equilibrium having a central electron density and temperature of 4 $10^{19}m^{-3}$ and 2.7 keV, respectively. One notices that the FWHM of the absorption versus poloidal injection angle is weakly dependent on the radial position.

3. Real-time feedback on the poloidal injection angle

To maintain the maximum absorption in plasma discharges with a dynamic variation of both density (refraction) and temperature (relativistic shift) a real time control system on the injection angle has been developped. The main element of this feedback system consists in a synchronous demodulation of an harmonic perturbation of the plasma response (line-integrated emissivity of a central soft-X ray chord), generated by sinusoidally varying the launcher injection angle. The dynamic response of the feedback system is related to the maximum frequency at which the mirror can be swept and this frequency has been determined by measuring the transfer function of the system composed by the mirror mechanical system and its motorization. The frequency response of this system is represented in a Bode diagram on Figure 3.

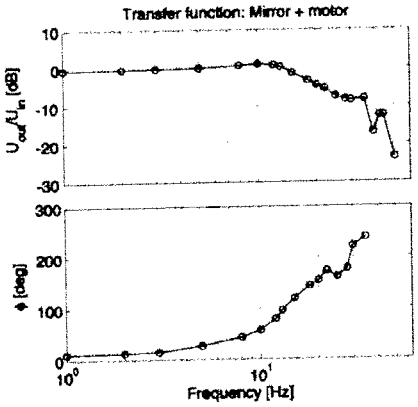

FIG.3. The frequency response of the top-launch mirror system is represented in a Bode diagram. This system consists of the mechanical part and the mirror motorization. The quantities represented in this diagram are the amplitude and phase of the ratio between the desired and actual mirror angular position. A strongly damped resonance is observed around the frequency of 13Hz which is chosen as the driving frequency for the harmonic perturbation.

The schematic of the complete feedback system is shown in Figure 4. In the Laplace transform representation the transfer function shown in Figure 3 corresponds to the function $G_2(s)$. The other elements of this system are detailed in the figure caption. The signal at the output of the low pass filter is proportional to the derivative of the plasma response shown in Figure 2a). The reference, R(s), is set to a value such to maintain the mirror angle on a zero derivative of $dT_e/d\theta$. Only the proportional term of the PID controller has been used in these experiments.

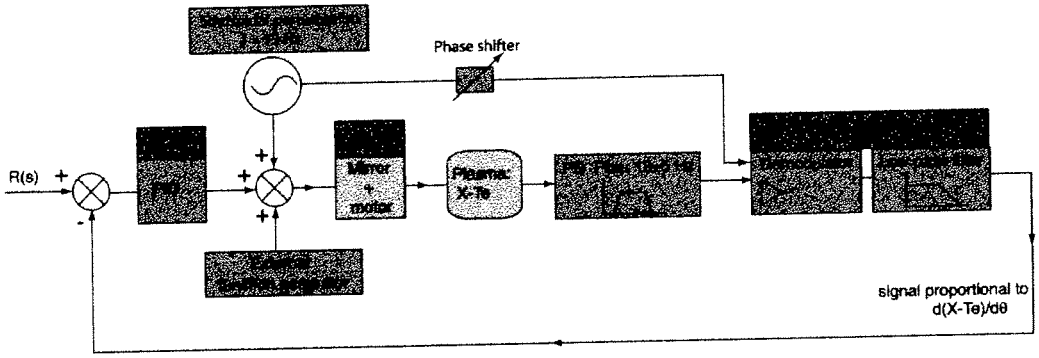

FIG.4. Schematic of the complete closed-loop feedback system. The harmonic perturbation at 13Hz is used both for applying the sinusoidal perturbation on the launcher mirror and also as an input of the synchronous demodulator which is placed after a pass-band filter centered at 13±5Hz. At the output of the demodulator the AC component is filtered out by a low-pass filter (f_{cutoff} = 2 Hz) with the resulting signal being proportional to the derivative of the plasma response function, $dT_e/d\theta$ where θ is the mirror poloidal angle. The dynamic response of the closed-loop system can be adjusted by the parameters of the PID regulator.

The open-loop characteristics of this system are shown in Figure 5, where the time traces of the relevant quantities are represented in a shot on which a linear sweep of the launcher angle is performed. The sweep is such to cross the optimum angle corresponding to the maximum X3 absorption.

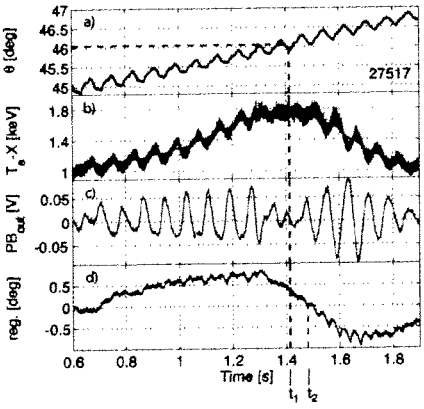

FIG.5. Open-loop signals during a linear sweep of the mirror poloidal angle. Trace a), linear angular sweep of the mirror poloidal angle with superimposed the sinusoidal perturbation at 13Hz. Trace b), Plasma central temperature deduced from the two-foil method using the soft X-ray emission measurement on a central chord. Trace c), Signal at the output of the pass-band filter whose envelope is proportional to the derivative $dT_e/d\theta$ of the Te-X signal. Trace d), signal at the output of the low-pass filter following the demodulator. The error signal, which is fed to the PID controller, is obtained by substracting this signal from the reference signal.

One notices that the envelope of the signal at the pass-band filter output (Trace c) crosses zero exactly at the time (t_1=1.41s) where the mirror is at the optimum angle. The small time delay between this time and the time of zero crossing of trace d) (t_2=1.47s) is caused by the low-pass filter. This small difference can be compensated by properly adjusting the level of the reference signal R(s).

The closed loop characteristics of the real-time feedback are shown in Figure 6. In this shot the mirror poloidal angle was pre-programmed to perform a linear sweep across the angular region of optimum heating (green line). The feedback controlled mirror-angle (red line) has been such to reach the optimum angle faster than the pre-programmed sweep and, once the optimum angle has been reached (t = 1.1s), the feedback has reacted such to maintain this optimum angle despite the externally imposed ramp, forcing the mirror to move away from the optimum. In the experiments with feedback performed so far only the proportional term of the PID controller was used. After an experimental optimisation of the different parameters in the system, a stable real-time control of the optimum injection angle of the X3 launcher has been obtained on a wide variety of L-mode plasmas.

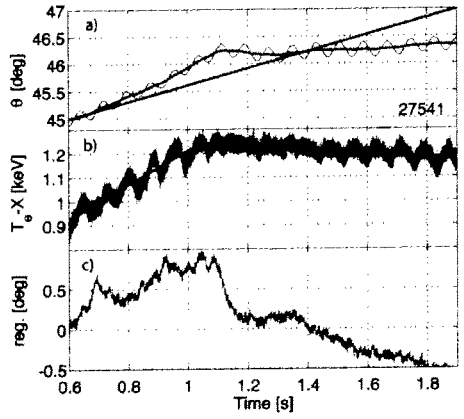

FIG.6. Real-time control of the mirror in a L-mode plasma. In this shot the mirror angle was programmed with a linear sweep (green line) across the optimum injection angle which occurs at t =1.1s. The error signal which is fed to the proportional controller is shown on trace c. On trace b), the time-trace of the central plasma temperature clearly demonstrates that once the launcher optimum angle is reached, the feedback controls the launcher such to maintain it on the optimum angle.

Further development of this real time control system are required in case of plasmas with an L-H transition and H-mode plasmas where the perturbations associated to the presence of ELMs and also rapid density variations strongly perturbe the feedback loop. A complete modeling of the system will allow to further optimize the dynamic response of the real-time

control. Once the Advanced Plasma Control System of TCV will be operational it is also planned to transform this analog controller to a digital one.

4. X3 Absorption with top-launch

The X3 absorption studies were significantly simplified with the real-time control of the launcher and the absorbed fraction versus plasma density at different levels of the injected rf power has been measured. With the mirror feedback control, the absorbed rf power was measured only after a stationary state of the mirror angle was reached. The absorbed fraction was measured during a modulated portion of the X3 rf pulse (full-power modulation of one gyrotron at 237Hz) using a diamagnetic loop [5].
The absorbed fraction versus plasma density is shown in Figure 7b, for two different levels of average injected rf power and a L-mode target plasma with a cross section as shown in the insert of Figure 2c (R_0 = 0.88m, a = 0.26m, κ = 1.6, δ =0.1, B_T = 1.45T, I_p = 230kA). The two levels of average injected power correspond to the sum of the average power of a fully square-wave modulated gyrotron (P_{av} = 225kW) plus the power of one (450kW) or two (900kW) additional gyrotrons.
The difference between the measured absorbed fraction (DML) and the one predicted by the TORAY-GA code is to be associated with the existence of a suprathermal population generated by the X3 wave itself and not taken into account in TORAY-GA. At higher electron densities this difference is lower since a fast thermalization of the suprathermal population occurs. The coupling to the ions (equipartition) is very weak since the average ion temperature, on a vertical chord, remains nearly constant at T_i = 510eV during the entire plasma shot.

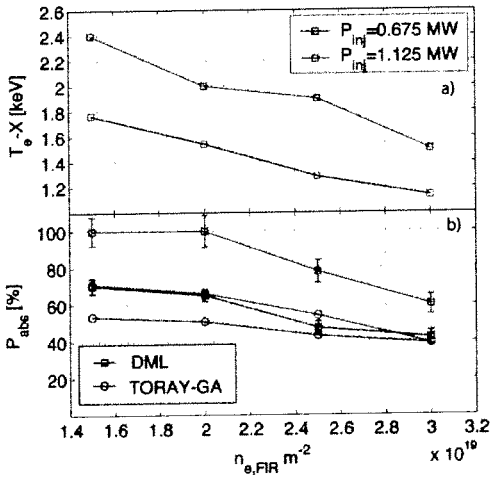

FIG.7. a) Central temperature versus line integrated density for two levels of X3 injected power. For the target plasma used, the value of the central density [m^{-3}], is twice the value of the line integrated density. The central temperature during the ohmic heating (before rf injection) is 0.9 keV.
b) Absorbed fraction measured with the DML (squares) and predicted by TORAY-GA (circles) versus line integrated density for two levels of X3 injected power (0.675MW and 1.125MW).

The typical density and temperature profile measured with the Thomson scattering diagnostic are shown in Figure 8 for a central electron density of 4.10^{19} m^{-3} which, on Figure 7, corresponds to a line integrated density of 2.10^{19} m^{-2}. The ohmic profiles (squares) are time averaged during 100ms before the X3 is turned on and the profiles during the ECH phase are time averaged from the start of the ECH pulse until the modulation phase is started. At the X3 power switch on, a clear flattening of the density profile is observed. This "pumpout" phenomenon has also been observed on X2 ECH and ECCD experiments on TCV [6] as well as on ASDEX Upgrade [7].
For the plasma target used in this study, a contour plot of the absorbed power fraction, calculated with TORAY-GA, versus central density and temperature is shown in Figure 9. The presence of a suprathermal electron population is not taken into account in this

calculation.The four inserts show the ray trajectories inside the plasma for the extremities of the density and temperature ranges.

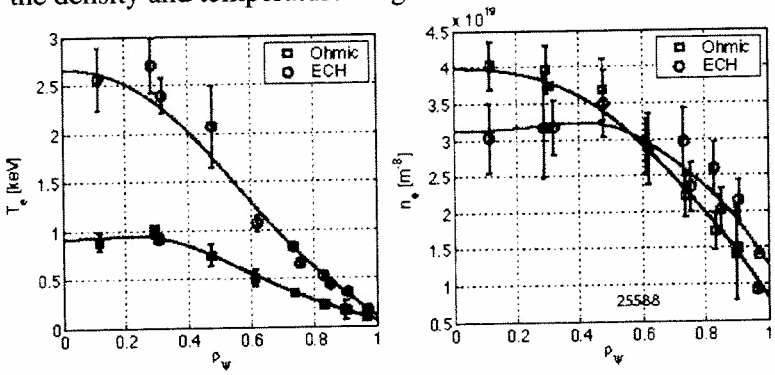

FIG.8. The temperature and density profiles measured with the Thomson scattering diagnostic for both ohmic and ECH phases. This shot corresponds to a point in Figure 7 with P_{inj} =1.125MW and line integrated density of 2.10^{19} m^{-2}.

The yellow part on each ray indicates the absorbed fraction between 10% and 90% of the total absorbed fraction for each specific ray. The cold resonance is indicated by the vertical dashed line and the q=1 surface by the circular dashed line.

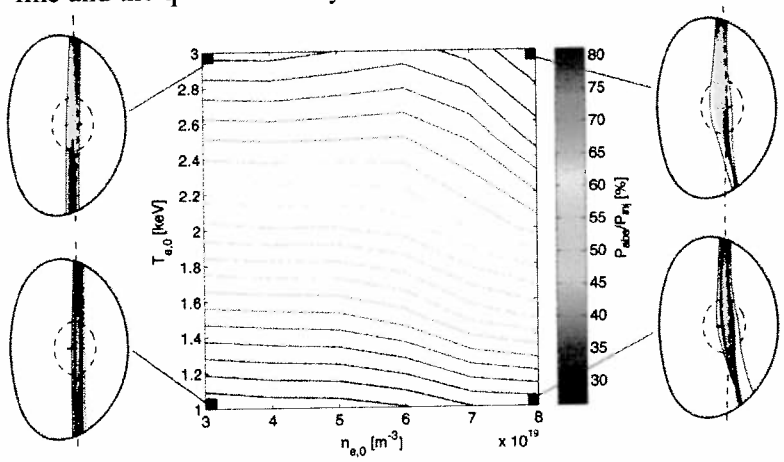

FIG.9. Contour plot of the absorbed power fraction calculated with TORAY-GA versus central plasma density and temperature. The equilibrium corresponds to shot 25588 and the calculation with TORAY-GA have been made by properly scaling the respective density and temperature profiles.

As expected, a strong dependence of the absorption on the electron temperature is observed, whereas the dependence on density is fairly weak. At high density, refraction effects can generate a fairly strong focusing of the rf beam. In this cases the WKB approximation, on which the ray-tracing code is based, might fail. In order to assess the importance of diffraction effects on the X3 power absorption, preliminary studies with the beam tracing code ECWGB [8] have been performed. In Figure 10 a comparison between the two codes is made. The launcher mirror has been designed [2] to be focusing inside the plasma with a minimimum waist located approximately at the vacuum vessel center.

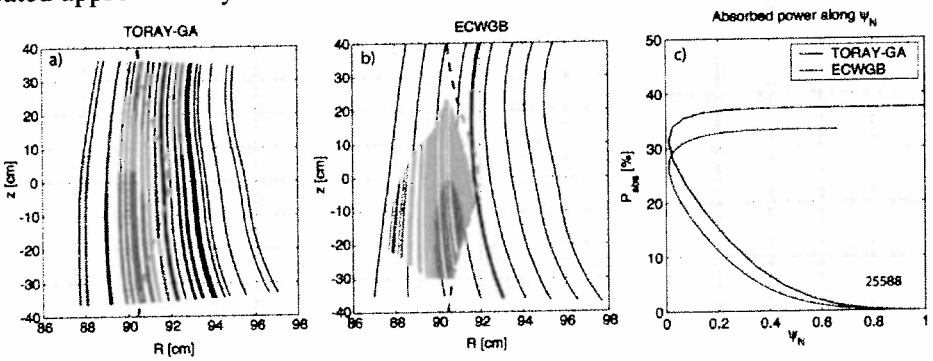

FIG.10. Comparison of the ray trajectories for the TORAY-GA (a) and ECWGB (b). On (c), the total absorption computed along the central ray (indicated in black on a) and b)) is shown in red for the ECWGB code and in blue for the TORAY-GA code.

In TORAY-GA, the focusing gaussian beam is approximated by a cylindrical beam with a gaussian rf power distribution of width $w_0/\sqrt{2}$. The ray trajectories of Figure 9 a,b show this effects especially for the case of ECWGB where the rf beam in the absorption region (described by the red colored rays) is slightly diverging which is consistent with a focusing beam having its minimum waist located at z 20cm. The slightly higher absorption predicted by TORAY-GA might be explained by the cylindrically shaped modeling of the rf beam.

Further comparisons between the two codes are presently underway especially for the cases where, at high density, refraction effects cause additional focusing (as shown in Figure 8).

5. X3 top-launch heating of quasi-stationary ELMy H-mode plasma

Until X3 heating was installed on TCV the only quasi-stationary H-modes that were routinely available were ohmic H-modes that were approached through a narrow gateway in parameter space [9]. Using X3 to heat the core of ELMy H-modes, accessed through the gateway, experiments have been performed to establish quasi-stationary additionally heated ELMy H-modes and to study the effect of heating on the ELMs. Initial results of X3 heating in quasi-stationary ELMy H-mode plasmas were presented by Porte et al. [10]. In this reference, results of low power X3 ECH ($P_{ECH,X3} < P_{\Omega}$, where $P_{ECH,X3}$ is the X3 absorbed power and P_{Ω} is the ohmic power) have shown that the ELM frequency was reduced with increasing $P_{ECH,X3}$ but they were unable to alter the ELMy regime (i.e. the ELM type).

In recent experiments, $P_{ECH,X3} \approx 3P_{\Omega}$ has been obtained and the results are significantly altered as compared to [10]. It has been possible to enter into an ELMy regime that is fundamentally different to ohmic/low-power-heating ELMy H-modes. The ELM frequency is reduced and the energy loss per ELM is significantly increased (≈ factor of 10). There seems to be a minimum additional heating power before the transition from one ELM regime to another can be achieved as it is demonstrated in Fig.11 when, at t=1.42s, one gyrotron is switched off.

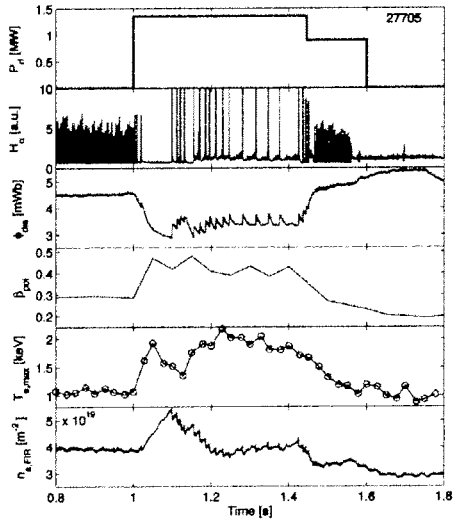

FIG.11: Temporal evolution of a quasi-stationary ELMy H-mode plasma, heated using top launch X3. The discharge exhibits a clear transition from one ELMy regime to another with the addition of X3 heating. The two ELMy regimes are distinguished by their ELM frequency and amplitude and by their effect on the stored energy. ELMs in the additionally heated phase cause an energy loss per ELM that is ≈10 times more than in the ohmic phase. At t≈1.42s one of the X3 gyrotrons was switched off and the plasma immediately went back to the ohmic/low power ELMy regime..

In Figure 11 a discharge is presented where the transition from the 'low-power' regime to the 'high-power' regime is achieved. With a total injected power of 1.35MW, the absorbed rf power during the quasi-stationary part of the discharge with large ELM's (t =[1.2-1.42s]), is in excess of 850kW. Work continues to determine the ELM type, according to the usual classification and to establish a technique to make the high-power ELMy regime easily and routinely accessible.

Further studies of the X3 absorption properties both in L and H-mode plasmas at higher elongations and triangularities will be investigated in the near future.

6. Conclusions

A top-launch X3 ECH system has been installed on TCV in order to heat high density plasmas. The X3 absorption is theoretically predicted to be strongly sensitive to the launcher poloidal angle. This strong dependence has been experimentally confirmed showing a typical launching angular width of $\pm 0.5^0$ (FWHM) within which the absorbed power fraction is maximized. This narrow width together with the goal of maintaining the optimum absorption in dynamically varying plasma conditions has motivated the development of a real–time control system of the launching angle. This system has been successfully tested and has allowed to perform extensive absorption studies in L-mode plasmas. With a total injected power of 1.35MW, full-single pass-absorption has been reached with a significant fraction of the power absorbed on a suprathermal population. Preliminary comparisons between the linear ray-tracing code TORAY-GA and the beam-tracing code ECWGB have been presented. First experiments with 1.35MW of injected power have demonstrated the accessibility to an ELMy regime that is fundamentally different to ohmic/low-power-heating ELMy H-modes.

Acknowledgement: This work was partially supported by the Swiss National Science Foundation

Appendix 1: References

[1] T. Goodmann et al., "Design and installation of the electron cyclotron wave system for the TCV tokamak",Fusion Technology (Proc. of 9th Symp. Lisbon 1996), North-Holland, Amsterdam (1997), 565.

[2] J.P. Hogge et al., "Preliminary results of top launch third harmonic X-mode electron cyclotron heating in the TCV tokamak",Nucl. Fusion, **43** (2003)1353.

[3] G. Arnoux et al., "Top-Launch X3 ECH and its use as an electron energy diagonstic on the TCV Tokamak", IAEA Technical Meeting on ECRH, Klosterseeon, July 2003.

[4] G. Arnoux et al., "Third-harmonic X3 absorption in a top launch configuration on the TCV tokamak, Submitted for publication

[5] A. Manini et al., "Modulated ECH power absorption measurements using a diamagnetic loop in the TCV tokamak", Plasma Phys. Control. Fusion, **44** (2002) 139.

[6] A. Zabolotsky et al.,"Observation and empirical modelling of the anomalous particle pinch in TCV",Plasma Phys. Control. Fusion, **45** (2003) 735.

[7] C. Angioni et al., Density response to centrel electronheating: theoretical investigations and experimental observations in ASDEX Upgrade, Nucl. Fusion, **44** (2004)827.

[8] D. Farina et al., "ECWGB: a beam tracing code for EC heating and current drice",IFP-CNR Internal Report FP 03/6, October 2003.

[9] Y. Martin et al.,"ELMing H-mode Accessibility in Shaped TCV Plasmas"; Proceedings of the 18th IAEA Conference on Fusion Energy, Sorrento, Italy, October 14–19 ; 2000.

[10] L. Porte et al.,"Third Harmonic X-mode Electron Cyclotron Resonance Heating on TCV using Top Launch ", Proceedings of the 19th IAEA Conference on Fusion Energy; Lyon, France, paper # EXP5-15

Shear modulation experiments with ECCD on TCV

S. Cirant 1), S. Alberti 2), F. Gandini 1), R. Behn 2), T.P. Goodman 2), and the TCV Team 2)

1) Istituto di Fisica del Plasma
EURATOM-ENEA-CNR Association, Milano, Italy
2) Centre de Recherches en Physique des Plasmas CRPP EPFL
Association EURATOM-Confédération Suisse
CH-1015 Lausanne, Switzerland

e-mail contact of the first author: cirant@ifp.cnr.it

Abstract Anomalous electron transport is determined by turbulence, which in turn is affected by magnetic shear. A novel application of Electron Cyclotron Current Drive (ECCD), aiming at localized shear modulation, has been applied on TCV tokamak for experiments on shear-dependent electron transport. Pairs of EC beams, absorbed at the same radius but oriented for co and counter injection, are modulated out of phase in order to force a local modulation of current density at constant input power. Off-axis deposition (ρ_{dep}=0.24) is performed for sawteeth control. A significant impact on local shear is achieved with $I_{ECCD} \approx 0.1 I_{OH}$ even if the modulation period is much shorter than current diffusion time. Although source (heat and particle) terms are constant, both electron density and temperature are modulated during alternated ECCD. Thomson Scattering is the diagnostic for local T_e and n_e measurement, in order to overcome suprathermal problems on ECE from high field side. Once equilibrium effects are taken into account for appropriate mapping of TS measurements onto flux coordinates, T_e and electron pressure modulation, peaked on-axis, is confirmed at all radii internal to EC deposition. Best confinement ($\Delta n_{e,0} T_{e,0}$=+12%) is for co-injection, when shear drops from ≈0.5 to less than 0.2.

1. Introduction

The current density profile in a tokamak is a key feature contributing to determine actual discharge thermodynamic quantities through separate but interlinked processes: it controls the relevant geometry by arranging flux surfaces consistently with equilibrium, it provides an heat source term, it determines MHD equilibrium, and it contributes to heat transport by affecting turbulence scale length. Any experimental attempt to study one or the other of these processes has to deal with the difficult task of a clear distinction between them.
Experiments on electron transport with Electron Cyclotron Heating (ECH) are carried out in many machines (AUG, DIIID, FTU, TCV, TS), focussed on the key issue of electron heat transport and its relation with turbulence [e.g.1,2,3]. Since magnetic shear can have an effect on the stability of the modes producing turbulence [4,5,6,7,8,9], clearly the interest in using Electron Cyclotron Current Drive (ECCD) for shear-control, finalized to transport studies, is great. However, this is a typical case in which much attention must be paid to separate heating effects, always present together with ECCD, from transport features. A way to do this is to compare co and counter ECCD in different shots [10]. In earlier times switching from co to cnt was performed within the same shot on the Stellarator Wendelstein VII-AS [11]. A similar procedure has been used in TCV tokamak, suitably tailored to shear modulation by choosing the switching frequency and the absorption radius in order to achieve the largest and most localized perturbation of the current density profile.

2. Experimental set up, practices and diagnostics

Shear-modulation experiments have been performed on TCV by using the ECRH-ECCD system which has recently been completed. It is composed by 9 gyrotrons divided in three

clusters. Each cluster is connected to a single high voltage power supply. Two of the clusters each have 3 gyrotrons (82.7GHz, 0.5MW, 2s) used for heating (ECH) and/or current-drive generation (ECCD) in 2nd harmonic X-mode (X2)[12] while the third cluster has 3 gyrotrons (118GHz, 0.5MW, 2s) for top-launch third harmonic X-mode (X3) heating[13]. Two gyrotrons at 82.7 GHz have been used for shear modulation experiments.
The essential aspects of the experimental procedure are as follows: two EC beams, or a pair of beam clusters when available, are oriented toroidally for driving ECCD in opposite directions, and poloidally for having the identical deposition radius r_{dep}. The power is switched on alternatively in the beam clusters by square-wave modulation of the pertaining power supplies at the identical frequency, but exactly out of phase. The power in the two beam clusters is such that the absorbed fraction is identical, so that the instantaneous EC heating is constant and equal to its average value. Because the heat source distribution is constant in time (not modulated), any observed synchronous electron temperature oscillation $\tilde{T}_e$ has to be ascribed to modulation of the transport properties.
In principle, co and cnt deposition layers can be finely overlapped by observing the heat wave excited by each one of the two clusters, the other one being kept CW at half power in order to have the same average absorbed power, and the same average T_e, in all conditions. More difficult is the balancing of the power in the two clusters, to the precision required for revealing small perturbations of thermal diffusivity. In order to take into account all imperfections in power balancing, a preliminary calibration experiment is performed with the same settings (plasma target and EC system) as for the Switching ECCD (SECCD) experiment, but for the toroidal angle which is set for purely perpendicular launch, without any driven current. The residual synchronous oscillations recorded in this calibration experiment provide the reference term to the real SECCD experiment.
Although all main diagnostics (ECE and soft-X emission, FIR interferometer) are used to monitor SECCD effects on electron temperature T_e and density n_e, the detailed quantitative analysis has been performed using Thomson Scattering data, because in this case both T_e and n_e measurements are really local, and taken at the same volume by definition.
Different modulation frequencies from 5 Hz to 70 Hz have been used, but the quantitative analysis discussed in this paper is performed on experiments at 5 Hz for two main reasons: as shown in the following, at this frequency the driven current is a substantial fraction of its steady-state value. Secondly, Thomson Scattering can be used in spite of its relatively low repetition rate of 20 Hz. Nyquist frequency is 10 Hz in this case, allowing FFT analysis of the 5 Hz modulated signals.
Experimental information on the current density profile is provided by the estimate of the internal inductance and by MHD activity, mostly by sawtooth. The diamagnetic loop is used to confirm appropriate power balancing between the two beam clusters.
Finally, it should be noted that stationary periodic perturbations allow the use of well-known techniques of synchronous detection with much greater sensitivity than in purely transient or steady-state conditions. In fact, the discussion in the following will be entirely based on amplitude and phase of oscillations (any quantity) at the fundamental switching frequency.

3. Steady periodic alternate ECCD and electrodynamic effects on magnetic shear

Because of the transient nature of SECCD, localized in a narrow layer inside a conductive medium, the elctrodynamic plasma response must be taken into account in the estimate of the actual distribution of the driven current. By taking advantage of the periodicity of the equivalent e.m.f. locally applied by SECCD, we follow a simplified procedure for calculating the periodical amplitude current distribution. Instead of solving the complete current diffusion equation, we imagine the plasma composed by N toroidal shells mutually coupled, with an

e.m.f. assigned to each shell accordingly to the calculated ECCD (TORAY, Fig.3). The periodical current distribution I_n, n=1:N, is provided by solving a system of linear circuit equations.

In order to get a reliable evaluation of the periodic modification of the shear profile, all sources of modulated current must of course be taken into accounts. We anticipate here the observation, thoroughly discussed in following sections, that the electron temperature is modulated during SECCD, which creates a modulated current drive term to be added to SECCD. From the electrodynamic point of view the change in resistivity is equivalent to the application of an additional, distributed "current drive" $J_\eta(\rho) = (\delta\eta/\eta)J(\rho)$, where $\delta\eta/\eta$ is the relative change in resistivity and $J(\rho)$ is the average current density profile. Figure1 summarizes the results of a simulation of shot #24867. Total ECCD current is 12 kA, peaked at 5.7 cm, 3.1 cm wide ($1/e^2$ of the peak value). Resistive current drive is peaked at center, it has a width of 5 cm, with a total modulated current of 12 kA. Swing frequency is 5 Hz. Main thing to be noted is that electrodynamic reaction to ECCD is strong, but a large fraction of localized current drive still persists, with a significant modulation of the current density profile . Magnetic shear modulation is therefore evident near r_{dep} (±60%, from 0.15 to 0.75 min to max).

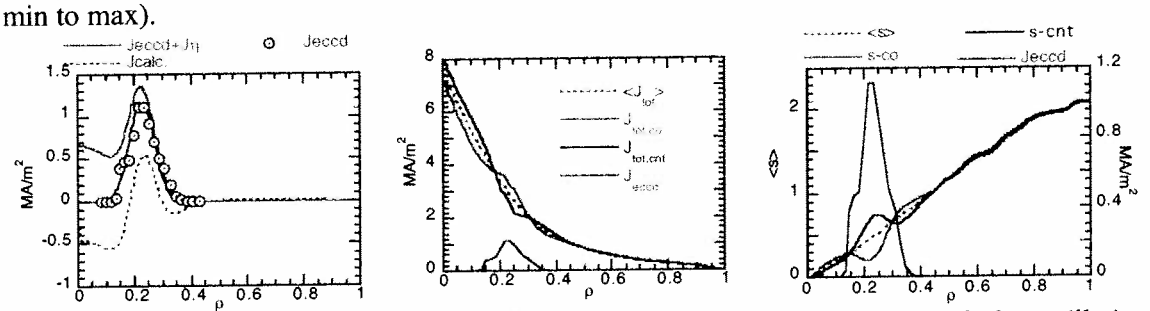

Fig.1 –Left: Total driving term, ECCD (dots) and resistive (solid line), is shown with the oscillating current amplitude (dashed), determined by electrodynamic reaction. Center: total current density, average (dashed), during co (red) and counter (blue) injection period. Right: magnetic shear profile.

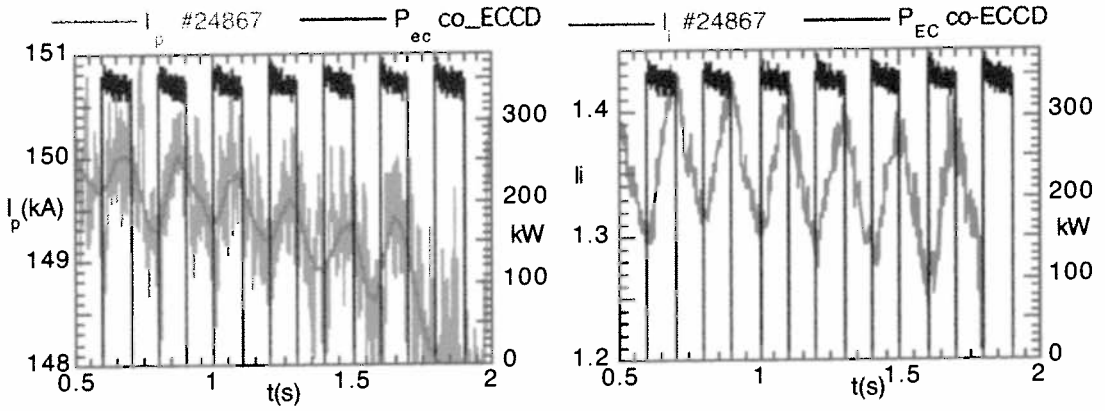

Fig.2 – Internal inductance (right), compared with EC power in the beam oriented for co-ECCD injection. Left figure shows plasma current oscillations, in-phase with the internal inductance and with co-ECCD.

An experimental validation of calculated current profile changes $\tilde{J}(\rho)$ is given by the internal inductance time evolution. Fig.2, left, shows the power from the gyrotron $P_{EC,co}$ dedicated to co-ECCD, and the plasma current oscillating correspondingly (with appropriate phase shift).

The internal inductance increases during the co-injection phase (Fig.2, right), consistent with the calculated flattening of the current density profile (Fig.1, center).
The change in internal inductance, due to both SECCD and resistivity oscillations, is $\delta l_i = 3.1\%$, very close to the measured value of 3.4%. In addition, a loop voltage (periodical) of $V_\omega = 20$ mV is calculated, very close to the measured value of 24 mV, with a very good agreement also between measured and calculated I_ω-V_ω phase delay.
Furthermore, sawteeth are suppressed during the co-injection phase (gyrotron 2), and re-appear during the cnt-injection phase (gyrotron 5). During cnt-injection the magnetic shear is strongly increased at r_{dep}, and the safety factor is slightly reduced inside r_{dep}. In the case of co-injection the opposite holds true. Both strong shear near to q=1 surface (note that $\rho_{inv} \approx 0.13 \leq \rho_{dep}$, which is the most effective arrangement for affecting sawteeth with ECH/ECCD) and low central q are destabilizing factors for sawteeth [14]. This is important experimental evidence supporting the claim that ECACD drives a modulation of the current density profile as foreseen and calculated.

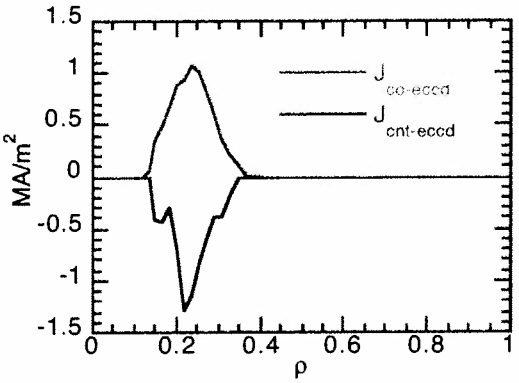

Fig.3 – Current density profile for co (red) and counter (blue) injection, calculated from linear ECCD theory (TORAY code).

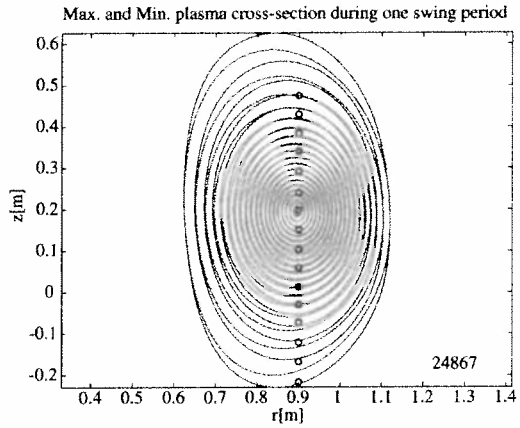

Fig.4 – Magnetic flux surfaces for co and counter injection. Dots mark the position of Thomson Scattering measurements.

4. Electron temperature modulation at constant heating power

The essential feature of swing ECCD experiments is that, in principle, the instantaneous EC heating power is constant. Any detectable $\tilde{T}_e$ synchronous fluctuation can be ascribed therefore to a modulation of heat confinement, possibly induced by SECCD. Effective $\tilde{J}(\rho)$ modulation might cause synchronous modulation of the whole equilibrium frame, as indeed observed (Fig.4). Since the grid of Thomson Scattering measuring points is fixed in the laboratory frame, this effect clearly must be taken into account. The electron density must be monitored and, in case of modulation, properly taken into account. A whole section will be dedicated to this point in the following
The striking feature (shot #24867) is that T_e strongly oscillates (more than 30% peak-to-peak at centre) in spite of constant input power. Fig.5 and Fig.6 show the main features of this internal heat wave. The whole T_e profile oscillates internal to the EC wave absorption radius r_{dep}. A thermal barrier (or a step-up in thermal diffusivity) is alternated at r_{dep} to a thermal bridge (or a step-down in diffusivity), in synchronism with ECCD. The phase distribution of the oscillations, Fig.6, confirms that the modulation is generated in the plasma core, internal to r_{dep}, and propagates outwards. If local transport is modulated, important effects should be found in ∇T_e also. ∇T_e can be modulated either because local diffusivity χ_e is modulated at

constant heat flux ϕ, or because the heat flux itself oscillates. Since $n_e \nabla T_e = -\phi/\chi_e$, and assuming that n_e is constant, we get:

$$\frac{\nabla \tilde{T}_e}{\nabla T_{e,0}} \sim \frac{\tilde{\phi}}{\phi_0} - \frac{\tilde{\chi}_e}{\chi_{e,0}}$$

where $\nabla \tilde{T}_e$ is the amplitude of the oscillating gradient (obtained by FFT analysis of the incremental ratio of the T_e data), and $\nabla T_{e,0}$ is the gradient of the averaged profile. All other quantities have a similar meaning. $\tilde{\phi}$ is partly due to a sloshing flux possibly caused by re-adjustments of χ_e, vanishing on a time scale longer than local heat transfer time constant. Its contribution to fluctuating gradient is expected therefore to be negligible.

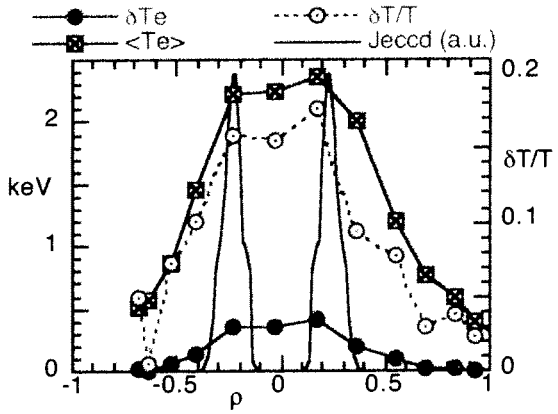

Fig.5 – Red full dots: amplitude of T_e oscillations synchronous to swinging. Green crossed squares: averaged T_e profile. Open red dots: relative change.

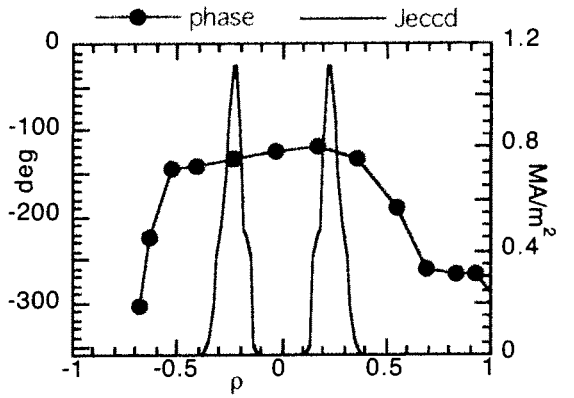

Fig.6 – Red full dots: phase of T_e oscillations synchronous to swinging. The ECCD profile (violet) is shown in both Fig.5 and Fig.6

The main contribution to $\tilde{\phi}$ is due to a feed-back from $\tilde{\chi}_e$ which modulates T_e, which modulates (in phase opposition to $\tilde{T}_e$) the ohmic input. We assume therefore that:

$$-\frac{\tilde{\chi}_e}{\chi_{e,0}} \sim \frac{\nabla \tilde{T}_e}{\nabla T_{e,0}} - \frac{\tilde{\phi}_{oh}}{\phi_{oh,0}}$$

The measured $\nabla \tilde{T}_e / \nabla T_{e,0}$ (FFT on T_e incremental ratio) and the relative heat flux modulation $\tilde{\phi}_{oh}/\phi_{oh,0}$, estimated on the basis of observed T_e fluctuations and assuming Spitzer resistivity, are shown in Fig.7. Outside r_{dep} the relative change of the gradient is fully explained by heat flux modulation. This is not the case in the whole region at r_{dep}, where gradient fluctuations are twice the flux oscillations. This implies that $\tilde{\chi}_e/\chi_{e,0}=0.5$ at r_{dep}. Inside r_{dep} both $\nabla \tilde{T}_e$ and $\nabla T_{e,0}$ are small, and the error in the measure prevents a reliable estimate of their ratio. However, the absence of a phase delay and of a damping of the heat wave at center with respect to r_{dep} supports the conclusion that transport is modulated in the whole region internal to r_{dep}. It has to be noted that T_e increases, and transport drops, during the co-injection phase, when shear is also low (Fig.8). The same result is obtained by the estimate of χ_e with power balance analysis. Fig.9 shows that $\chi_{e,PB}$ (at ρ=0.2) is modulated out of phase with respect to T_e, and in phase with magnetic shear modulation.

Consistent with χ_e modulation, a modulation of the global energy content W_e is also observed. The observed relative change $\tilde{W}_e/\langle W_e \rangle$=0.04, confirmed by 4% oscillation

amplitude measured in the diamagnetic signal, is compatible with a 40% change in electron diffusivity over a volume smaller than 25% of the total one, considering also that in the meantime in the same volume there is a loss of 40% in ohmic heating (modulated T_e). Global energy confinement behaviour is therefore consistent with the observed modulation of local thermal diffusivity.

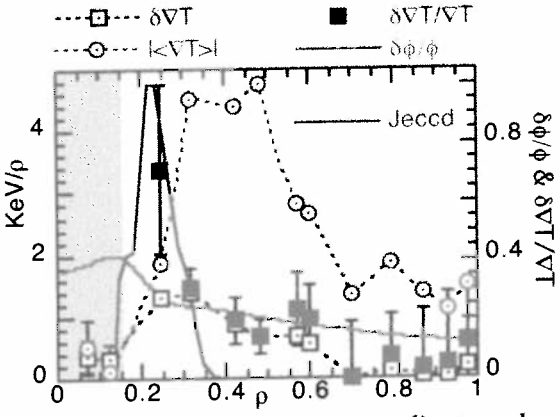

Fig.7 –∇T_e is the average T_e gradient, and $\delta\nabla T_e$ is the periodic component. Same meaning for of heat flux ϕ and $\delta\phi$.

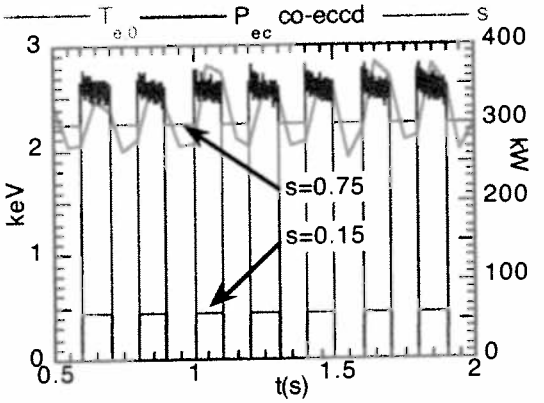

Fig.8 – $T_{e,0}$ (red) and confinement increase during the co-injection phase (P_{ec}), when shear s is the lowest.

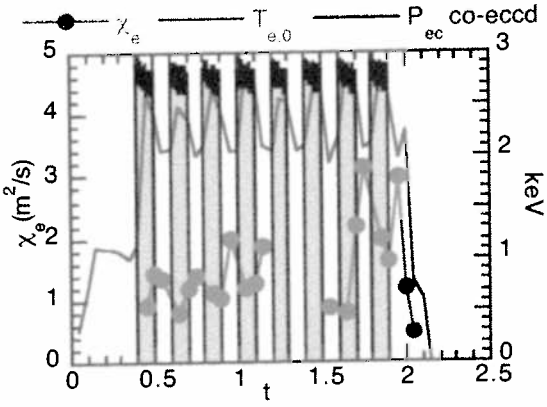

Fig.9 – In addition to the peak temperature and the EC power driving current in the co-direction, the figure shows the time dependence of the electron thermal diffusivity from power balance.

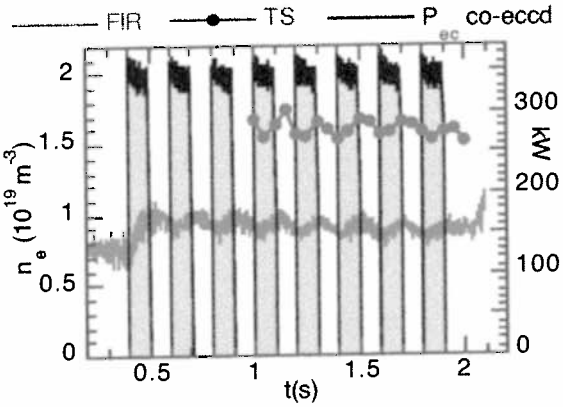

Fig.10 – Electron density from FIR interferometer, central chord, and from Thomson Scattering. P_{ec} for co-injection provides, as in the other figures, the time frame.

It has to be noted that $\tilde{T}_e$ modulation caused by $\tilde{\chi}_e$ is opposed by modulation of the ohmic input. At constant input power, the temperature change would have been much larger.
All the elements of thermal analysis converge to the point that a local decrease (≈60%) in the magnetic shear determines a decrease of the same amount (≈40%) in the electron thermal diffusivity at and inside r_{dep}.

5. Electron density modulation at constant particle sources

Although particle sources are likely constant during SECCD, electron density n_e is clearly modulated during these experiments. Since the equilibrium is modified with SECCD, we need

to take this into account, as in the analysis of electron temperature. However unlike the T_e measurement, changes in n_e measurements might be due not only to motion of Thomson Scattering (TS) observation point across magnetic surfaces, but also to thickening/rarefaction of flux surfaces at the same point, causing reduction/increase of the volume between surfaces.

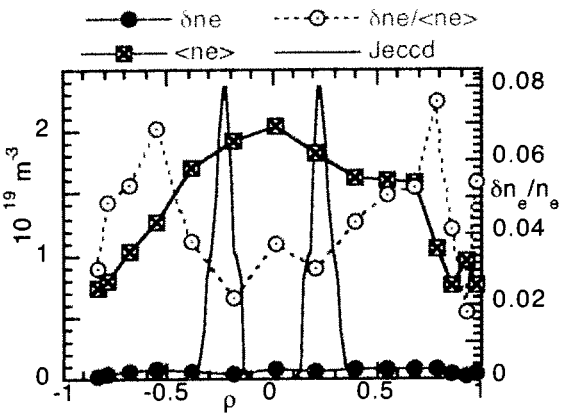

Fig.11 – Red full dots: amplitude of n_e oscillations synchronous to swinging. Green crossed squares: averaged n_e profile. Open red dots: relative change.

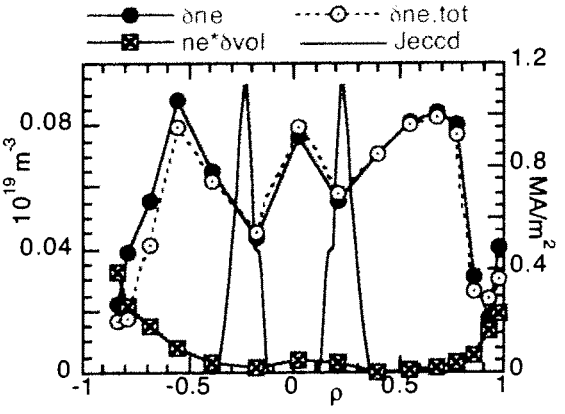

Fig.12 – Full dots: density oscillations. Crossed squares: δn_e due to volumetric effects. Open dots: total δn_e, corrected by equilibrium and volumetric effects.

Figure11 summarizes the results of the analysis of synchronous density oscillations performed by FFT of the TS density data corrected by equilibrium modulation (but not by volumetric effects). Density oscillation amplitudes are small (only a few percent), but outside the error bar given by the random noise in the FFT spectra. Figure 12 shows that the correction term due to volumetric effects is even smaller, densification/rarefaction of flux surfaces being peaked at the plasma periphery. It follows that we can neglect equilibrium volumetric effects on the density modulation.

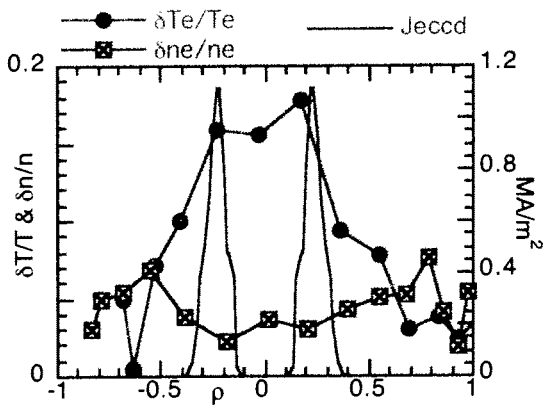

Fig.13 – Relative amplitude of T_e and n_e oscillations synchronous to swinging. Both data are corrected for equilibrium modulation effects. The ECCD profile is shown for reference

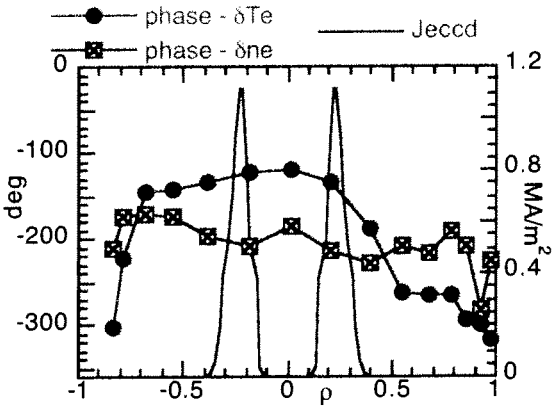

Fig.14 – Red full dots: phase radial profile of T_e oscillations synchronous to swinging. Green crossed squares: phase of n_e oscillations. Both data are corrected for equilibrium modulation effects.

If we compare amplitude and phase of T_e and n_e oscillations (Fig.13 and 15), we see that the two effects are both determined by SECCD, but as a result of different processes. $\tilde{T}_e$

oscillations are limited in the region inside the deposition radius, and possibly propagate outwards, while $\tilde{n}_e$ oscillations are originated in a broader region extending outside the deposition radius. The phase is also quite different in the two cases, confirming that different processes are going on in the two regions.
Because of the small relative amplitude of $\tilde{n}_e$, we can neglect their impact on $\tilde{T}_e$.

6. Conclusions

Electrodynamic calculations show that ±40% (from 0.15 to 0.75) shear modulation can be achieved at r_{dep} in Switching ECCD experiments on TCV. Shear modulation is localized at the CD layer. Internal inductance measurements and sawteeth activity evolution support the calculations.

In spite of the constant heating power, the presence of electron temperature oscillations show that electron transport is modulated at, and possibly inside, the SECCD layer. The observed ±40% relative amplitude of χ_e modulation is at the same level of the shear modulation amplitude.

An important result is that electron transport is reduced when shear is low. This provides useful information on the issue of magnetic shear destabilization of drift-waves [e.g. 4], and on the link between transport and fine-scale turbulence.

Small amplitude density oscillations are also observed during SECCD, although a process different from energy confinement is acting, possibly related to the $n_e(q)$ functional dependence.

Acknowledgement: This work was partially supported by the Swiss National Science Foundation

References

[1] F.Ryter, Nucl. Fusion **43** (2003) 1396–1404
[2] C Gormezano, Plasma Phys. Control. Fusion **41** (1999) B367–B380.
[3] Ulrich Stroth, Plasma Phys. Control. Fusion **40** (1998) 9–74
[4] A. Kendl and B. Scott, 29th EPS Conference on Plasma Phys. and Contr. Fusion Montreux, 17-21 June 2002 ECA Vol. **26B**, P-3.211 (2002)
[5] JW Connor and R J Hastie, Plasma Phys. Control. Fusion **46** (2004) 1501–1535
[6] F Jenko and A Kendl, New Journal of Physics 4 (2002)
[7] F Jenko and W Dorland, Plasma Phys. Control. Fusion 43 (2001) A141–A150
[8] B.D. Scott, Phys. Rev. Lett. 65, 3289 (1990)
[9] B.D. Scott, Plasma Phys. Contr. Fusion 39, 1635 (1997)
[10] R.C. Wolf, Nuclear Fusion, Vol. **41** (2001) 1259
[11] V.Erckmann et al., IAEA Proc.1995, Plasma Physics and Contr. Nuclear Fusion Research, Vol.1, p. 771-781, paper IAEA-CN-60/A6-3
[12] T. Goodmann et al., Fusion Technology (Proc. of 9th Symp. Lisbon 1996), North-Holland, Amsterdam (1997), 565.
[13] J.P. Hogge et al., Proc. of 12th Joint Workshop on ECE and ECRH, Aix-en Provence, France 2002, p.371.
[14] G.Ramponi et al., RADIO FREQUENCY POWER IN PLASMAS, 13th Topical Conference, Annapolis, Maryland (USA), April 1999, AIP Conf. Proc. 485 , 265 (1999)

Rapid eITB Formation during Magnetic Shear Reversal in fully non-inductive TCV Discharges

M.A. Henderson, Y. Camenen, S. Coda, E. Fable, T.P. Goodman, P. Nikkola, A. Pochelon, O. Sauter, C. Zucca, and the TCV team

Centre de Recherches en Physique des Plasmas CRPP EPFL
Association EURATOM-Confédération Suisse
CH-1015 Lausanne, Switzerland

e-mail contact of the first author: Mark.Henderson@epfl.ch

Abstract. A rapid formation of an electron internal transport barrier (eITB) is observed during a slow evolution (~200ms) from a centrally peaked to a hollow current density profile, while all external actuators remain constant. The time constant for the barrier formation appears to be shorter than the electron energy confinement time. The improved confinement associated with the barrier formation occurs first in a localized region off-axis. Then the effects propagate to inner and outer flux surfaces on a confinement time scale. The temporal and spatial localization of the barrier formation suggest a threshold in the magnetic shear profile, which triggers the onset of the eITB. The location of the barrier corresponds to the radial location of the zero-shear flux surface based on a Fokker-Planck code and, therefore, we assume that the inversion of the q-profile corresponds to the barrier formation in both time and space. A simplified model is presented that attempts to characterize the current profile evolution and correlates the onset of the barrier with the time at which the current profile becomes inverted.

1. Introduction

Generation of non-inductively driven electron Internal Transport Barriers (eITB)[1,2,3,4] on the Tokamak à Configuration Variable (TCV) initially starts with a steady-state Ohmic plasma discharge with the current density profile (j_P) peaked in the center. The plasma current is then sustained using co-Electron Cyclotron Current Drive (ECCD) deposited off-axis (ρ_{CD}~0.4, 1.0MW), which broadens j_P. The co-ECCD current density profile (j_{CD}) is flat or slightly hollow from the deposition location inward due to a strong particle diffusion[5]. The off-axis co-ECCD also broadens and increases the electron temperature (T_e), steepening the electron pressure gradient off-axis (∇P_e) and resulting in an increased bootstrap current (I_{BS}). The bootstrap current density profile (j_{BS}) is peaked off-axis, and combines with j_{CD} to generate a slightly hollow j_P. The transition from a peaked to hollow j_P profile occurs on a slow time scale (~200ms). Even though the applied external loop voltage is zero, the plasma inductance generates local electric fields that drive internal currents (j_I), which attempt to maintain the peaked j_P profile that existed before the co-ECCD turn on. j_I decreases with a time constant τ_{jI},

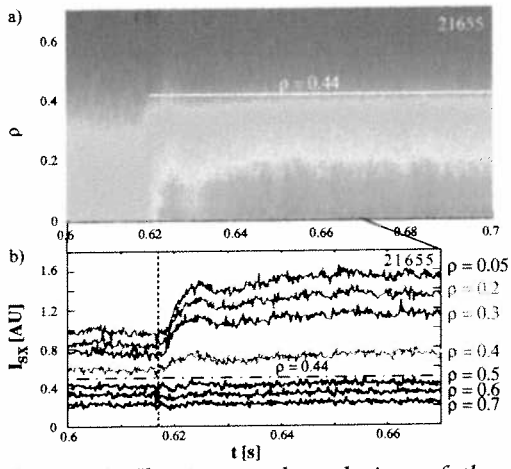

FIG. 1 a) The temporal evolution of the line-integrated soft x-ray emission across the plasma cross section, the eITB forms near 0.62s and b) viewed at selected values of ρ, during the eITB transition; the barrier foot position corresponds to the horizontal dashed-dotted line at ρ=0.44.[6]

governed by a combination of the current redistribution time and the plasma's L/R time constant. The transition from the centrally peaked to the hollow j_P is delayed until j_I is reduced to the point that it no longer fills in the hollow non-inductive current profile.

Despite the gradual evolution of the current profile and all external actuators being held constant, a rapid improvement in confinement is observed[6], see FIG. 1. The fast transition suggests the reaching of a threshold during the magnetic shear profile evolution, which triggers the onset of the eITB. We have determined the transition to occur at the moment at which the q profile becomes inverted. Unfortunately, there is no direct measurement of the local magnetic field line pitch angle on TCV, but simple modelling of the magnetic shear profile under equilibrium conditions and the of the current profile evolution, motivates the hypothesis that the rapid and localized barrier formation coincides with the appearance of the zero-shear (s=0) flux surface in time and space.

In the next section, the experimental evidence that the barrier forms rapidly and in a very localized region off-axis will be presented, with the position correlated to the modelled s=0 flux surface. Also, the formation of the barrier is shown to occur on an even faster time scale than the electron energy confinement time (τ_{eE}). In the third section a simplified model of the current profile evolution is presented, which approximates the three source current components: inductive, ECCD and bootstrap. The barrier's appearance is correlated with the inversion of the modelled current profile and the confinement enhancement is proportional to the modelled depth of the hollow j_P. Conclusions are offered at the end of this paper.

2. Spatial and temporal formation of the barrier

A typical eITB discharge from the turn on of the ECCD to a nearly steady state regime is shown in FIG. 2. The co-ECCD (1.0MW) is initiated at 0.4s, and at 0.42s all external actuators (including the ohmic transformer current, I_{OH}) are held constant. After 0.42s the plasma current is sustained by only I_{CD}, I_{BS} and I_I, and evolves from a peaked to hollow current profile as I_I decays on τ_{jI} scale. Approximately 200ms after the I_{OH} is held constant, a transition to the improved confinement regime is observed between 0.6 and 0.65s by the increase in the central electron temperature (T_{e0}), the electron energy confinement time (τ_{eE}) and the confinement enhancement factor, H_{RLW} ($=\tau_{eE}/\tau_{RLW}$)[7,8], see FIG. 2. Unfortunately, T_e and τ_{eE} are obtained on the Thomson Scattering (TS) diagnostic acquisition rate of 20Hz and can not resolve the rapid barrier formation evidenced by the soft x-ray emission (measured by a multiwire chamber proportional x-ray detector, MPX) of FIG. 1 and 2c, which occurs at t_T~0.618s. The barrier formation improves the confinement in the center as the emission from inner chords relative to ρ=0.44 increases, while the outer viewing chords register a momentary decrease as the barrier reduces the energy flux from the core to the outside, see FIG. 1b. The median radial location between the chords

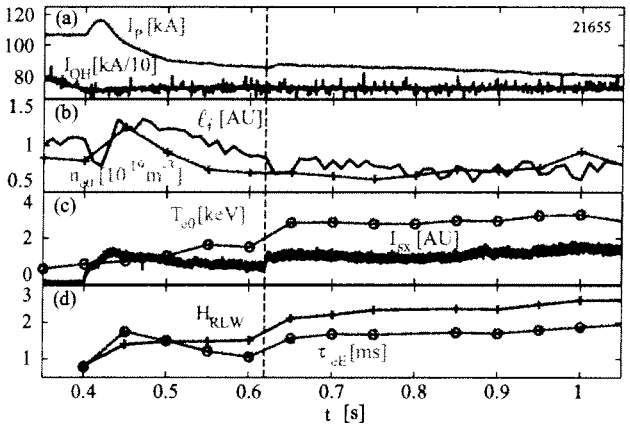

FIG. 2. Typical eITB discharge with the improved confinement starting at 0.62s, including a) ohmic transformer coil current and plasma current; b) internal inductance and central electron density; c) I_{SX} and central T_e, and d) H_{RLW} and τ_{eE}..

along which the emission respectively the increases and decreases corresponds to the barrier foot location, defined as the radial location of the maximum in ρ^*_T[9], which we refer to as ρ_{ρ^*}[10] (dashed line of FIG. 1b). The ρ^*_T parameter is defined as:

$$\rho^*_T = \rho_s / L_{Te}$$

where $L_{Te}=-T_e/(\partial T_e/\partial r)$ is the local temperature gradient scale length, $\rho_s=c_s/\omega_{ci}$ is the ion Larmor radius at the sound speed c_s ω_{ci} is the ion cyclotron angular frequency. After its inception the barrier's radial location remains stable until additional heating or counter-ECCD is applied in the center at 1.1s (not shown).

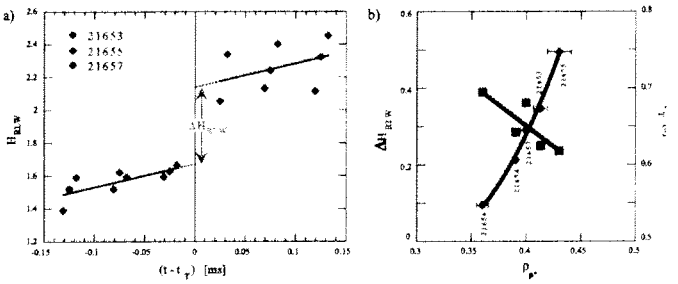

FIG. 3 a) The enhancement factor, H_{RLW} versus the time relative to the eITB formation time, t_T, for three different discharges. b) The step in confinement enhancement at t_T is correlated with the radial location (red curve) of the barrier formation. The time t_T (blue curve) is earlier for broader barriers.

Even though H_{RLW} is calculated on the TS acquisition rate, the rapid transition can also be observed by assembling several similar shots and plotting H_{RLW} at each TS acquisition time relative to t_T, see FIG. 3a. A gradual improvement in confinement is observed leading up to t_T, and then a rapid increase in H_{RLW} of magnitude ΔH_{RLW} occurs. There is a slight variation in ΔH_{RLW} for the three discharges, which can be attributed to the formation of the barrier at slightly different radial locations from shot-to-shot. If the barrier forms at a larger radius, the whole volume inside that radius will experience the improved confinement resulting in a greater step in ΔH_{RLW} as shown in FIG. 3b. It appears that ΔH_{RLW} depends on $\rho_{\rho^*}^2$ (proportional to the enclosed volume) as shown in FIG. 3b (red curve), consistent with the eITB figure of merit proposed in reference [10].

The chord-integrated I_{SX} seems to indicate a uniform increase across the whole core; however, chords viewing the plasma axis cannot distinguish between an increase at the center and an increase near the barrier. A recently upgraded MPX camera, viewing the entire plasma cross section, is used to obtain a local emissivity profile (ε_{SX}) by inverting the integrated profile, assuming a constant emissivity on a given flux surface and using a minimum Fisher inversion method[11]. The inverted profiles, averaged over 0.25ms and plotted at 0.75ms time intervals, are shown in FIG. 4a. The relative intensity (normalized to pre-eITB levels) for selected radial locations may then be plotted as a function of time, see FIG. 4b. An increase in the soft x-ray emission is first observed in the region of $\rho\sim0.3$, then progresses inward toward the center and outward toward the barrier foot. We chose to estimate the propagation time by fitting (solid line) the relative intensity change at each radial position to a hyperbolic tangent: $\varepsilon_{SX}(\rho)$ =

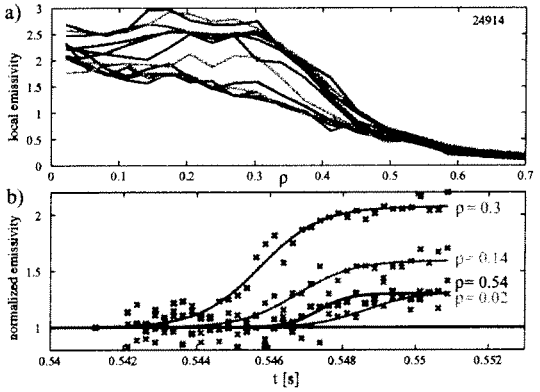

FIG. 4 a) The reconstructed ε_{SX} profiles averaged over 0.25s and plotted every 0.75ms during the eITB transition. b) The temporal evolution of ε_{SX} normalized and plotted for selected radial locations. The barrier forms first around $\rho\sim0.3$.

$\tanh[(t-t_T(\rho))/\tau_F(\rho)]$, where $\varepsilon_{SX}(\rho)$ corresponds to the amplitude rise, $t_T(\rho)$ the inflection point of the rise and $\tau_F(\rho)$ the rise time for the given flux surface ρ. The time of the initial rise of $\varepsilon_{SX}(\rho)$ at each radial location is approximated by $t_T(\rho)-\tau_F(\rho)$ and is plotted as a function of ρ in FIG. 5a. The increase in $\varepsilon_{SX}(\rho)$ occurs first at $\rho\sim0.3$, which can be attributed to a local decrease in thermal diffusivity, i.e. the formation of a barrier. As time progresses, neighbouring flux surfaces are influenced as the barrier "dams" the thermal flux resulting in a build-up of the local temperature. The inward and outward propagating effects of the barrier formation of FIG. 5a result in a relatively sharp "V" rather than a "U" shape indicating that the barrier width is very narrow (~0.05 in ρ or 1.2cm). The flat T_e profiles typical of the region contained inside eITBs[2,12] also indicate that the diffusivity is comparably higher inside $\rho<0.3$ than at the barrier. The barrier is located at the edge of the ε_{SX} or T_e flat top and not farther out at ρ_{ITB}[13] near the barrier foot ($\rho=0.44$ of FIG. 1b) characterized by the radial location of unchanging I_{SX}-chords.

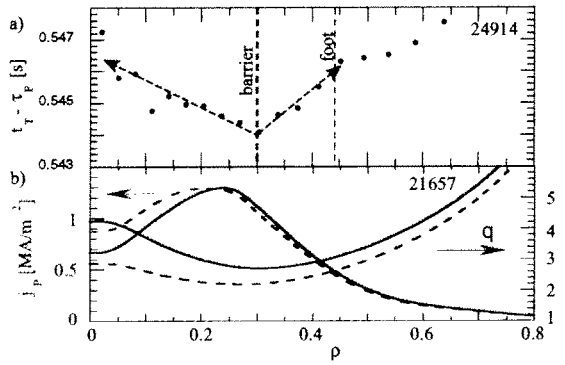

FIG 5 a) The fitted rise time (t_T-τ_F) of ε_{SX}: the barrier forms at $\rho\sim0.3$ (vertical dashed line) and the effects then propagate inward (blue line) and outward (green line). b) Calculated j_P and q-profile from the CQL3D code for shot #21657 (equivalent to #21655 and 24914 but in equilibrium conditions).

The j_P (red curves) and q profiles (blue curves) of FIG. 5b were calculated using the Fokker-Planck code, CQL3D[14] for an equivalent shot (#21657) after steady-state conditions were achieved. The calculations assumed two different averaged effective charge values, $Z_{eff}=5$ (solid) and 2.5 (dashed). In each case the diffusion coefficient (D) was chosen in such a way as to best reproduce the experimental total plasma current, *e.g.* D=0.5 m^2/s (solid) and 0.7 m^2/s (dashed)[15]. In both cases the zero-shear ($s=0$) flux surface occurs near $\rho\sim0.3$, equivalent to the barrier location $\rho_B\sim0.3$ of FIG. 5a. Since the barrier location corresponds to the modelled $s=0$ and the barrier position remains stable, it is reasonable to hypothesize that the threshold, which triggers the barrier formation, corresponds to the appearance of a zero-shear magnetic flux surface[6], i.e. that the barrier forms when and where $s=0$.

The step in confinement enhancement from the rise on the soft x-ray emission of FIG. 1 appears to occur on the order of τ_{eE}. However, if the transition occurred instantaneously, the increase in stored energy would occur on a similar τ_{eE} time scale, indicating that the formation of the barrier may occur at an even faster rate. In order to discern the formation speed, the confinement improvement is modelled as a function of time and of the barrier's formation time constant τ_F as follows:

$$\tau_{eE}(t) = \tau_{eE0} + \Delta\tau_{eE}(1+\tanh((t-\tau_F)/\tau_F))$$

where τ_{eE0} represents the initial global confinement time and $\Delta\tau_{eE}$ is the corresponding step associated with the onset of the eITB. The experimentally measured values are used for both τ_{eE0} and $\Delta\tau_{eE}$. The corresponding increase in the local soft x-ray emission can then be modelled as follows:

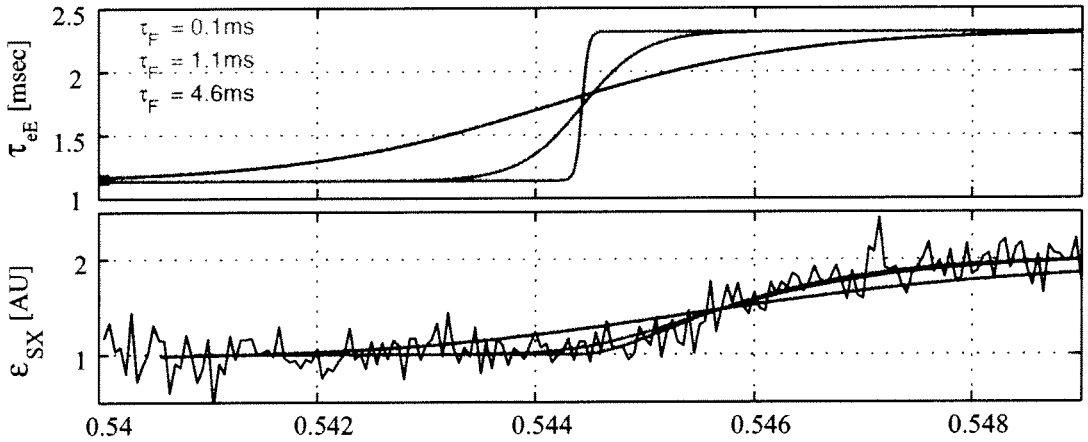

FIG. 6 a) the modelled step in confinement at τ_F with the three chosen transition times $\tau_F=\tau_{eE}/20$ (red), τ_{eE} (green) and $4\tau_{eE}$ (blue). b) The modelled local soft x-ray emissivity for the three choices of τ_{eE} is compared to the experimental reconstructed local soft x-ray (black).

$$\varepsilon_{mod}(t) = \sum_{t_i=0}^{t} \varepsilon_0 \, e^{-(t-t_i)/\tau_{eE}(t_i)}$$

where ε_{mod} is the soft x-ray emission, ε_0 is the normalized reconstructed local emissivity, and t_i is the interval time step chosen to be small relative to the confinement time scale. An example of three barrier formation rates: $\tau_F = \tau_{eE}/20$ (red), $\tau_F = \tau_{eE}$ (green) and $\tau_F = 4\tau_{eE}$, are shown in FIG. 6a, with the corresponding modelled response in FIG. 6b along with the reconstructed local emissivity at ρ=0.3. The formation speed, can be estimated by choosing the value of τ_F that minimized the difference between ε_{mod} and ε_{SX} (Exp.). This was performed for each radial location of the reconstructed emissivity profiles. In the region near the barrier formation, τ_F <0.2ms (or $<\tau_{eE}/10$), which is nearly three orders of magnitude faster than the current evolution time scale τ_I. Note that the resolution of τ_F is limited to the MPX acquisition rate for this discharge (20kHz).

3. Current profile evolution

Since no direct measurement of the local magnetic field line pitch angle exists on TCV, we can only attempt to estimate the current density profiles through calculated and modelled profiles of the different source currents. After the current in the transformer coil is held constant, the plasma current is maintained by the sum of I_{CD} (net co-ECCD current), I_{BS} (net bootstrap current) and I_I (net current from the induced electric fields from the plasma inductance). I_{BS} can be calculated from the T_e and n_e profiles[16], and the time evolution of I_{CD} and I_I can be approximated using the following expression:

$$I_P(t) - I_{BS}(t) = c_1 \frac{T_e(\rho_{CD}, t)}{ne(\rho CD, t)} + c_2 e^{-\frac{(t-0.42s)}{\tau_{jI}}}$$

where the first term represents the EC driven current (I_{CD}) and the second term the inductively induced currents that decay on a τ_{jI} scale. I_P is the measured total plasma current, and ρ_{CD} is the co-ECCD deposition location. The constants c_1, c_2 along with τ_{jI} are obtained from an optimization routine that minimizes the difference between the measured and modelled currents. The evolution of the measured, calculated and modelled sources is shown in FIG. 7a for a similar discharge (#21654). At 1.1s central heating is added which increases the central

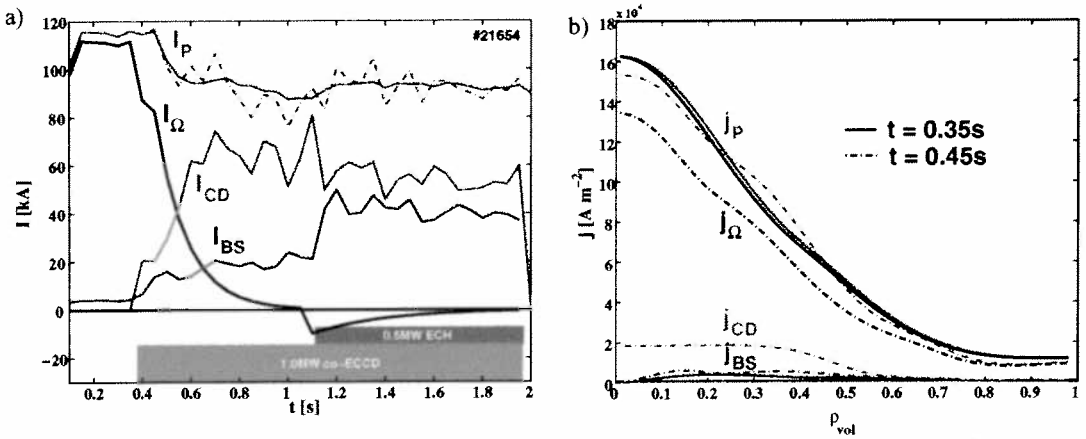

FIG. 7 a) Time evolution of the plasma current compared with the modelled contributions of I_{BS} (blue), I_{CD} (green), I_Ω + I_I (black) and their sum (red-dashed). b) The reconstructed current density profiles before and after the current in the transformer coil is held constant.

temperature, steepening the pressure gradient and increasing the driven bootstrap current. Again, the inductive nature of the plasma prevents rapid changes in the current profile, and a negative I_I is driven by the internal electric fields that then decay in time. The above minimization procedure is repeated during the central heated phase as shown in FIG. 7a. Once the magnitudes of the different current sources have been determined, the current density profiles can then be reconstructed. The profile shape of j_{CD}[15] is supplied by CQL3D, j_I at t=0.42s can then be calculated by subtracting (j_{CD}+j_{BS}) at t=0.42s+δ (where δ is a small time step) from j_{BS}+j_Ω at t=0.42s-δ, see FIG. 7b. Note that j_Ω is taken to be proportional to $T_e^{3/2}$, with the absolute amplitude constrained by the measured total current. Finally we can write $j_I = j_I(\rho)*e^{-(t-0.42)/\tau jI}$ from t=0.42 to 1.1s, and at 1.1s the process is repeated to obtain the complete profile evolution throughout the discharge. The modelled j_P becomes hollow between 0.6 and 0.65s consistent with the barrier formation near 0.64s (for #21654), see FIG. 8a. Although this is a simplified model of the complex evolution of j_P, the transition from a peaked to a hollow modelled j_P occurs consistently near the formation of the barrier for the five discharges analyzed. Hence it is reasonable to infer that the barrier forms once an s=0 surface appears in the plasma, which occurs soon after the j_P profile is inverted[6].

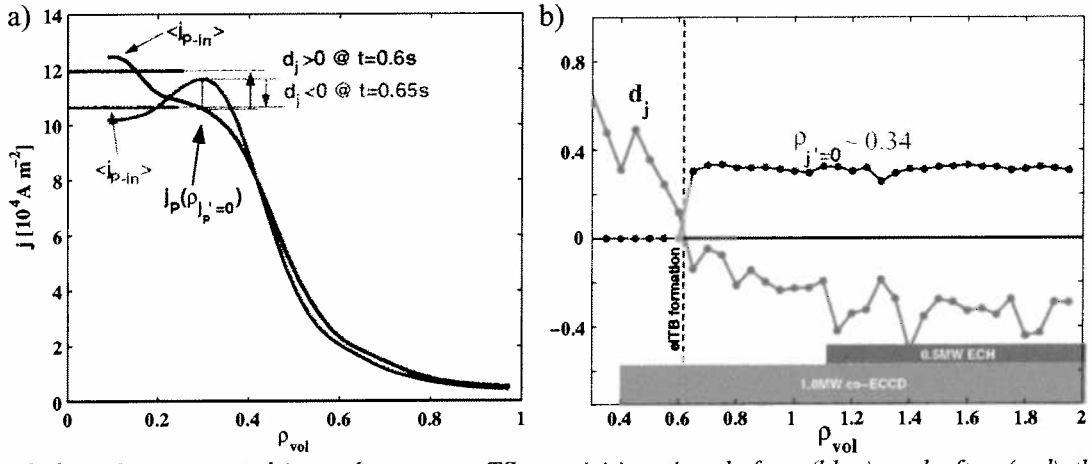

FIG. 8 a) Reconstructed j_P at the nearest TS acquisition time before (blue) and after (red) the barrier formation at t_T. b) The temporal evolution of d_j (height or depth of current center) during discharge #21654. t_T is represented by the red vertical dashed-line.

The depth of the hollow current profile can be characterized by $d_j = (j_{P\text{-}in} - j_{P\text{-}B})/ j_{P\text{-}B}$, where $j_{P\text{-}in}$ is the average current density inside $\rho = \rho_{jp'=0}$ (the radial location of the off axis maximum in j_P) and $j_{P\text{-}B}$ is the local current density at $\rho = \rho_{jp'=0}$. The evolution of both d_j and $\rho_{jp'=0}$ is shown in FIG. 8b, where the eITB transition occurs when d_j becomes negative. Note that the modelled j_P is strongly affected by the fluctuations in the T_e measurements, which provide the estimated j_{CD} and j_{BS} profiles. The average value of d_j was calculated for each discharge of FIG. 3b between 0.8 and 1.1s and plotted against the average maximum of ρ^* (referred to as the barrier strength, ρ^*_{max}), see FIG. 9. The results suggest a threshold in improved confinement once $d_j<0$ as well as when $\rho^*_{max}>0.04$[10]. The results further suggest that the improved confinement increases as the current profile (and q-profile) becomes more hollow (i.e. more inverted). However, the barrier width does not increase in size (as would be expected if the confinement increases with negative shear, but appears to remains relatively narrow at the zero shear flux surface. Therefore, the local improved confinement associated with the barrier improves with increasing ds/dr at the zero shear flux surface.

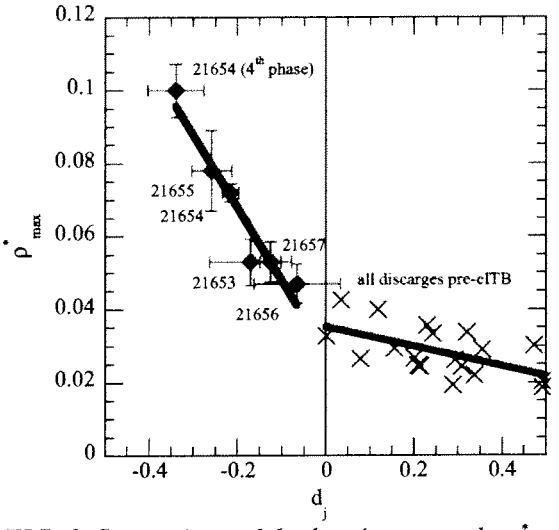

FIG. 9 Comparison of the barrier strength, ρ^*_{max} versus d_j averaged after the barrier formation (red) and at each TS acquisition time before the transition (blue) for the same discharges of FIG. 3b.

4. Conclusions

In conclusion, a rapid and localized formation of an internal transport barrier is observed during a slow evolution of the current density profile. The current profile evolution occurs on a relatively slow time scale, >200ms, from a well-defined peaked inductive ohmic profile to a steady-state fully non-inductively sustained hollow profile while all external actuators are held constant. The magnetic shear evolves on a similar time scale from a monotonically increasing to inverted profile. During this evolution, an internal transport barrier forms rapidly (<0.2ms) in a very narrow region off-axis. The barrier remains relatively stable at this location and the confinement improvement increases with the volume enclosed within the improved confinement region.

The barrier position is correlated to the zero shear flux surface according to the q profile modelled with CQL3D. A simplified model of the current profile evolution estimates the inversion of the current profile to occur when the barrier forms. The combination of the two models supports the hypothesis that the barrier forms when and where a zero shear flux surface appears[6]. The barrier strength, which is characterized as the maximum in the ρ^*_T parameter, increases linearly with the depth of the modelled current, implying that the barrier strength could be roughly proportional to ds/dr at the zero-shear flux surface. Here we have not invoked anything other than a local increase in confinement at a radial position corresponding to s=0 to explain the experimental data. The dual aspects of a rapid localized formation of the barrier at the modelled zero-shear flux surface and the barrier strength dependence on the ds/dr have yet to be incorporated in a single theory on internal transport barriers.

Acknowledgement:
The authors would like to acknowledge Basil Duval who helped greatly in proof reading and in numerous discussions concerning the organization of this manuscript. Also, Roland Behn and Ge Zhuang are to be acknowledged for their work with the Thomson Scattering diagnostic and Alexei Sushkov for his work with the MPX soft x-ray diagnostic. This work was partially supported by the Swiss National Science Foundation

---

Appendix 1: References

[1] S. Coda *et al*, "High-power ECH and fully non-inductive operation with ECCD in the TCV tokamak", Plasma Phys. Control. Fusion **42** (2000) B311.
[2] O. Sauter *et al*, "Electron ITB in fully non-inductive reverse shear scenarios", Proc. 29th EPS Conf. on Controlled Fusion and Plasma Physics (Montreux, 2002), Europhysics Conf. Abstr. **26B** (2002) P2-087.
[3] T.P. Goodman *et al*, "An overview of results from the TCV tokamak", Nucl. Fusion **43** (2003) 1619.
[4] M.A. Henderson *et al*, "Recent results from the electron cyclotron heated plasmas in Tokamak à configuration Variable (TCV)", Phys. Plasmas **10** (2003) 1796.
[5] P. Nikkola *et al*, "Modelling of the electron cyclotron current drive experiments in the TCV tokamak", Nucl. Fusion **43** (2003) 1343.
[6] M.A. Henderson *et al*, "Rapid and localized eITB formation during shear inversion in fully non-inductive TCV discharges", to be published in Phys. Rev. Lett (2004).
[7] P.H. Rebut, P.P. Lallia and M.L. Watkins, "The critical temperature gradient model of plasma transport: Applications to JET and future tokamaks", Proc. 12th Int. Conf. of Plasma Phys. and Cont. Fusion Res., **2** (IAEA, Vienna, 1989) p.191.
[8] A. Pochelon *et al*, "Energy confinement and MHD activity in shaped TCV plasmas with localized electron cyclotron heating", Nucl. Fusion **39** (1999) 1807.
[9] G. Tresset *et al*, "A dimensionless criterion for characterizing internal transport barriers in JET", Nucl. Fusion **42** (2002) 520.
[10] M.A. Henderson *et al*, "Control of electron internal transport barriers in TCV", Plasma Phys. Control. Fusion **46** (2004) A275.
[11] M. Anton *et al*, "X-ray tomography on the TCV tokamak", Plasma Phys. Control. Fusion **38** (1996) 1849.
[12] T. Fujita *et al*, "High performance experiments in JT-60U reversed shear discharges",Nucl. Fusion **39** (1999) 1627.
[13] B. Esposito *et al*, "JET internal transport barriers: experiment vs theory", Plasma Phys. Control. Fusion **45** (2003) 933.
[14] R.W. Harvey and M.G. McCoy, "The Fokker-Planck CQL3D code" in *Proceedings of the IAEA Technical Committee Meeting on Numerical Modeling of Plasmas, Montreal*, 1992 (IAEA, Vienna, 1993).
[15] P. Nikkola, "The effect of electron transport on electron cyclotron current drive in tokamak plasmas", EPFL Thesis No. 3048 (2004).
[16] O. Sauter, C. Angioni and Y.R. Lin-Liu, "Neoclassical conductivity and bootstrap current formulas for general axisymmetric equilibria and arbitrary collisionality regime", Phys. Plasmas **6** (1999) 2834.

H-mode Threshold Power Dependences in ITPA Threshold Database

ITPA H-mode Threshold Database Working Group 1), presented by Y.R.Martin 2)

1) from Alcator C-Mod: J.A.Snipes, M.Greenwald;
ASDEX/ASDEX Upgrade: F.Ryter, O.J.W.F.Kardaun, J.Stober;
COMPASS-D/MAST: M.Valovic;
DIII-D: J.C.DeBoo;
JET/EFDA: Y.Andrew, J.G.Cordey, R.Sartori, K.Thomsen;
JFT-2M/JT-60U: T.Takizuka, Y.Miura, T.Fukuda, Y.Kamada, K.Shinohara, K.Tsuzuki;
PBX-M/NSTX: S.M.Kaye, C.Bush, R.Maingi;
TCV: Y.R.Martin;
TUMAN-3M: S.Lebedev.

2) CRPP, Association EURATOM-Confédération Suisse, EPFL, CH-1015 Lausanne, Switzerland

e-mail contact of main author: yves.martin@epfl.ch

Abstract.

Newly contributed data and the current status of the International H-mode threshold database are presented. Selecting data from only one divertor geometry per tokamak leads to a reduction in the data scattering and improves the quality of the fits. The selection of a reduced set of transition types also leads to fit improvement. A new parameter, (R+a)/(R-a), is introduced in the power law scaling to account for the data provided by the spherical tokamaks. A prediction for ITER is given for the different power law scalings. Threshold power for ITER is estimated at about 35MW.

1. Introduction

The ELMy H-mode is obtained in many tokamaks. Its good confinement properties together with its good impurity removal make it the nominal operational regime for ITER. It is widely accepted that the transition from L-mode to H-mode (LH transition) is obtained when the input power exceeds a threshold, which depends on the plasma density and the magnetic field [1,2]. The threshold power was generally found to be lower when the plasma is shaped in a single null diverted configuration with the ion gradB drift directed towards the X-point. Finally, it also depends on other parameters such as the plasma shape, the neutral density or the vacuum vessel conditioning, but in a less clear manner.

The comparison of the threshold power measured in different tokamaks under different conditions has shown a relationship between that power and the plasma size. Therefore, data from a series of tokamaks have been collected into one database to analyse the size dependence of the H-mode threshold power. After data selection, power law scalings were deduced, including the plasma density, magnetic field and parameters describing the plasma size. Finally, the power law scaling is used for extrapolation to new devices such as ITER. Practically, the international H-mode threshold database (IGDBTH), initiated in 1992 and summarised in [3], now contains data from 13 tokamaks: Alcator C-Mod, ASDEX, ASDEX Upgrade, Compass, DIII-D, JET, JFT-2M, JT-60U, MAST, NSTX, PBX-M, TCV and TUMAN-3M.

In the analyses, the experimental threshold power is approximated by the loss power P_L measured just before the transition. $P_L=P_{OHM} + P_{AUX}$ - dW/dt (PLTH in database) where P_{OHM} is the Ohmic power [MW], P_{AUX} the absorbed auxiliary heating power [MW] and dW/dt the time derivative of the total plasma energy [MJ/s]. At the last IAEA conference, two power law scalings were presented. They were based on data from 9 tokamaks (ASDEX, ASDEX Upgrade, Alcator C-Mod, COMPASS-D, DIII-D, JET, JFT-2M, JT-60U, TCV) and their expressions were [4]:

$$P_{th1} = 1.67\, n_{e20}^{0.61}\, B_T^{0.78}\, a^{0.89}\, R^{0.94} \qquad \text{RMSE=25.1\%} \qquad (1)$$

$$P_{th2} = 0.05\, n_{e20}^{0.46}\, B_T^{0.87}\, S^{0.84} \qquad \text{RMSE=26.0\%} \qquad (2)$$

where P_{th}, n_{e20}, B_T, a, R, and S are respectively the predicted threshold power [MW], plasma density [$10^{20}m^{-3}$], magnetic field [T], minor radius [m], major radius [m] and plasma outer flux surface area [m^2].

Since 2002, new data have been added to the database. This paper introduces the new data and summarises the present status of the database. It then shows the analysis of the database, the criteria used for data selection and to the parameter selection to reduce the Root Mean Square Error (RMSE) of the fit. The role of the effective charge (Z_{eff}) and the absolute B was studied in [5] and will not be discussed here. Finally, a new estimation of the prediction for ITER is given.

2. New Data

New time slices were provided by ASDEX Upgrade (17 new time slices), Alcator C-Mod (79), JET (555), MAST (6), NSTX (6) and TCV (13). The ASDEX Upgrade new contribution consists of transitions obtained at low density. For Alcator C-Mod, LH transitions in inner wall limited, inner nose limited, single null and double null configurations, as well as low density time slices were provided. New JET data points come from 2002 and 2003 campaigns with the MKII GB (SRP) divertor as well as 2001 discharges performed in H or He. The MAST contribution comes from new double null discharges. A first set of data points was provided by NSTX. Data taken at LH transitions obtained in ohmic power ramps were provided by TCV as well as one LH transition obtained with ECH. The database now contains 7673 time slices.

At the beginning of the study presented in this paper, the data selection includes the largest possible data set. The phases taken into account are LD (D for dithering), DH and LH transitions, D for data points during the dithering phase and LDL, LHL for brief attempts to reach the H-mode. Data selection is restricted to time slices taken from plasmas in "appropriate conditions", as defined by a series of flags (SELDB). "Appropriate conditions" refers to single null configuration with ion gradB drift directed towards the X-point, a D_2 plasma with low radiated power. To avoid an increased threshold, the safety factor must be above 2.5, the density above a value defined in each tokamak and the plasma wall distance large enough. Exceptions to this rule were allowed to either extend the study to such parameters or avoid elimination of a complete data set provided by a particular device. For instance, the Single Null condition would reject all Tuman-3M data. Therefore, an exception was made for the corresponding data points to maintain them in the preliminary analysis.

Table 1 shows a comparison of the contribution from the different tokamaks in the selected datasets. The improvement from 665 to 1339 time slices comes from the new data contributions, as listed at the beginning of the section, and from the extension of the dataset.

The exceptions to the "appropriate conditions" are: 2 entries in Hydrogen plasmas and 29 in Helium for JET; 24 data points in Double Null configuration for JET, 15 for MAST and 5 for PBX-M; 15 time slices in Limited configuration for TUMAN-3M; 46 entries with unfavourable ion gradB drift for Alcator C-Mod.

A second data set was defined under the name IAEA04R. It contains all data in "appropriate conditions" and only those exceptions which keep the diversity of the database. As an example, MAST and PBX-M Double Null data are kept but JET Double Null data are rejected. JET non D_2 data are also rejected. This restricted data set contains 1298 entries.

TABLE 1: Contributions from tokamaks to the full dataset on LH transitions

Tokamak	IAEA02	IAEA04
ASDEX	37	43
ASDEX Upgrade	172	232
Alcator C-Mod	130	230
COMPASS-D	8	18
DIII-D	55	58
JET	118	610
JFT-2M	41	53
JT-60U	58	58
MAST		20
NSTX		6
PBX-M	5	5
TCV	41	51
TUMAN-3M		15
Total	**665**	**1399**

3. DataBase Status

The database completed with all new data is referred to as IGDBTH4v4. It contains 7673 entries. Among those, 1399 time slices belong to the large dataset as described above. The remaining time slices either belong to other phases of a discharge (L-mode, H-mode or HL transition) or have at least one parameter which is outside the "appropriate conditions". The restricted dataset contains 1298 time slices. All are in D2 working gas. All are in Single Null configuration but those from MAST (15 DN), PBX-M (5 DN) and TUMAN-3M (15

TABLE 2: Number of data points for all PHASE and TOKAMAK

	PHASE								
Count	D	DH	LD	LDL	LH	LHL	OHMD	OHMH	
ASDEX	0	0	0	0	37	6	0	0	43
AUG	18	6	89	22	82	0	10	5	232
CMOD	46	0	24	0	49	3	27	35	184
COMPASS	10	0	1	0	0	0	6	1	18
D3D	1	2	0	0	53	0	0	2	58
JET	226	66	91	0	172	0	0	0	555
JFT2M	12	0	6	0	35	0	0	0	53
JT60U	0	0	36	0	22	0	0	0	58
MAST	0	0	0	0	4	0	16	0	20
NSTX	1	0	0	0	5	0	0	0	6
PBXM	0	0	0	0	5	0	0	0	5
TCV	0	20	0	0	1	0	16	14	51
TUMAN-3M	0	0	0	0	0	0	0	15	15
	314	94	247	22	465	9	75	72	1298

LIM). All are in favourable ion Grad B drift but those in Double Null configuration.

The parameter PHASE describes more precisely in which part of the L-mode to H-mode transition the time slice was taken. OHM, L, D, H refer to Ohmic, L-mode, Dithering and H-mode, respectively, all combinations of these references indicate transitions from one to the next state. Usually data corresponding to a transition are taken just before its occurrence. A 'D' alone represents a time slice taken during the dithering phase. Table 2 shows the contribution of all tokamaks through the different PHASEs.

As shown in Table 2, the restricted data set contains 712 entries at LD or LH transitions (55%). 147 time slices (11%) also correspond to the transition out of the L-mode but are obtained in ohmic condition. 408 data points (32%) are taken during the dithering phase which is considered as being at the threshold as well. The remaining 31 entries (2%) are also considered as at the threshold since they show an attempt to go in H-mode even if they return to L-mode soon after.

Figure 1a and 1b show the distribution of the plasma density and magnetic field, respectively, for each device. The high magnetic field capability of Alcator C-Mod is clearly visible in both magnetic field and plasma density distributions. The magnetic field is quite uniform for half the tokamaks.

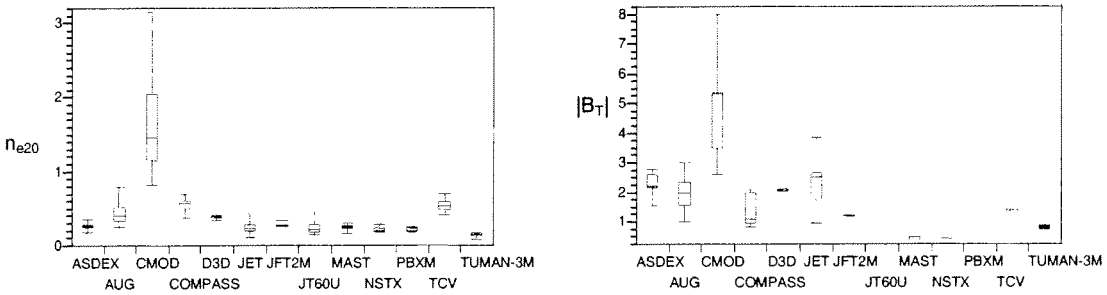

Figure 1: Distribution of plasma density and magnetic field for each tokamak. Quantile box plots indicate the minimum, 25%, 50 %, 75% and maximum of the distribution.

4. Analysis

4.1 General fit

The fits for the threshold power were generally based on two sets of variables: [n_{e20}, B_T, a, R] and [n_{e20}, B_T, S]. In this paper the first one will be used as a reference. With the restricted data set (1298 data points because of missing data), the fit gives:

$$P_{th3} = 3.46\ n_{e20}^{0.48}\ B_T^{0.65}\ a^{1.37}\ R^{0.26} \qquad \text{RMSE=32.4\%} \qquad (3)$$

The a and R dependences are significantly different from fit (1). However, since most tokamaks have the same aspect ratio, the roles of a and R are quite exchangeable and then the size dependence is comparable. This correlation of a and R can only be removed with a larger contribution from the Spherical Tokamaks. Nevertheless, it is their presence in the fit which already induces the change in the expression. The influence of Spherical Tokamaks on the fit will be addressed later.

The deviation of the actual threshold power (P_L) from the fit is shown in Fig.2. Data from TUMAN-3M remain out of the fit and the excess in the threshold is due to the fact that all data points are taken while in limited configuration. NSTX also show an excessive threshold power with this set of variables. Data points from spherical tokamaks (NSTX and

MAST) and TUMAN-3M are therefore removed from the data set to analyse the effect of the divertor type among conventional tokamaks operating in diverted configuration.

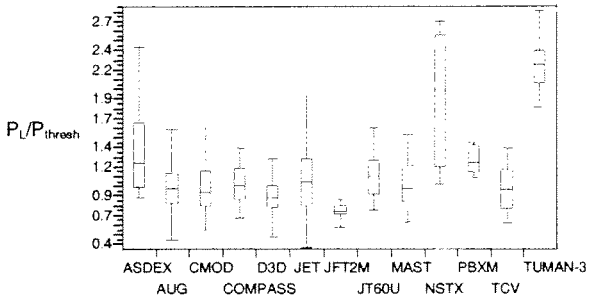

Figure 2: Deviation of the threshold power from the fit for each tokamak

4.2 Effect of divertor

The database contains a variable indicating the name of the divertor which was used for the experiments (DIVNAME). The effect of the divertor shape can then be treated and used for data selection. Figure 3 shows the deviation of the threshold power as a function of the divertor name for JET data.

LH transitions in plasmas with Mk0, MkI or MkIIap divertors have an average threshold power below the value given by the fit (1). Since the database contains a larger variety of data points with the MkIIap divertor, these time slices will be used in further analysis.

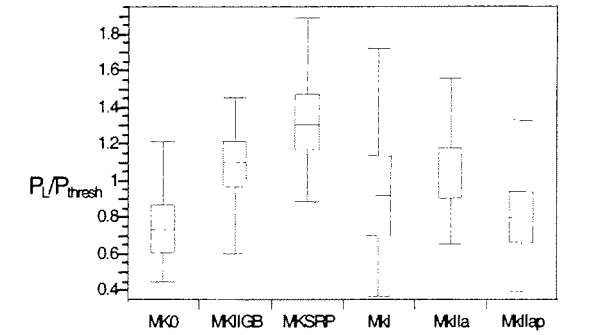

Figure 3: Deviation of the threshold power from the fit for each divertor in JET

The same analysis is done for ASDEX and ASDEX Upgrade and DIV-I gives a smaller threshold. The closed divertor is chosen for Alcator C-Mod and JT-60U, as expected from the fact that closed divertors are more suited to keep the plasma impurity level low. Since closed divertors are chosen and TCV works with an open divertor, TCV is removed from the data set. Table 3 summarises the selected divertor for the tokamaks which changed divertor configuration.

TABLE 3: Selected divertors

Tokamak	Divertor
ASDEX	DIV-I
ASDEX Upgrade	DIV-I
Alcator C-Mod	DIVCLOSE
JET	MkIIap
JT-60U	CLOSEDSN

With this restriction to one divertor per tokamak, the number of data points decreases to 462 and the new fit is:

$$P_{th4} = 2.96\ n_{e20}^{0.85}\ B_T^{0.51}\ a^{1.07}\ R^{0.83} \qquad \text{RMSE=22.9\%} \qquad (4)$$

The RMSE is much smaller with this restricted dataset indicating that the type of divertor plays an important role in the data scattering. Compared to the global fit (3), the dependence in plasma density is, here, stronger and in the magnetic field weaker, while the dependence in plasma size remains similar. In comparison, the fit calculated with the JET

MKII GB (SRP) divertor, which induces a higher threshold power in JET, gives a stronger dependence in a and R, 1.55 and 0.53 respectively. Figure 4 shows the reduction of the scattering in the comparison between experimental and estimated threshold power when only one divertor is selected.

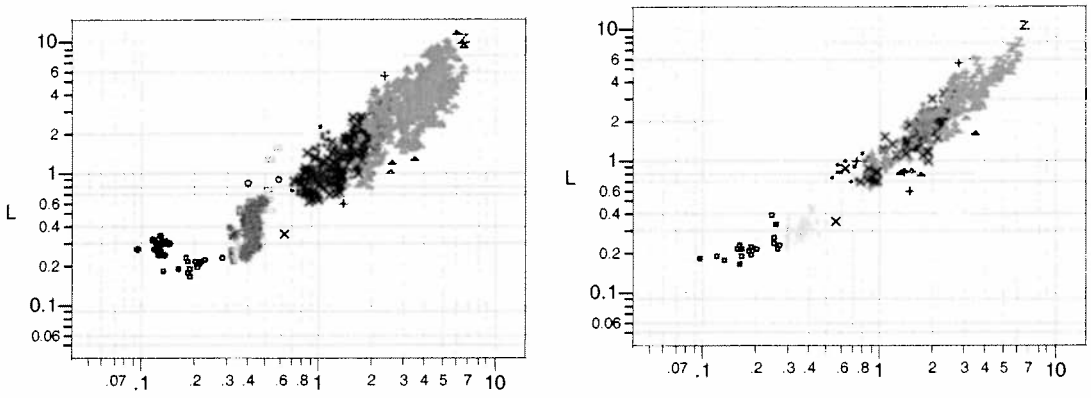

Figure 4: Comparison between the experimental and estimated threshold power for the fits (3) and (4), corresponding to the global dataset and the restricted to one divertor per tokamak dataset.

4.3 Influence of the phase in the transition process

In the previous fit, the selected data have the PHASE variable equals to either D, DH, LD, LDL, LH, OHMD or OHMH. In this subset, ASDEX Upgrade data contain all LDL time slices (22). These time slices show an experimental threshold power much bigger than the estimated power as well as the average power, as shown in Fig.5. This is in contradiction with the fact that these data points could be just at the threshold. Nevertheless, these time slices are removed from the dataset. Similarly, OHMH data are removed for ASDEX Upgrade.

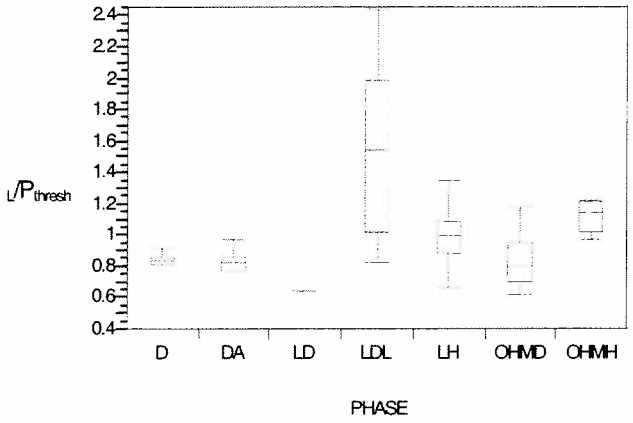

Figure 5: Deviation of the threshold power from the fit for each PHASE in ASDEX Upgrade

The same filtering is applied to all other tokamaks and TCV rejoins the dataset since its data is well aligned with the scaling. This data set contains 461 time slices and the fit is:

$$P_{th5} = 2.34\ n_{e20}^{0.67}\ B_T^{0.62}\ a^{1.02}\ R^{0.71} \qquad \text{RMSE=21.5\%} \qquad (5)$$

The RMSE is lower than in the previous fit. The exponents for a and R are slightly reduced.

In this dataset, each tokamak contributes with a quite different weight: JET has 113 data points while PBX-M has only 5. A random selection is performed to reduce the large datasets (JET and ASDEX Upgrade) to approximately 50 samples to match the population of most of the remaining ones (Alcator C-Mod, DIII-D, JFT-2M, JT-60U and TCV). The dataset is then reduced to 367 entries. The RMSE value is slightly reduced but the coefficients of the fit remain quite similar, independently of which data is kept for ASDEX Upgrade and JET.

4.4 Effect of the parameter set

The new fits presented in this paper so far are based on the plasma density, magnetic field, plasma minor and major radius. Fits are also calculated with the plasma outer surface area instead of a and R. The results are very similar. The effect of the aspect ratio $\varepsilon = a/R$ cannot be determined with this parameter set. Similarly, the plasma shape can play a non-negligible role in the threshold power as seen in TCV [6]. Therefore, an extension of the parameter set could lead to a more precise fit of the threshold power. However, it is necessary to select parameters which are not a combinations of the others, such as the aspect ratio taken with a and R in the fit. Typically the shape and size of a plasma can be defined by 3 independent parameters, for instance: a or R, κ (plasma elongation) or S, ε or $R_{mm}=R_{max}/R_{min}=(R+a)/(R-a)$. The latter parameter also describes the aspect ratio, although differently. Fits using different combinations of these parameters are calculated with the dataset used for (5) enlarged with MAST and NSTX data, since these devices widen significantly the range in aspect ratio or R_{mm}. 412 time slices make up this dataset. The fit using only a and R is compared to the best fit of this family, that found with R, S and R_{mm}:

$$P_{th6} = 3.73\, n_{e20}^{0.55}\, B_T^{0.60}\, a^{1.43}\, R^{0.18} \qquad \text{RMSE=24.5\%} \qquad (6)$$

$$P_{th7} = 0.151\, n_{e20}^{0.63}\, B_T^{0.67}\, R^{1.22}\, S^{0.25}\, R_{mm}^{1.21} \qquad \text{RMSE=22.9\%} \qquad (7)$$

The parameter R_{mm} leads to an RMS error smaller than that obtained with the aspect ratio. Since this parameter is proportional to the ratio of the toroidal magnetic field taken at the high field and low field side of the plasma edge ($B_{T(in)}/B_{T(out)}$), it indicates the importance of the strength of the magnetic field at the plasma edge as already shown in [5].

The LH transition threshold power was found to depend on the X-point height above the divertor floor [7,8]. Including this variable in the parameter set leads to a reduction in the RMS error of the fit, down to 18%. However, this reduction is partly due to a substantial reduction of the dataset since only 203 time slices are used in this calculation. An improvement of the database would therefore be required to address this question.

4.5 Prediction for ITER

Power law scalings presented in this paper are used to estimate the LH threshold power for ITER (R=6.2m; a=2m; S=678m^2; $n_{e20}=0.610^{20}$m^{-3}; B=5.3T) as shown in Table 4. The uncertainty is calculated as the standard error in prediction.

The low value of the prediction with scaling P_{th3} (3) is due to the participation of small devices with a high threshold power in the fit, which induces a tilt in the fit and therefore an under estimation when extrapolating to large devices. In case of scaling P_{th6} (6), the prediction is biased by the presence of the spherical tokamaks in the traditional fit with plasma density, magnetic field, major and minor radii. With the set of parameter used for this scaling, they also induce a similar tilt than in scaling P_{th3}.

TABLE 4: Threshold power for H-mode access in ITER

Scaling	Threshold power [MW]
P_{th1}	46
P_{th2}	40
P_{th3}	32 - 35
P_{th4}	40 - 45
P_{th5}	32 - 37
P_{th6}	27 - 31
P_{th7}	32 - 37

Scalings P_{th5} (5) and P_{th7} (7) are based on a large set of devices and data points. They have a modest RMSE and their residuals are independent of the plasma size. These scalings can therefore be taken as the reference for estimating the threshold power in future devices. Both give the same predicted threshold power for ITER.

5. Conclusions

New data have been added into the International H-mode threshold database which now contains 7673 time slices from 13 tokamaks. The initial dataset is enlarged (1298 time slices), including new data and data taken during the dithering phase.

After selecting data from the best divertor for each device and from the best LH transition times, according to the DIVNAME and PHASE parameter respectively, the RMSE of the fit was lowered down to 22.9%. In this fit most devices are represented, improving the data range and therefore the reliability of the fit.

With the addition of a new parameter in the fit, (R+a)/(R-a), and the use of the major radius and the plasma surface for the plasma geometry description, the Spherical Tokamaks, MAST and NSTX, are well fitted.

The predicted threshold power for ITER reaches 35MW when the best fits are used.

Acknowledgement

This paper could not have been written without the contribution of the teams working on tokamaks providing data to the International H-mode Threshold Database. The authors would like to thank them all.

References

[1] ASDEX Team, Nucl. Fus. 29 (1989) 1959
[2] Burrell K H et al. Plasma Phys. and Contr. Fusion 31 (1989) 1649
[3] Ryter F et al. Nucl. Fus. 36 (1996) 1217
[4] Snipes J A et al. 19th IAEA Fus. Energy Conf. IAEA-CN-94/CT/P-04
[5] Takizuka T et al. Plasma Phys. and Contr. Fusion 46 (2004) A227
[6] Martin Y R et al. Plasma Phys. and Contr. Fusion 44 (2002) A143
[7] Carlstrom T N et al. Proc. of 16th European Conference on Controlled Fusion and Plasma Physics, Vol 13B (1989) 241
[8] Andrew Y et al. Plasma Phys. and Contr. Fusion 46 (2004) A87

FT/1-1Rc

Development of Steady-State 2 MW, 170 GHz Gyrotrons for ITER

B. Piosczyk 1), A. Arnold 1[a]), G. Dammertz 1), R. Heidinger 1), S. Illy 1), J. Jin 1), K. Koppenburg 1), W. Leonhardt 1), G. Neffe 1), T. Rzesnicki 1), M. Schmid 1), M. Thumm 1[a]), X. Yang 1),
S. Alberti 2), R. Chavan 2), D. Fasel 2), T. Goodman 2), M. Henderson 2), J.P. Hogge 2), M.Q. Tran 2), I. Yovchev 2),
V. Erckmann 3), H.P. Laqua 3), G. Michel 3),
G. Gantenbein 4), W. Kasparek 4), G. Müller 4), K. Schwörer 4),
D. Bariou 5), A. Beunas 5), E. Giguet 5), G. LeCloarec 5), F. Legrand 5), C. Liévin 5),
O. Dumbrajs 6)

1) Forschungszentrum Karlsruhe (FZK), Association EURATOM-FZK, Postfach 3640, D-76021 Karlsruhe, Germany, [(a)] also Universität Karlsruhe, D-76128 Karlsruhe, Germany
2) CRPP, Ass. EURATOM-Confédération Suisse, EPFL Ecublens, Lausanne, Suisse
3) MPI für Plasmaphysik, Association EURATOM, D-17491 Greifswald, Germany
4) Institut für Plasmaforschung, Universität Stuttgart, Pfaffenwaldring 31, Stuttgart, Germany
5) Thales Electron Devices, 2 bis, Rue Latécoère, F-78941 Vélizy-Villacoublay, France
6) Helsinki University of Technology, Association EURATOM-TEKES, FIN-02015 HUT, Finland

e-mail contact of main author: bernhard.piosczyk@ihm.fzk.de

Abstract. A prototype of a 1 MW, CW, 140 GHz conventional gyrotron for the W7-X stellarator in Greifswald/Germany has been tested successfully and the fabrication of series tubes started. In extended studies the feasibility for manufacturing a continuously operated high power coaxial cavity gyrotron has been demonstrated and all needed data for an industrial design has been obtained. Based on this results the fabrication of a first prototype of a 2 MW, CW, 170 GHz coaxial cavity gyrotron started recently in cooperation between European research institutions and European tube industry. The prototype tube is foreseen to be tested in 2006 at CRPP Lausanne where a suitable test facility is under construction.

1. Introduction

Gyrotron oscillators have proven to be the most powerful sources of coherent wave radiation in the millimeter wavelength range. Fusion experiments of the next generation such as the stellarator W7-X now under construction at Greifswald/Germany or the international thermonuclear experimental reactor (ITER) require gyrotrons with a microwave (RF) output power of one megawatt or more in continuous wave (CW) operation. At the W7-X stellarator plasma heating with EC waves will be the main heating method. In total an electron cyclotron wave (ECW) system capable to deliver up to 10 MW, CW microwave power at 140 GHz (10 gyrotrons a 1 MW) will be built up to meet the goals of this stellarator with inherent steady-state capability [1]. For ITER 24 MW, CW microwave power at 170 GHz is foreseen in the basic scenario for heating and for stabilization of NTM instabilities [2]. The development of such gyrotrons in the frequency range between 110-170 GHz is subject of investigation worldwide since a number of years. A great progress has been made in the development of conventional long pulse gyrotrons with 1 MW microwave output power during the last years [3-6]. For the development of the 140 GHz gyrotrons a European gyrotron collaboration has been established between European research laboratories (mainly FZK Karlsruhe and CRPP Lausanne) and European tube industry (Thales Electron Devices, (TED), France). The results obtained within this collaboration are very convincing. With a prototype of the 140 GHz gyrotron the capability of CW operation around 1 MW microwave output power has been

practically demonstrated. The obtained results have lead to the decision to start with the series production of seven gyrotrons of this type as needed at the W7-X stellarator .
To reduce the costs of the installations of the ECW system at ITER and to allow a compact upper port launcher an increase of the output power per gyrotron is desirable. Coaxial cavity gyrotrons have the potential to generate microwave power in excess of 1 MW, CW at frequencies around 170 GHz since very high-order volume modes can be used. This is because the presence of the coaxial insert practically eliminates the restrictions of voltage depression and limiting current and in addition, the problem of mode competition is reduced by a selective influence of the diffractive quality factor of competing modes [7]. The feasibility of manufacturing a 2 MW coaxial gyrotron operated in CW has been demonstrated and data needed for an industrial design has been obtained [8,9]. The suitability of the major gyrotron components for CW operation has been examined and according to a first draft integral design no technical constraints have been found for manufacturing of a 2 MW, CW coaxial gyrotron as could be used for ITER. Based on these results the manufacturing phase of a first prototype of such a coaxial cavity gyrotron at 170 GHz started recently within the above mentioned European gyrotron collaboration. The technical design including integration of all components as well as thermo-mechanical calculations and specifications of auxiliary systems needed for operation of the tube is in progress. The delivery of the first prototype is expected for beginning of 2006. The SC magnet has been specified and has been already ordered. A test facility for testing the 2 MW tube up to CW is under construction at CRPP Lausanne [10].
In the following, first the main results and the status of the 1 MW, CW, 140 GHz conventional gyrotron for W7-X will be given and then the work on the 2 MW, CW, 170 GHz coaxial cavity gyrotron will be described.

2. 140 GHz gyrotron for W7-X

The development of the 1 MW, CW, 140 GHz gyrotron for the W7-X stellarator in Greifswald/Germany started a few years ago within the above mentioned European gyrotron collaboration. The $TE_{28,8}$ mode has been selected as operating cavity mode. The gyrotron has been equipped with a highly efficient internal quasi-optical mode converter, a single-stage depressed collector and an edge-cooled, single-disk CVD-diamond window. The main design parameters are summarized in Tab. I.

TABLE I: Main design parameters of the 140 GHz gyrotrons for W7-X.

operating cavity mode	$TE_{28,8}$
RF output power, P_{out} / MW	1
accelerating voltage, U_{acc} / kV	81
beam current, I_b / A	40
RF output efficiency, η_{out}	≥ 45%

A pre-prototype (maquette) and a prototype tube have been built and tested at FZK till now. In Fig. 1 both the bare gyrotron and the tube installed in the superconducting (SC) magnet for testing are shown. With the prototype tube the design specifications have been almost fulfilled. A maximum RF output power of 970 kW with an output efficiency of ~44% has been achieved for a pulse length of 11.7 s. For 180 s an output power of 890 kW has been obtained. The 180 s pulse was limited due to the capability of the high voltage (HV) power supply available at FZK.
At a beam current reduced to about 25A, at which the HV power supply allows an operation

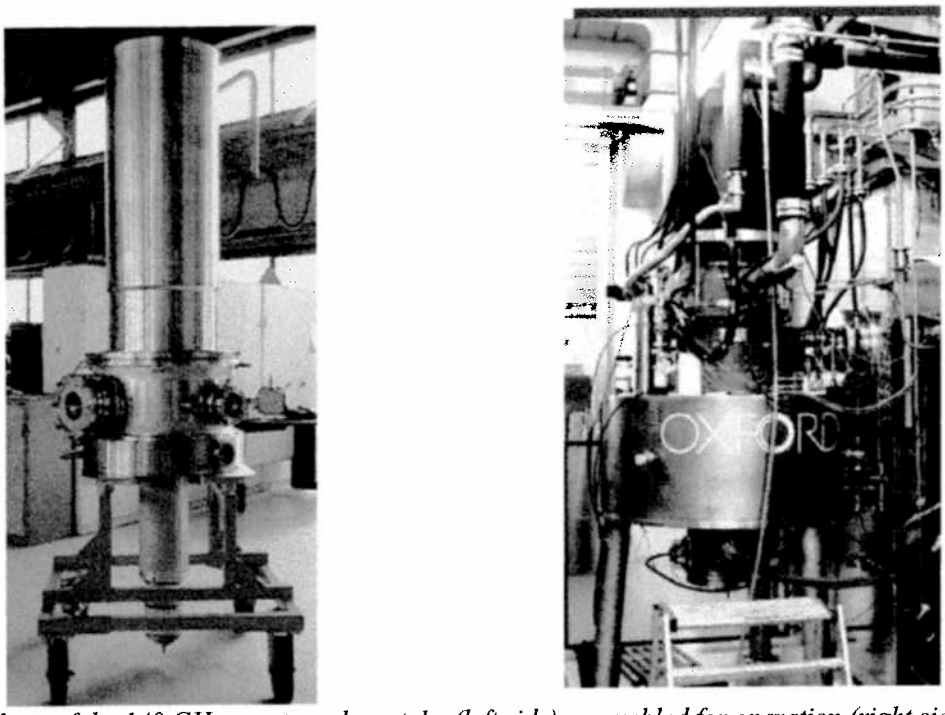

Fig. 1.: Photo of the 140 GHz gyrotron, bare tube (left side), assembled for operation (right side).

up to CW, an output power of 540 kW with an efficiency of 41% has been obtained with the prototype tube for a pulse length of 937 s limited by a pressure increase inside the gyrotron [6]. At further reduced beam current with an output power of ~250 kW the pulse length was extended up to 1300 s. In Fig. 2 the results are summarized. The mode purity of the Gaussian output beam is as high as 98 %. The pressure increase is assumed to be caused due to warming up of internal parts of the ion getter pumps, placed inside the mirror box, to temperatures above 250^{0}C by the microwave stray losses inside the tube. The microwave stray losses have been measured to be as low as 3.2% of the output power in good agreement with the calculated value of 2.1 %. The internally absorbed part of the stray radiation was experimentally determined to only 1.4 %. Even this low value caused an increase of the temperature of the internal ion getter pumps as has been clearly shown by temperature measurements with an infrared camera. In order to avoid the pressure rise due to the warming up of the pumps in the series gyrotrons the ion getter pumps will be placed outside the mirror box.

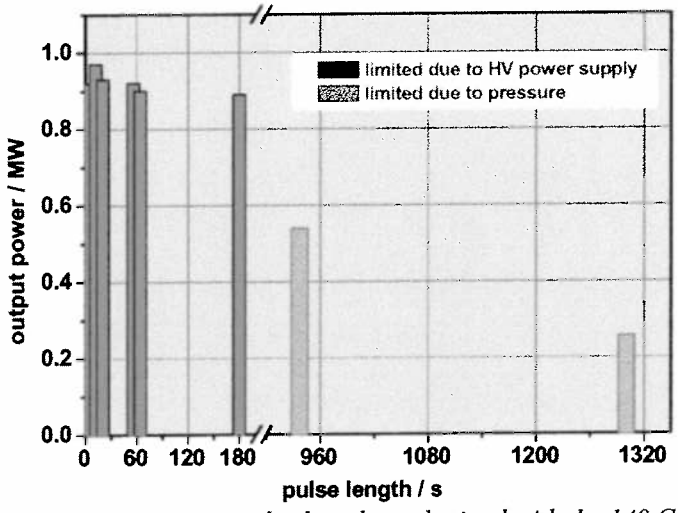

Fig. 2: Maximum RF output power versus pulse length as obtained with the 140 GHz prototype tube.

The design output power of 1 MW was not fully achieved. This is suspected to be due to azimuthally inhomogeneous electron emission of the emitter ring which may result in a degradation of the electron beam quality and, as a consequence, in a limitation of the microwave output power to values slightly below 1 MW. For the seven series gyrotrons under production special attention will be paid to the quality assurance of the emitter rings.

3. 2 MW, CW, 170 GHz coaxial cavity gyrotron for ITER

The feasibility of manufacturing a 2 MW coaxial gyrotron operated in CW has been studied experimentally and theoretically during the last years at FZK. The investigations have been performed on a coaxial gyrotron operated at 165 GHz in the $TE_{31,17}$ mode described in detail in [8]. This experimental gyrotron is demountable and enables an easy replacement of the components. Its cooling performance allows an operation only at short pulses (typically ≤ 10 ms). With this gyrotron problems specific to the coaxial arrangement as mechanical stability of the coaxial insert, required alignment accuracy, leakage current to the insert and losses have been studied. A limitation of the HV performance due to build up of a Penning discharge inside the coaxial electron gun has been successfully suppressed by modifying the gun geometry such that electron trapping is avoided. A maximum RF output power P_{out} of 2.2 MW has been obtained in single-mode operation and efficient microwave generation has been demonstrated. The conversion of the high-order cavity mode into a free space Gaussian mode has been performed in a quasi-optical (q.o.) RF output system consisting of a smooth launcher with a cut and of two mirrors. The microwave stray losses captured inside the tube body have been investigated and the amount of the losses has been measured. The feasibility of the main gyrotron components for use in CW operation has been examined and demonstrated. According to a first draft integral design of a 2 MW, CW coaxial gyrotron no technical constraints have been found [9].

Based on these results it has been decided to begin within the European gyrotron collaboration the development of a coaxial cavity gyrotron with an RF output power of 2 MW, CW at 170 GHz as could be used in the ECW system of ITER. The conceptual design of such a tube compatible with CW operation has been completed and the manufacturing phase of a first prototype started recently. The first prototype is expected to be delivered beginning of 2006. A superconducting (SC) magnet has been specified and already ordered. A test facility designed to host the 2 MW, CW gyrotron and to perform experimental investigations up to full performances is presently built up at CRPP Lausanne.

TABLE II: Design parameters of the prototype and pre-prototype of the coaxial gyrotron.

	prototype	**pre-prototype**
operating cavity mode	$TE_{34,19}$	
frequency, f / GHz	170	
RF output power, P_{out} / MW	2	~ 1.5 - 1.7
beam current, I_b / A	75	
accelerating voltage, U_{acc} / kV	90	~80
pulse length: τ	up to CW	5 - 10 ms
efficiency (with depressed collector), η_{out}	$\geq$ 45 %	
cavity magnetic field, B_{cav} / T	6.87	6.66 - 6.70
velocity ratio, $\alpha = \beta_\perp / \beta_\parallel$	1.3	

In parallel to the work on the industrial tube, the design of the most critical components of the prototype - as electron gun, cavity and RF interaction and the quasi-optical RF output system - will be verified under realistic conditions. For this the experimental 165 GHz coaxial gyrotron at FZK has been modified for operation at 170 GHz in the $TE_{34,19}$ cavity mode. This

tube is considered as a pre-prototype for the 2 MW, CW industrial gyrotron since it is equipped with a cavity and a q.o. RF output system same as designed for the prototype and with an electron gun which is very similar to the gun of the prototype. The nominal design parameters of both tubes, the 2 MW, CW prototype and the short pulse pre-prototype are summarized in Table II. The reduction of the beam voltage to about 80 kV for operation of the pre-prototype became necessary because the maximum magnetic field of the available SC-magnet at FZK is limited to values between 6.66 and 6.70 T. Therefore, in order to be able to excite the $TE_{34,19}$ mode at 170 GHz at the reduced magnetic field, the beam voltage has to be reduced. Consequently somewhat reduced RF output power is expected in the pre-prototype tube.

3.1. First prototype of the 2 MW, 170 GHz coaxial cavity gyrotron

The physical design of main components of the 2 MW prototype tube have already been done and the detailed drawings for manufacturing are in progress. In order to keep the wall loading inside the cavity within technically acceptable limits, the $TE_{34,19}$ mode has been selected as operating mode. The geometry of the cavity is shown in Fig. 3. The coaxial insert is tapered and corrugated as indicated in that figure. This allows a selective influence of the quality factor of neighbouring modes reducing thus the mode competition [7]. The Ohmic losses at the outer cavity wall have been calculated to be within 1 kW/cm² (ideal copper at 273 K) for a generated RF power of 2.2 MW. The corresponding peak losses at the insert have been calculated to be less than 0.1 kW/cm². The start up behaviour has been simulated with a time dependent, self consistent multimode code considering up to 13 competing modes. High efficient, single mode operation is expected over a wide parameter range. The main mode competition occurs between the two mode triplets, $\{TE_{-33,19}, TE_{-34,19}, TE_{-35,19}\}$ and $\{TE_{+32,20}, TE_{+33,20}, TE_{+34,20}\}$. Simulations have also been performed for a cavity with walls slightly deformed due to the Ohmic heat loading.

A new RF output system with a dimpled-wall launcher and three mirrors - a quasi-elliptical mirror followed by a toroidal and a phase correcting mirror with a non-quadratic surface - has been designed [11] in order to keep the microwave losses inside the gyrotron tube within technically acceptable limits (≤ ~5% of RF output power). From the use of a dimpled-wall launcher a reduction of diffraction losses at the edge of the launcher cut is expected. The goal for designing the mirrors was to generate an RF output beam with a high Gaussian content. However, because of limitations in the accuracy of mechanical fabrication of the surface structure of the non-quadratic mirror a compromise has been made between the Gaussian content of the RF output beam and the amount of microwave losses inside the tube.

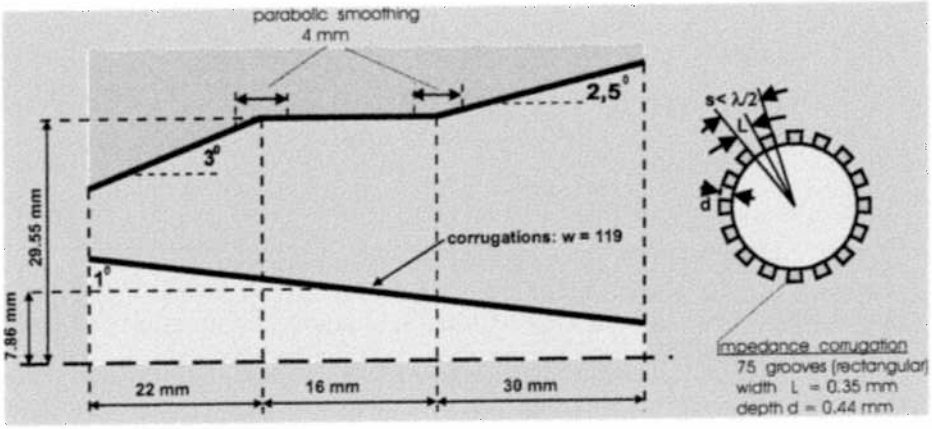

Fig. 3: Cross section of the $TE_{34,19}$ coaxial cavity

According to calculations the total amount of microwave stray losses inside the gyrotron tube is expected to be within the technically acceptable value (~ 5 % to 6 % of P_{out}). The short-pulse experiment will allow to verify the design performance, to measure the amount of stray losses and to study experimentally possibilities to absorb the microwave losses inside the tube.

A coaxial magnetron injection gun (CMIG) has been designed similar to the gun used in the 165 GHz gyrotron [12]. The emitting current density is about 4.2 A/cm^2 at I_b = 75 A. The inner part of the coaxial insert is cooled with water and its position can be adjusted under operating conditions. Special care has been taken in designing the geometry of the cathode and the insert in order to avoid regions in which electrons can be trapped in order to avoid the built up of a Penning discharge.

As RF output window a single-disk of CVD diamond with a thickness of 1.852 mm = 5λ/2 at 170 GHz will be used. At a loss tangent of 2×10^{-5} (state of the art) 880 W power will be absorbed in the disk [13]. Edge cooling of the CVD diamond disk with water is sufficient for removing the heat load. The window will have an aperture of 96 mm.

To obtain a desired total efficiency of ≥ 45 % a single-stage depressed collector with the collector at ground potential will be used. Under nominal operating conditions the remaining beam power which has to be dissipated in the collector is expected to be about 2.3 MW, CW. In case of fast modulation of the microwave output power as required for NTM stabilisation at ITER the average beam power which has to be dissipated power at the collector walls increases up to ~3 MW. The design optimisation of the collector is in progress.

The magnetic field distribution and the technical parameters of the SC-magnet have been specified and the SC-magnet has been already ordered. In addition to the solenoidal coils the magnet will be equipped with a set of dipole coils generating a transverse magnetic field needed for the alignment of the coaxial insert relative to the electron beam under operating conditions. The warm bore-hole will have a diameter of 220 mm and the distance between the cathode position and the maximum of the magnetic field will be about 380 mm.

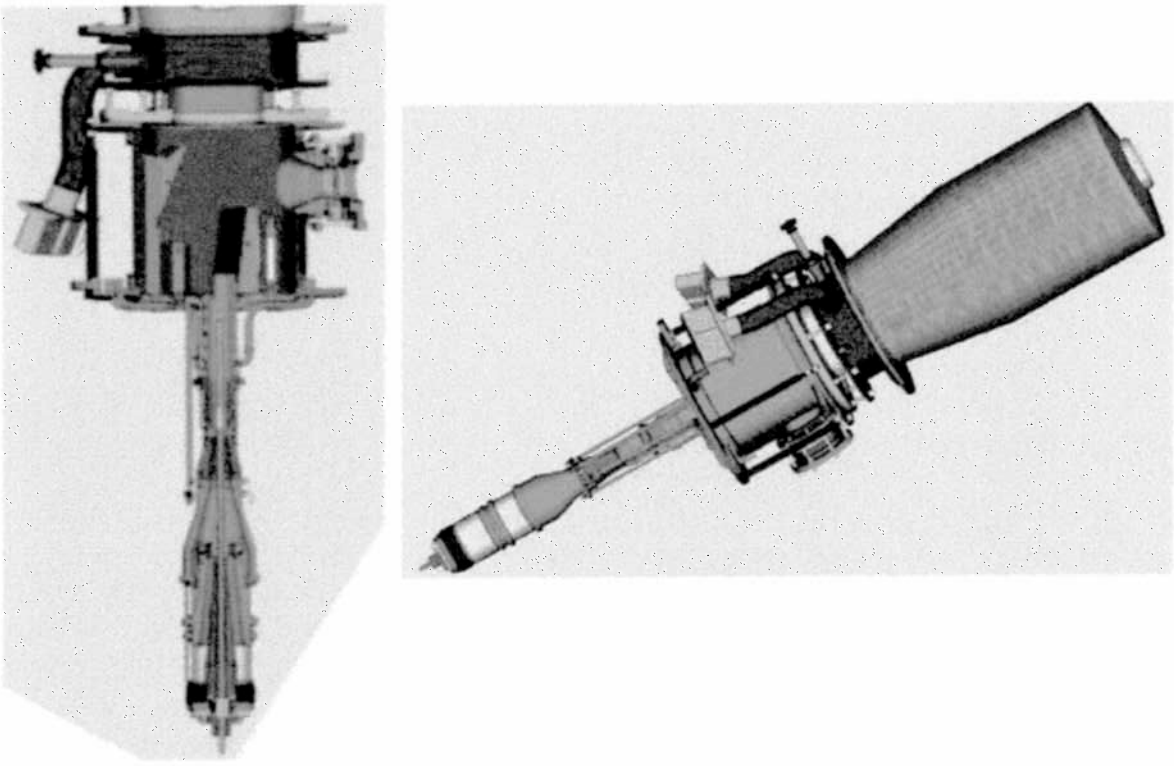

Fig. 4: View of the integrated coaxial gyrotron, cut (left side) and full tube (right side)

An integral design of a 2 MW, CW coaxial gyrotron has been performed as shown in Fig.4. The high voltage insulation between the body and the collector is placed at the top of the mirror box. The overall dimensions of the gyrotron are comparable with the dimensions of a conventional 1 MW, CW, 140 GHz gyrotron.

3.2. The pre-prototype of the 2 MW, 170 GHz coaxial cavity gyrotron

In order to verify the design of the most critical components of the prototype the experimental short pulse coaxial gyrotron at FZK operated at 165 GHz in the $TE_{31,17}$ mode has been modified for operation at 170 GHz in the $TE_{34,19}$ cavity mode. This modified coaxial gyrotron is equipped with an electron gun which is very similar to the gun of the industrial prototype and both the cavity and the quasi-optical RF output system will have the same geometry as in the prototype tube. Thus the generation of the high power electron beam, RF interaction and mode competition as well as the design of the RF output system will be verified and the amount of stray radiation will be measured under realistic conditions. The main nominal design parameters are summarized in Tab. II, both for the 2 MW, CW prototype and for the short pulse tube. The SC-magnet used for the short pulse experiments delivers only a magnetic field up to about 6.68 T. Due to this the beam voltage has to be reduced to values below 80 kV in order to be able to excite the $TE_{34,19}$ mode at 170 GHz. The operation at a lower voltage results in an RF output power reduced to a value of about 1.5 MW depending on the finally obtained magnetic field.

The modifications of the previously used 165 GHz coaxial gyrotron for operation at 170 GHz have already been performed. All components have been fabricated, the pre-prototype has been assembled and installed inside the SC-magnet. A schematic view of the coaxial magnetron injection gun (CMIG) is shown in Fig. 5. The emitting current density is about 4.2 A/cm^2 at $I_b = 75$ A. The inner part of the coaxial insert is cooled with water as needed for CW operation and its position can be adjusted under operating conditions. Regions inside the gun in which electrons can be trapped have been avoided. The pulse length is limited to 5 - 10 ms depending on the beam current. The limitation in pulse length is due to the fact that the cavity, the launcher and the mirrors are not actively cooled and no beam sweeping along the collector surface is foreseen. A disk out of fused silica with a thickness of 6.84 mm $\cong 15\lambda/2$ at 170 GHz is used as RF output window.

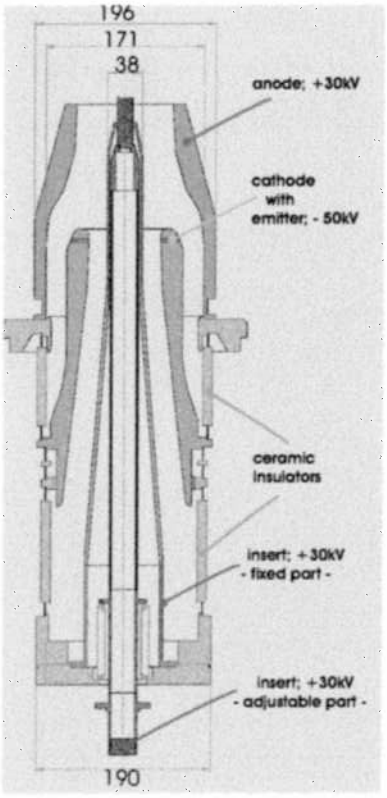

Fig. 5: CMIG gun (dimensions in mm)

The experimental operation started recently. First, the radial position of the inner conductor has been aligned with respect to the electron beam within ± 0.1 mm. Stable operation up to $I_b \approx 58$ A (present limit of the HV power supply) and $U_c \approx 80$ kV has been achieved without any instabilities and parasitic low frequency oscillations. No indications of the built-up of a Penning discharge inside the gun have been observed. The oscillation of the nominal $TE_{34,19}$ mode has been observed in a parameter range which is in good agreement with theoretical predictions. Work on optimization of the microwave output power and efficiency is underway. The distribution of the

microwave output beam has been found to be not in agreement with the calculations. The reason is not clear yet and a detailed analysis is in progress. The experimental measurements are continuing.

3. Summary and outlook

The development of the 1 MW, CW 140 GHz conventional (hollow waveguide) cavity gyrotron for W7-X was very successful. CW operation at 1 MW output power has almost been obtained and thus the series production of seven additional tubes has started. Encouraged by this impressive progress and based on results of short pulse experiments the development of a 2 MW, CW 170 GHz coaxial cavity gyrotron as could be used for ITER is in progress within the European gyrotron collaboration. The manufacturing phase of a first 2 MW, CW prototype started recently. Delivery of the prototype tube is expected for beginning of 2006. A suitable test facility is under construction at CRPP Lausanne. In parallel to the work on the prototype tube experimental operation with a short pulse pre-prototype tube is in progress in order to verify the design of critical components of the prototype tube.

References

[1] V. Erckmann, et al., "ECRH and ECCD with high power gyrotrons at the stellarators W7-AS and W7-X", IEEE Trans. Plasma Sci., PS-27, pp. 538-546, 1999.

[2] ITER Physics Basis Editors et al.," ITER Physics Basis", Nucl. Fusion, vol. 39, pp. 2137-2638, 1999.

[3] V. E. Zapevalov, et al., "Development of a 170 GHz/1 MW Russian gyrotron for ITER", Fus. Eng. Design 53 (2001), pp. 377-385

[4] A. Kasugai, et al., "1 MW and long pulse operation of Gaussian beam output gyrotron with CVD diamond window for fusion devices", Fusion Eng. Design 53 (2001) 399-406

[5] M. Blank, et al., "Demonstration of High-Power, Long-Pulse, 140 GHz Gyrotron Oscillator", IEEE Trans. Plasma Science, Vol. 32, No. 3, June 2004, 867-876.

[6] G. Dammertz, et al., "Development of a 140-GHz, 1-MW Continuous Wave Gyrotron for the W7-X Stellarator", IEEE Trans Plasma Sci., vol. 30, June 2002, 808-818.

[7] C.T. Iatrou, S. Kern, A. Pavelyev "Coaxial cavities with corrugated inner conductor for gyrotrons", IEEE Microwave Theory Tech. vol. 41, No. 1, January 1996, 56-64.

[8] B. Piosczyk et al., "165 GHz Coaxial Cavity Gyrotron - last results", IEEE Trans. Plasma Science, Vol. 32, No. 3, June 2004, 853-860.

[9] B. Piosczyk et al., "A 2 MW, 170 GHz Coaxial Cavity Gyrotron", IEEE Trans. Plasma Science, Vol. 32, No. 3, June 2004, 413-417.

[10] J.P. Hogge et al. "Development of a 2 MW, CW, 170 GHz Coaxial Cavity Gyrotron for ITER", EC13, May 17-20, 2004, Nizhny Novgorod, Russia.

[11] G. Michel, "Synthesis of Yeti-footprint-mirrors with low stray radiation", EC 13, May 17-20, 2004, Nizhny Novgorod, Russia

[12] B. Piosczyk, "A novel 4.5 MW electron gun for a coaxial gyrotron", IEEE Trans. Electron Devices, vol. 48, No.12, December 2001, 2938-2944.

[13] R. Heidinger, et al., "CVD diamond windows studied with low and high power waves", IEEE Trans Plasma Sci., vol. 30,. June 2002, 800-807.

Experimental Studies of Alfvén Mode Stability in the JET Tokamak

D.Testa[1], A.Fasoli[1,2], R.Bertizzolo[1], D.Borba[3], R.Chavan[1], S.Huntley[4], V.Riccardo[4], S.Sanders[4], J.A.Snipes[2], P.Titus[2], R.Walton[4], M.Way[4], JET-EFDA contributors*

[1] CRPP, Association EURATOM – Confédération Suisse, EPFL, Lausanne, Switzerland
[2] Plasma Science and Fusion Center, Massachusetts Institute of Technology, Boston, USA
[3] Associacão EURATOM/IST, Av. Rovisco Pais, 1049-001 Lisboa, Portugal
[4] EURATOM-UKAEA Fusion Association, Culham Science Centre, OX14 3DB, Abingdon
E-mail of main author: duccio.testa@epfl.ch)

1. Introduction

Controlling the interaction between fusion generated α's and modes in the Alfvén frequency range is a crucial issue for the operation of experimental reactors in the burning plasma regime, such as ITER, as these modes can be driven unstable by the slowing-down α's up to amplitudes at which they could cause rapid radial transport of the α's themselves. The need to avoid strongly unstable regimes for some classes of Alfvén Eigenmodes (AEs) could therefore provide additional operational limits for the reactor regime. On the other hand, if adequate actuators are identified, AEs could be used to affect the thermonuclear plasma burn in a controlled way.

Two classes of investigations are conducted on JET to directly observe the AE stability limits in the presence of fast particles that can resonate with the modes and to measure the damping rate of the modes as a function of the plasma parameters, in order to quantify the mechanisms that provide background damping for the modes in different conditions. Sections 2 and 3 describe experiments from the first class, addressing the AE stability threshold for different fast ion radial distributions, generated at different locations by additional heating or at different plasma densities, or modified by the presence of error field mode. Examples from the second class are described in Section 4. During the last two years a particular effort was undertaken to complete the database of damping rate measurements of low toroidal mode numbers using the saddle coil active AE excitation system, which is being dismantled during the 2004 JET shutdown. A new antenna system is under development to continue along the same lines, but extending the accessible range of toroidal mode numbers to higher values, up to $n \approx 10\text{-}15$, of more direct relevance to ITER. This system is described in Section 5.

2. Effect of the ICRF heating scheme and of plasma density on the AE stability threshold

Different Ion Cyclotron Resonance Frequency (ICRF) heating schemes are used to create different distributions of energetic particles, with energies in the MeV range, and test their stability with respect to AEs. As a first example, a simple method to affect the radial distribution of fast ions is to change the difference in frequency between independent ICRF modules. A broad fast ion pressure profile can be produced by operating the four JET ICRF antennas at four different frequencies. A wider ICRF power deposition profile corresponds to a lower fast ion pressure gradient, $\nabla\beta_{FAST}$, in the plasma core, thus leading to a reduced mode activity in the Alfvén frequency range [1].

Here we assess the difference on the fast ion distribution function $f_{FAST}(E,r)$ and the perpendicular temperature $T_{\perp FAST}(r)$ between single-frequency (monochromatic) and multi-frequency (polychromatic) minority hydrogen H(D) ICRF heating for similar background plasma parameters, and the effects of such differences on the spectra of fast ion driven AE instabilities. Multi-frequency ICRF heating gives rise to a lower $T_{\perp FAST}$ in the plasma core, as

* See annex 1 of J.Pamela et al., *"Overview of Recent JET Results"*, OV-1/1.4, Fusion energy 2002 (Proc. 19th International Conference, Lyon, 2002) IAEA, Nuclear Fusion 43 (2003), 1540.

measured with a high energy NPA [2]. Earlier measurements of $f_{FAST}(E,r)$ have also shown that, for the same level of P_{ICRF}, polychromatic heating gives rise to a broader $T_{FAST}(r)$, to a more peaked electron temperature profile $T_e(r)$, and to an increase in the central ion temperature T_{i0}, or to the same T_{i0} for a much higher central electron density n_{e0} [3]. This may have favourable implications for ITER operation since the lower $T_{\perp FAST}$ approaches the critical temperature at which fast ions preferentially heat the fuel ions through collisions, but the reduced collisional heating on the electrons, reducing the electron temperature, may in turn adversely affect the current drive efficiency.

To confirm these initial results in a more systematic way, we have compared discharges with the same P_{ICRF} and very similar electron density profiles. For the case of polychromatic heating we observe high-n Toroidal AEs located at the q=2 surface and high-n Ellipticity-induced AEs located at the q=3 surface, closer to the plasma edge. Conversely, for the case of monochromatic heating we only observe q=2 TAEs with significantly higher amplitude, but no EAEs. The presence/absence of the q=3 EAEs and the lower amplitude of the q=2 TAEs confirms that $f_{FAST}(E,r)$ has a broader radial profile, less peaked on-axis, for polychromatic than for monochromatic heating. This suggests a more extensive use of the polychromatic heating scheme in JET for further scenario improvements, also in view of ITER operation.

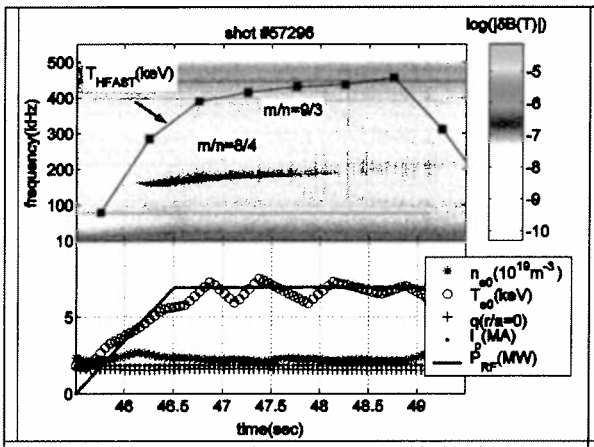

Figure 1a. Mode activity in the Alfvén frequency range for the case of polychromatic ICRF heating. Here only weak TAEs and EAEs are observed.

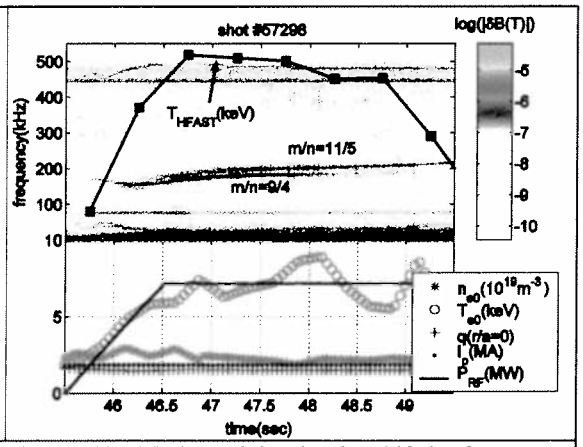

Figure 1b. Mode activity in the Alfvén frequency range for the case of monochromatic ICRF heating. Here strong core localised TAEs are observed.

Operation at high density is beneficial for the burning plasma regimes in ITER. The DT fusion cross section has a broad peak around $E_D \approx E_T \approx 70$keV/amu, and the temperature of the bulk plasma ions has to reach comparable values in order to maximise the fusion yield. The use of 2nd harmonic minority ICRF heating at higher plasma density reduces $T_{\perp FAST}$ in the plasma core due to the lower energy at which the RF diffusion coefficient goes to zero [4], but gives rise to a lower fast ion driven plasma rotation [1]. The reduced rotation may in turn negatively affect the stability of current and pressure driven modes, and limit the possibilities to control turbulence and the transition to high confinement regimes through sheared flow generation [5]. In view of possible extrapolations of the minority ICRF heating schemes used in JET to the heating of the fuel ions in ITER, it is then important to study the stability of fast ion driven AEs as a function of the plasma density for otherwise similar plasma conditions.

First, the most obvious effect of plasma density on ICRF-driven fast ions comes from the dependency of the fast ion slowing down time, $\tau_S \sim T_e^{3/2}/n_e$. Second, the RF diffusion coefficient goes to zero at lower fast ion energy for increasing plasma density due to the larger perpendicular wave number of the ICRF wave field, effectively preventing a formation of a tail in $f_{FAST}(E)$ above a certain energy. This critical energy decreases with the harmonic number, from >3Mev for 1st harmonic heating to ≤1MeV for 2nd and higher order harmonic.

To test this theoretical result and benchmark ICRF code calculations, a series of experiments were performed using the 2nd harmonic H(D) ICRF heating scheme. The ICRF power, P_{ICRF}=5.2MW, the electron temperature profile and the shape of the electron density profile were the same for the various discharges, thus allowing for a direct comparison of T_{FAST} as function of the electron density in the plasma core n_{e0}. The measured $T_{\perp FAST}$ is almost double at low plasma density, $T_{\perp FAST}\approx$200keV at $n_{e0}\approx3\times10^{19}m^{-3}$ compared to $T_{\perp FAST}\approx$120keV at $n_{e0}\approx4\times10^{19}m^{-3}$. Correspondingly, much weaker q=2 TAEs are excited for similar values of P_{ICRF}, thus indicating a much lower drive at the mode radial location, as shown in fig.2. These results are in quantitative agreement with current modelling of the various ICRF heating schemes [4], with encouraging prospects for predictions of ICRF scenarios in ITER.

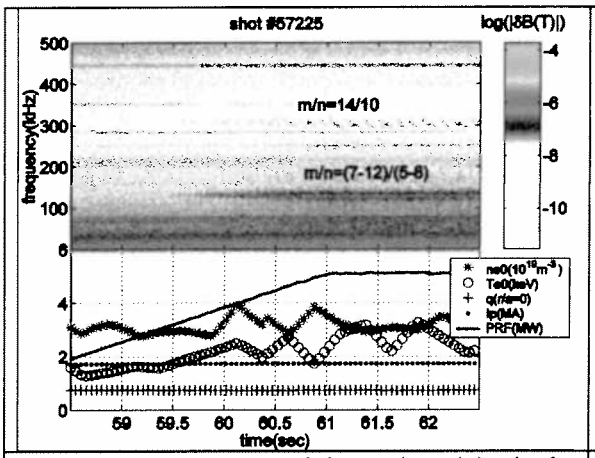

Figure 2a. Measurement of the mode activity in the Alfvén frequency range for the case of lower plasma density, $n_{e0}\approx3\times10^{19}m^{-3}$, thus higher $T_{\perp FAST}\approx$200keV.

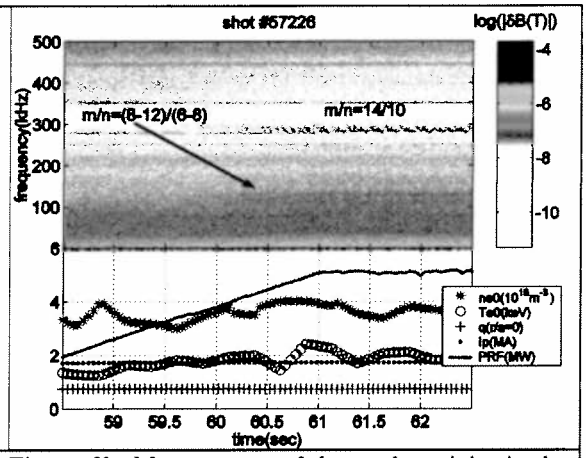

Figure 2b. Measurement of the mode activity in the Alfvén frequency range for the case of higher plasma density, $n_{e0}\approx4\times10^{19}m^{-3}$, thus lower $T_{\perp FAST}\approx$120keV.

3. Effect of error fields on the stability threshold of ICRH driven AEs

The AE stability can be affected by the onset of other instabilities that modify the AE drive by causing a redistribution of the fast ions. Two examples, already described in [6], are the rapid density perturbation associated with pellet injection and the appearance of a q=1 magnetic island associated with a sawtooth crash. To further these earlier studies, we investigated the effect on the fast particle population, hence the AE drive, of externally induced error fields locking to the q=2 surface and generating a magnetic island. The interest for this kind of experiment stems from the fact that an ad-hoc radial redistribution of the fast ions could in principle be beneficial in locally reducing $\nabla\beta_{FAST}$, hence the drive for AEs or Energetic Particle Modes.

In the absence of radially resolved measurements of $f_{FAST}(E,r,t)$, the onset and the disappearance of AEs localised at different radial positions can be used to provide evidence for fast ion redistribution. In these experiments, the in-vessel saddle coils were used in their low-frequency mode of operation to apply an externally controlled error field around the q=2 surface. With and without such error field, we observe EAEs associated with the q=3 surface, whereas with the error fields we do not observe q=2 TAEs, as we do without the error fields. This indicates that the net drive for these modes has been lowered by the error fields and the induced magnetic island around the q=2 surface, with a much weaker effect around the q=3 surface [1].

Similarly, without the error fields, n=4 TAEs become unstable at $P_{ICRF}\approx$3MW, and during the ICRF flat-top phase reach the amplitude at the plasma edge $|\delta B|_{TAE}\approx1.3\times10^{-5}$T. The only difference observed for the n=4 EAE when the error fields are applied is the much higher excitation threshold, $P_{ICRF}\approx$1.1MW without error fields compared to $P_{ICRF}\approx$2MW with error

fields, thus indicating that a larger drive is required in this case. The slightly different central electron temperature, T_{e0}<3keV without error fields compared to T_{e0}~4keV with error fields, does not affect significantly the TAE stability but gives a further indication that the fast ion temperature is larger in the plasma core without error field modes. These observations can be interpreted by considering that the presence of a magnetic island causes a radial redistribution of the fast ions. The detailed modelling of these experimental results is left for future work.

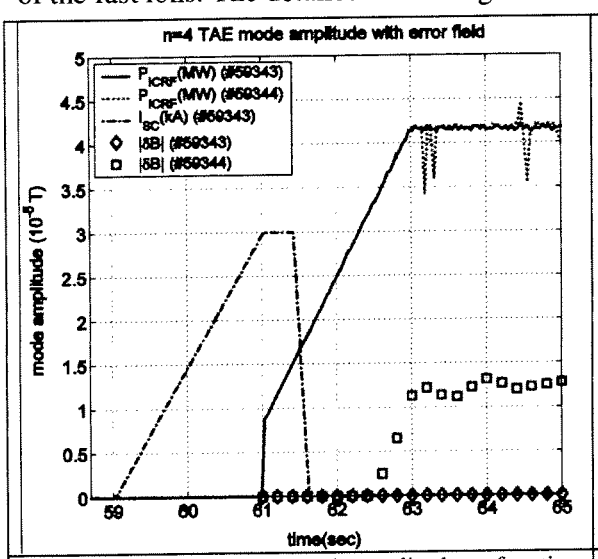

Figure 3a. The n=4 TAE mode amplitude as function of P_{ICRF}. No mode is observed with error fields, and it becomes unstable at P_{ICRF}≈3MW without error fields.

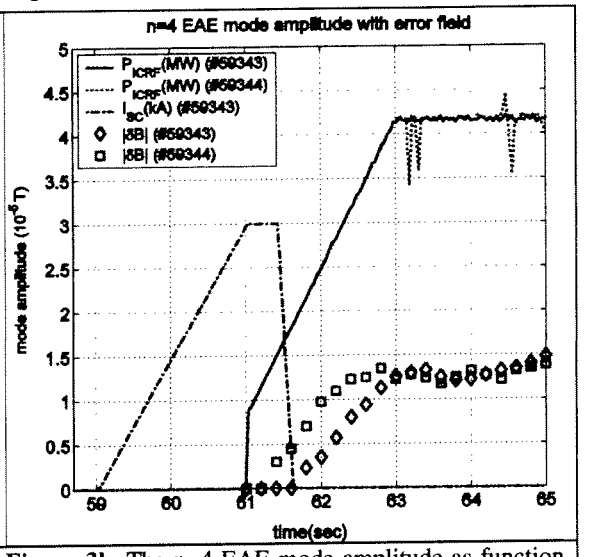

Figure 3b. The n=4 EAE mode amplitude as function of P_{ICRF}. The P_{ICRF} excitation threshold is higher with, P_{ICRF}≈2MW, that without error fields, P_{ICRF}≈1.1MW.

4. Effect of the value of the safety factor on axis, of the plasma rotation and its shear, and of the direction of the ion ∇B-drift on the damping rate for n=1 TAEs

One of the main purposes of the AEs studies on JET is to validate the existing theoretical models and identify the dominant damping mechanisms for global AEs, with the aim to improve the accuracy in the predictions for future burning plasma experiments such as ITER. This approach has characterised the AE active excitation experiments in JET over the last ten years, using the saddle coils as an AE active antenna. The last campaigns aimed at completing the saddle coil database before their removal, in the second half of 2004.

Along this line, we have investigated the role of the central safety factor q_0, of the plasma rotation and of the direction of the ion ∇B-drift on the AE stability in plasmas with a monotonic q-profile. Due to the strong increase of the damping rate for the saddle coil driven, low-n AEs at high edge elongation (κ_{95}>1.6) and triangularity (δ_{95}>0.35) [7], which makes it difficult to measure low-n AEs in such configurations, our experimental work has mainly focused on plasmas with low κ_{95} and δ_{95}, so as to infer in detail the contribution of additional damping mechanisms in regimes much closer to the marginal stability limit of low-n AEs.

Theoretical modelling and direct measurements indicate that low-n AEs have a global structure, i.e., have a radial profile extending over a large fraction of the plasma cross-section. The rotation f_{ROT} of the whole plasma column, and the shear in it $(r/f_{ROT})(df_{ROT}/dr)$, can thus be expected to have an impact over the effective mode damping. Comparing discharges with similar level of Neutral Beam power (P_{NBI}), we notice that for P_{NBI}≤5MW the shear in the plasma rotation has no clear effect on the damping rate of n=1 TAEs. Only for P_{NBI}>6.5MW a general trend can be identified in the database we collected, namely that the damping rate for n=1 TAEs is always γ/ω>2% in discharges characterised by a higher rotation shear, as shown in figs.4a and 4b. This suggests that the damping mechanisms active at low performance are

different from those active at high performance, with the former not affected by the toroidal rotation profile of the plasma column and its shear.

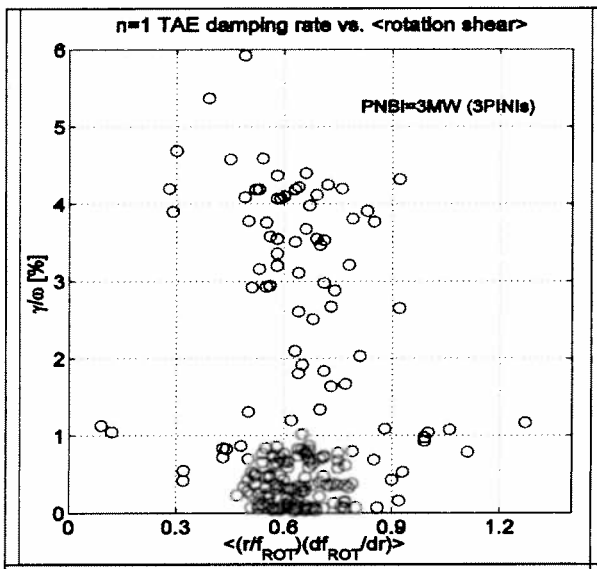

Figure 4a. Damping rate for n=1 TAEs as function of the volume-averaged rotation shear for P_{NBI}=3MW: note the large scatter in the values of γ/ω.

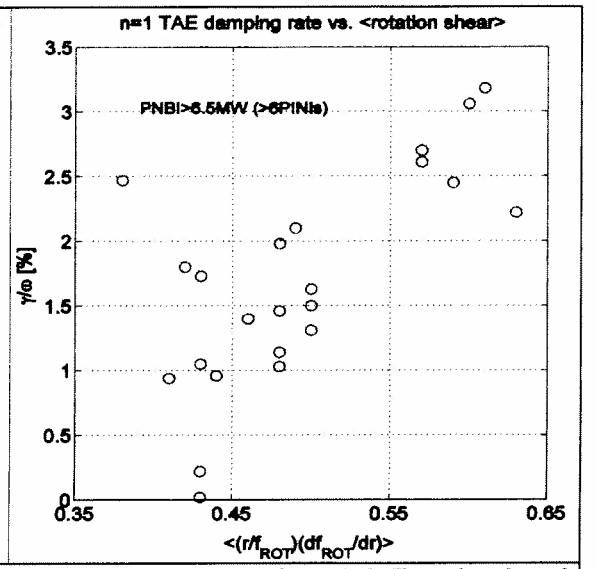

Figure 4b. Damping rate for n=1 TAEs as function of the volume-averaged rotation shear for P_{NBI}>6.5MW: here for high rotation shear γ/ω>2% always.

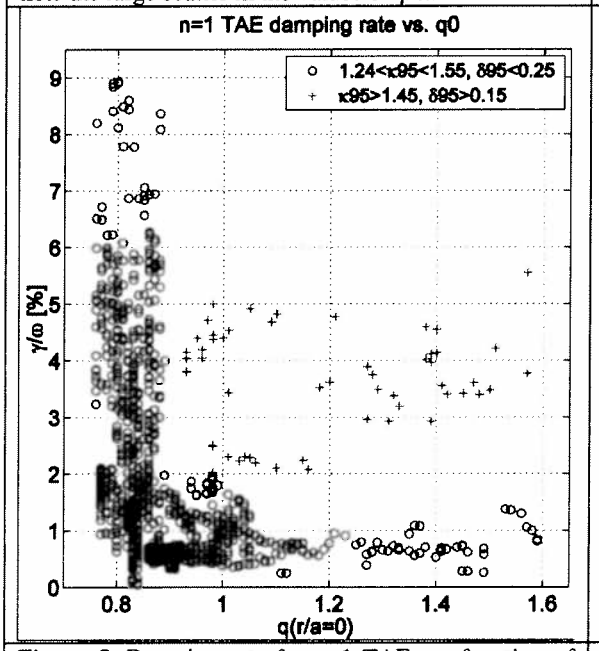

Figure 5. Damping rate for n=1 TAEs as function of q_0 in ohmic plasmas: we note that for q_0>1.1 a large γ/ω>2% is obtained only for κ_{95}>1.45 and δ_{95}>0.15.

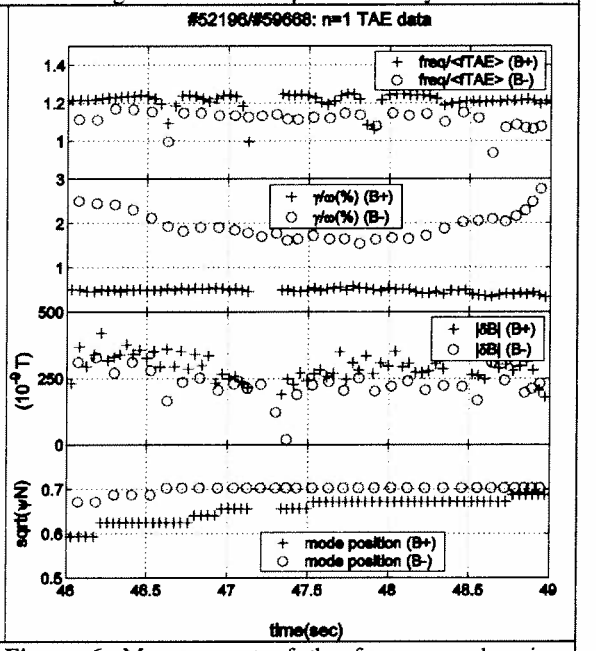

Figure 6. Measurement of the frequency, damping rate, mode amplitude and radial position for n=1 TAEs as function of the ion ∇B-drift direction.

Considering ohmic plasmas with κ_{95}<1.5 and δ_{95}<0.3, we find that for q_0>1.1 the damping rate of n=1 TAEs does not exceed the value $\gamma/\omega\approx$2% for a variety of electron density and temperature profiles and for different values of the plasma current and magnetic field, as shown in fig.5. Conversely, with q_0<0.9, we find that in the same experimental conditions γ/ω can reach values up to $\gamma/\omega\approx$8%. These observations indicate that very large values of the damping rate (γ/ω>2%) can only be obtained for q_0<1. Theoretical modelling is necessary to reproduce and provide an interpretation for this phenomenon. The transition between these two regimes, which is observed for $q_0\approx$0.9-1.1 is suggestive of a role for the sawteeth, either a

dynamical one associated to each individual sawtooth collapse, or an average effect of the sawteeth redistribution providing, on average, a lower core shear, favouring core damping via mode conversion [8].

The direction of the ion ∇B-drift is an important parameter in determining the accessibility conditions for the H-mode regime, with multi-machine experimental evidence that a lower additional heating power is required for the L-H mode transition when the ion ∇B-drift is directed towards the divertor [9]. It is thus important to study the implications of the choice on the ion ∇B-drift direction foreseen for ITER operation on the value of the background plasma damping of low-n TAEs. The data shown in fig.6 indicate that the damping rate of n=1 TAEs with similar frequency and radial location is approximately a factor three higher for the case of ion ∇B-drift directed away from the divertor, suggesting that low-n TAEs would have a much lower instability threshold in plasma configuration with the ion ∇B-drift directed towards the divertor [1].

After about ten years of operation, the 2004 JET experimental campaigns have been the last where the saddle coils have been used to drive and detect the damping rate of low-n TAEs. This experimental work has been useful in providing detailed benchmarks for the theoretical predictions of the TAE stability in ITER, see for instance Refs.[7,8,10,11]. In particular, we have demonstrated the role of the edge elongation, triangularity and magnetic shear in determining γ/ω for low-n TAEs [7], and we have measured the dependence of the damping rate on the bulk plasma beta [10] and normalised Larmor radius [11]. In this respect, the measurements reported here of the dependence of γ/ω for n=1 TAEs on the rotation shear, safety factor on axis and direction of the ion ∇B-drift represent the logic conclusion of our experimental effort on low-n TAEs. On the theoretical side, we have learnt that gyrokinetic codes provide for a better understanding of the damping rate of low-n TAEs, and particularly the dynamic scaling of γ/ω as function of various plasma parameters such as the edge plasma shape, the bulk plasma beta and the normalised ion Larmor radius, see for instance the results presented in Refs.[8,11]. However, it is also clear that a more systematic effort is needed for accurate predictions of TAE instabilities in ITER, and this work should start from the large database of low-n TAE data that we have collected so far, of which the data presented in this paper are a typical example. At the same time, the design and installation of the new high-n TAE antennas for JET represent the logic step forward towards a more detailed benchmarking of the existing models for high-n AEs in ITER regimes.

5. Outlook: the new JET antenna for the excitation of high-n AEs

The present antenna geometry limits the active AE excitation to low toroidal mode numbers, n=0-2, whereas intermediate or high n's characterise the most unstable AEs, which are already detected in JET and are similarly predicted for ITER. A direct excitation and tracking of the same modes is thus of clear interest for preparing the next step experiment. To this end, an antenna structure optimised for the excitation and detection of AEs with $n \approx 10\text{-}15$ has been designed and built, and it is being installed during the current JET shutdown [12].

The new antenna system comprises two assemblies of 4 toroidally spaced coils, situated at opposite toroidal locations. The static self-inductance of each new coil is $L \approx 25\mu H$, similar to that of the old antennas. Each coil is made using 18 turns of 4mm Inconel 718 wire, covers an extent of ~(25×25×15)cm, and is individually insulated from the supporting frame with Alumina-Oxide spacers. The first turn sits ~45mm behind the poloidal limiters. The coils are mounted on a 3mm-thick Inconel 625 open structure, to avoid a closed path for disruption-induced currents. A sketch of one set of four coils is shown in fig.7a. Figure 7b illustrates the integration of one set of four coils into the JET first wall.

The support scheme uses cantilevered brackets that connect to the remains of the saddle coils and "wing" brackets which add support to the top of the frame. These four attachment points are isolated with Shapal-M spacers and bypassed with straps of known resistance to provide a reliable current path, and hence optimise the mechanical load distribution. The frame is further protected by CFC tiles. Conservative estimates of the disruption currents in the MHD antennas and frame were used to calculate the loading and resulting stress in the antenna structure. The frame is designed as an open structure to break eddy current loops, computed assuming the antenna is shorted. The forces on the frame primarily result from halo currents entering around the mini limiters that now protect the coils. Initially, halo current loads were calculated assuming the full inventory of halo current crossed the toroidal field and passed downward the full height of the frame to the lower attachment points. This caused excessive forces at the saddle coil attachment points. To improve the loading, the attachment points were connected to their mounting locations through resistive straps which have their resistances sized to produce currents that minimise the net loading. With the addition of the resistive earth straps at the four attachment points, a small toroidal current crossed with the poloidal field component is added but the much larger loading due to poloidal currents crossed with toroidal field is hugely reduced. Figure 7c shows an example of the calculation of the mechanical loads and stresses in the antenna structure, due to halo currents during plasma disruptions, and, to a lesser extent, to disruption induced currents, in both cases crossed with the ambient magnetic field. Figure 7d shows a photo of the antenna frame, ready for the final coil assembly.

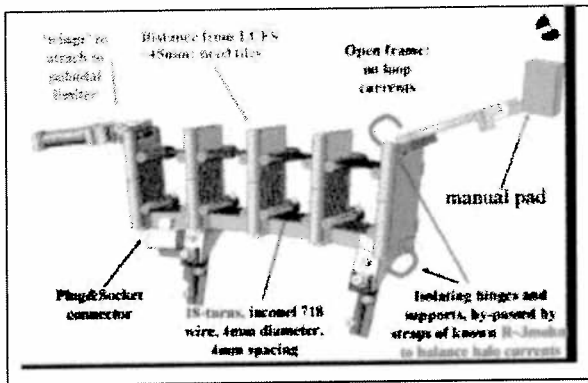

Figure 7a. Final design of the new TAE antennas.

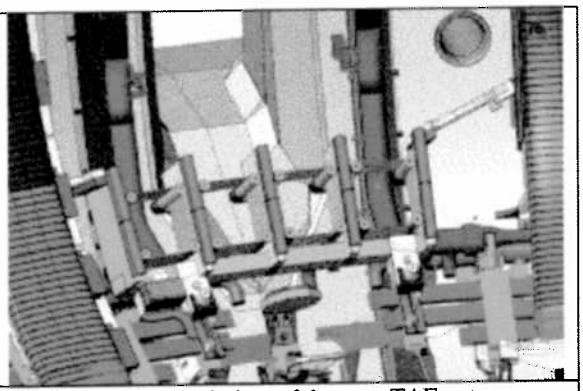

Figure 7b. In-vessel view of the new TAE antennas.

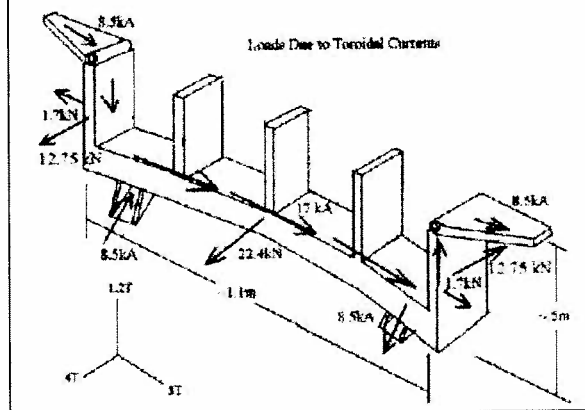

Figure 7c. Stress analysis of the new TAE antennas.

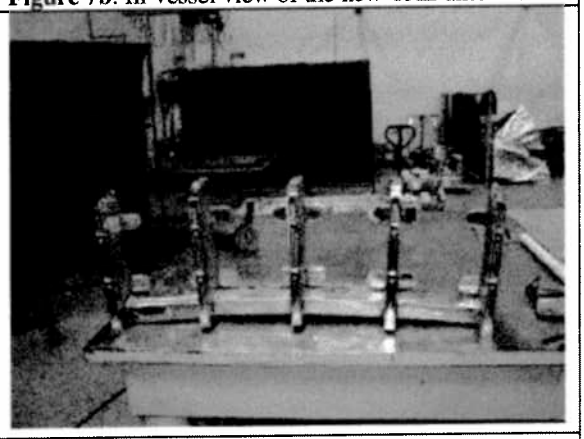

Figure 7d. One of the two antenna frames as built.

To comply with the "As Low As Reasonable Possible" system for manual in-vessel access, the new antennas will be almost entirely installed by Remote Handling (RH). Hence many components and jigs had to be specially designed to be compliant with the requirements of the RH installation. Detailed engineering work, the adaptable JET RH capabilities and

virtual reality models were used to develop the installation procedure. This has been recently successfully demonstrated in full mock-up trials, thus significantly reducing the engineering risks associated with the actual in-vessel installation.

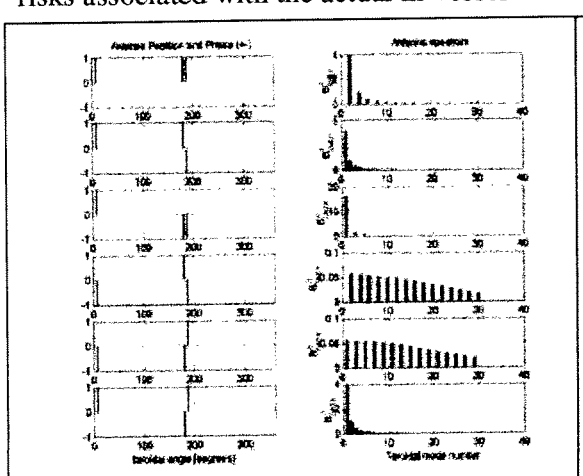

Figure 8a. Excited spectrum using 4 opposite coils.

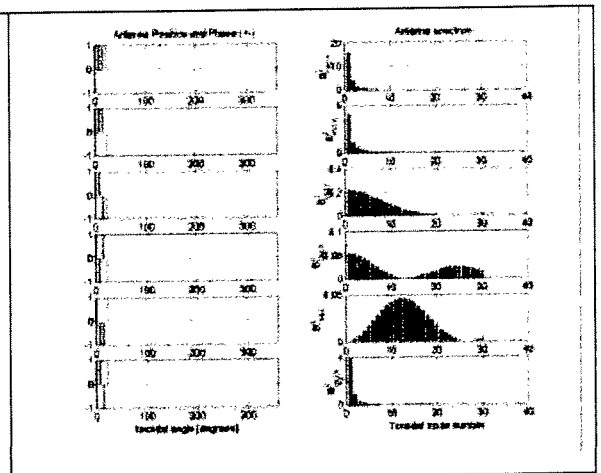

Figure 8b. Excited spectrum using 4 adjacent coils.

To simplify the ex-vessel installation, only four out of the eight antennas will be actively driven, and the four "passive" ones will be used as additional detectors, together with magnetic pick-up coils and internal measurements such as ECE and reflectometry. The maximum antenna current and voltage used for the AE excitation experiments are of the order of 10A and 700V, producing a very small antenna-driven magnetic field, $|\delta B/B| < 10^{-5}$. Any combination of 4 out of the 8 antennas will be chosen to excite different n-spectra, up to n~20, as shown in fig.8a and fig.8b.

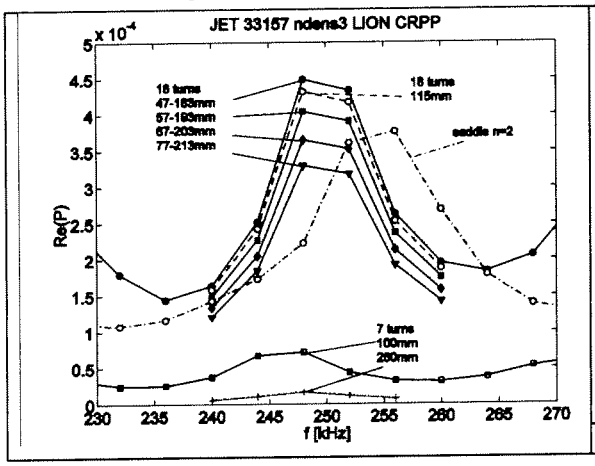

Code calculations also demonstrate that this arrangement provides a coupling to the plasma for a n=5 TAEs that is of the same order as that achieved with the present, much bigger, saddle coils for an n=2 TAE for the same JET equilibrium, as shown in fig.9. Thus, it is foreseen that the real-time tracking capabilities of the old saddle coil system will be maintained and, possibly, control of the marginal stability limit could be envisaged for the intermediate n-modes driven by the new antennas.

Figure 9. Calculated coupling for new TAE antennas.

This work has been conducted under the European Fusion Development Agreement. D.Testa and A.Fasoli were partly supported by the Fond National Suisse pour la Recherche Scientifique, Grant 620-062924. A.Fasoli, J.A.Snipes and P.Titus were partly supported by the US DoE Contract DE-FG02-99ER54563.

References

[1] D.Testa et al., PPCF **46** (2004), S59. [2] D.Testa et al., PoP **6** (1999), 3489; and D.Testa et al., PoP **6** (1999), 3498. [3] F.Rimini et al., NF **39** (1999), 1591. [4] A.Salmi et al., EPS 2004. [5] D.Ernst et al., PoP **7** (2000), 615. [6] A.Fasoli et al., PoP **7** (2000), 1816. [7] D.Testa et al., NF **41** (2001), 809. [8] A.Jaun et al., PPCF **43** (2001), A207; and A.Fasoli et al., PLA **265** (2000), 288. [9] W.Suttrop et al., PPCF **39** (1997), 2051. [10] D.Testa et al., NF **43** (2003), 724. [11] D.Testa et al., NF **43** (2003), 479. [12] A.Fasoli et al., IAEA-TCM on Energetic Particles, San Diego, USA, 6-8 October 2003; D.Testa et al., 23rd SOFT, Venice, Italy, 20-24 September 2004.

Anomalous particle and impurity transport in JET and implications for ITER

H. Weisen[1], C. Angioni[2], A. Bortolon[1], C. Bourdelle[4], L. Carraro[3], I. Coffey[5], R. Dux[2], I. Furno[6], X. Garbet[4], L. Garzotti[3], C. Giroud[5], H. Leggate[5], P. Mantica[7], D. Mazon[4], D. McDonald[5], M.F.F. Nave[8], R. Neu[2], V. Parail[5], M.E. Puiatti[3], K. Rantamäki[9], J. Rapp[10], J. Stober[2], T. Tala[9], M. Tokar[10], M. Valisa[3], M. Valovic[5], J. Weiland[11], L. Zabeo[5], A. Zabolotsky[1], K.-D. Zastrow[5] and JET-EFDA contributors

[1)]Centre de Recherches en Physique des Plasmas,
Association EURATOM - Confédération Suisse, EPFL, 1015 Lausanne, Switzerland
[2)]IPP Garching, Germany [3)]Consorzio RFX, Padova, Italy [4)]Association Euratom-CEA, CEA/DSM/DRFC CEA-Cadarache, France [5)]UKAEA, Abingdon, UK [6)]Los Alamos National Laboratory, USA [7)]IFP CNR Milano, Italy [8)]EURATOM-IST, Portugal [9)]EURATOM-Tekes, VTT, Finland [10)]IPP, Forschungszentrum Jülich, Germany
[11)]Chalmers University, Göteborg, Sweden
email of main author: henri.weisen@epfl.ch

Abstract: Results from an extensive database analysis of JET density profiles show that the density peaking factor $n_{e0}/\langle n_e \rangle$ in JET H-modes increases form near *1.2* at high collisionality to around *1.5* as the plasma collisionality decreases towards the values expected for ITER. This result confirms an earlier observation on AUG. The density peaking behaviour of L modes is remarkably different from that of H modes, scaling with overall plasma shear as $(n_{e0}/\langle n_e \rangle \propto l_i)$, independently of collisionality. H-mode density profiles show no shear dependence, except at the lowest collisionalities. No evidence for additional L_{Te}, L_{Ti}, T_e/T_i, β or ρ^* dependences has been obtained. Carbon and neon impurity density profiles from Charge Exchange Spectroscopy are less peaked than electron density profiles and usually flat in H modes. The possibility of heavy impurity accumulation at ITER collisionalities remains an issue. The peaking of the electron density profiles, together with the flatness of the light impurity density profiles, are favourable for fusion performance if they can be extrapolated to ignited conditions. Peaked density profiles would help to recover the fusion performance loss resulting from a possible lower-than-expected density limit in ITER.

1. Density profiles in ELMy H modes

Peaked electron and fuel density profiles in reactor plasmas provide the advantage of higher reactivity, higher bootstrap fraction and stronger electron-ion coupling in the core, than obtained with flat density profiles at the same average density, albeit at the risk of impurity accumulation in the core. Most importantly, they may allow a recovery of the thermonuclear power loss, which would result if the density limit in ITER [1] is as low as half of the Greenwald density limit, as expected from a recent analysis in AUG and JET [2]. Therefore the discovery of a clear collisionality dependence of density peaking in AUG [3] H-modes called for an independent verification in JET. The theoretically important effective collisionality defined as $\nu_{eff} = \nu_{ei}/\omega_{De} \sim 3(m_i/m_e)^{1/2}\varepsilon^{3/2}\nu^*_{ei}/q$ (assuming $k_\theta\rho = 1/3$), where ν_{ei} is the electron collision frequency and the curvature drift frequency ω_{De} is a rough estimate of the ITG growth rate, and is therefore expected to govern both anomalous diffusion and convection [3]. The collisionality dependence of the density peaking factors for a large representative set of stationary ELMy JET H modes and 'hybrid scenario H-modes' (which have moderate to

high q_{95} and low core magnetic shear) is shown in Fig.1. The density profiles were evaluated from the JET multichannel far infrared interferometer with the SVD-I inversion method [4], which uses basis function extracted from the LIDAR Thomson Scattering (TS) profiles, obtained by Singular Value Decomposition (SVD). This method greatly reduces errors in the LIDAR TS profiles, while granting consistency with interferometry. The collisionalities obtained on JET extend to below those expected for the ITER reference H-mode, indicated by a vertical line. The different symbols in Fig.1 refer to classes of internal inductance, which is a robust measure of overall magnetic shear. The same data are plotted versus l_i in Fig.2. There is no discernible dependence on l_i, except for $\nu_{eff} \leq 0.25$. This is in contrast to L-modes in DIII-D[5], TCV[6][7] and JET[8], where magnetic shear (or the peakedness of the current profile) was found to be the most important parameter, irrespective of collisionality.

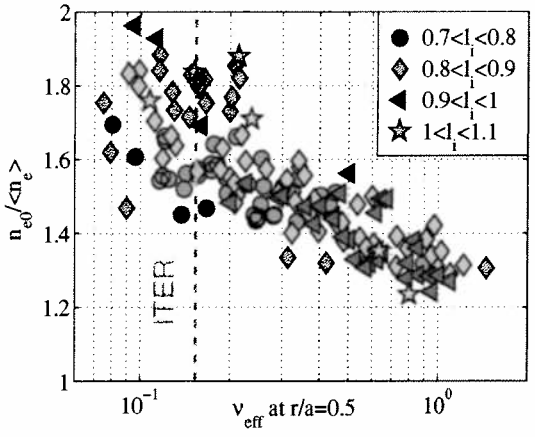

Fig. 1 Density peaking factor in H-mode versus ν_{eff} at r/a=0.5. Symbols: classes of internal inductance l_i.

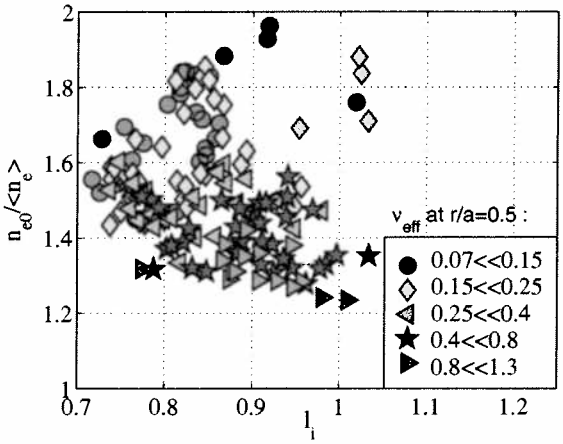

Fig. 2. Peaking factor in H-mode versus l_i, resolved by classes of effective collisionality ν_{eff}

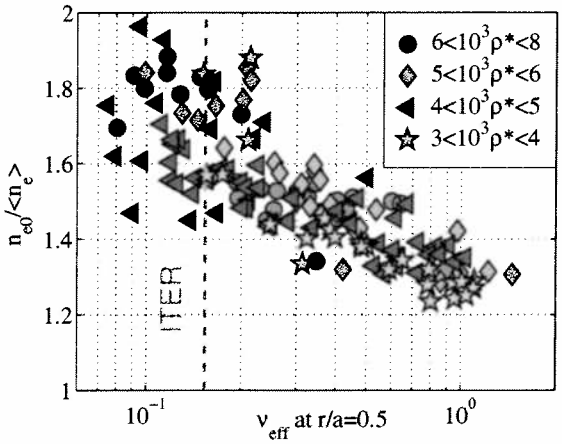

Fig. 3 Peaking factor in H-mode versus ν_{eff}, resolved by classes of ρ^* evaluated at r/a=0.5.

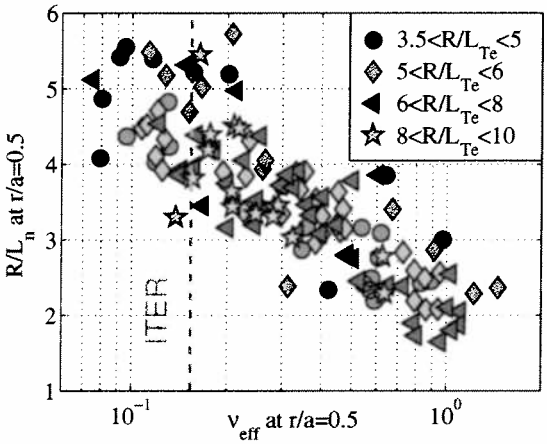

Fig. 4 Normalised electron density gradient in H-mode at r/a=0.5 versus ν_{eff}, resolved by classes of electron temperature gradient.

The data presented here contain a great variety of conditions with $1.7\times10^{19} \leq \langle n_e \rangle \leq 11\times10^{19} m^{-3}$, $3\times10^{-3} \leq \rho^* \leq 9\times10^{-3}$, $2.3 \leq q_{95} \leq 6.5$, $0.7 \leq \beta_N \leq 2.6$, $4 \leq R/L_{Te}(0.5) \leq 9$, $0.6 \leq T_e(0.5)/T_i(0.5) \leq 1.7$, $0.04 \leq V_{loop} \leq 0.55V$ and combinations of heating methods with $P_{nbi} \leq 17MW$, $P_{rf} \leq 10MW$, $P_{lhcd} \leq 3MW$, including a minority of cases with substantial ICRH heating (P_{ICRH}/P_{tot} in the range 0.4-0.9 and near central deposition r/a~0.3). We found no

additional dependence of peaking on $<n_e>$, nor on V_{loop}, P_{rf}/P_{tot}, β_N, ρ^*, T_e/T_i, L_{Te}, or L_{Ti}. Figs. 3&4 show the same data resolved into classes of ρ^*, and R/L_{Te}, evaluated at r/a=0.5, illustrating this lack of further dependences. In Fig.4, to offer an alternative representation, we characterise density peaking by $R/L_n=Rdln(n_e)/dr$ at mid-radius. The results also show that the Ware pinch cannot be held responsible for density peaking at low ν_{eff}, where the lowest values of V_{loop} are obtained. The latter statement is however in contradiction with JETTO modelling of three H mode discharges, one of which was at low collisionality, and which did not require an anomalous pinch larger than the Ware pinch [9]. Figures allowing a side-by-side comparison of JET and AUG results are available from ref [10]. The peaking is slightly higher (by ~0.1) at ν_{eff}~0.2 in JET than in AUG when the evaluation of ν_{eff} is based on the average Z_{eff} derived from visible Bremstrahlung (VB), as in Figs 1-4. JET results are however brought into full agreement with AUG when the hollow Z_{eff} profiles measured by CXS are used. Z_{eff} inferred from CXS at r/a=0.5 is typically lower by a factor 1.6 than Z_{eff} from VB, shifting the ν_{eff} axis by the same factor.

It has been suggested that the peaked density profiles observed at low collisionality may result from edge gas fuelling, rather than, as proposed here, from an anomalous pinch [11]. This conclusion, obtained using the FRANTIC code, is however disputed, because it is based on neutral flux calculations based on the total D_α emission, including the divertor, which produces 90% of the D_α light in the vessel. The idea that edge, or even beam fuelling may play an important role in shaping the density profile, is at odds with experimental observations. Fig.5 shows the peaking factor versus ν_{eff} resolved by line average density. The plasma density determines the mean free path for both the neutrals originating from edge fuelling and those injected by neutral beam heating. Penetration of edge neutrals occurs by a charge exchange (CX) chain, until the chain is terminated by an ionisation. For deuterium, the average chain length is $<\sigma v_{CX}>/<\sigma v_{ionisation}>$~4 for T_e in the keV range.

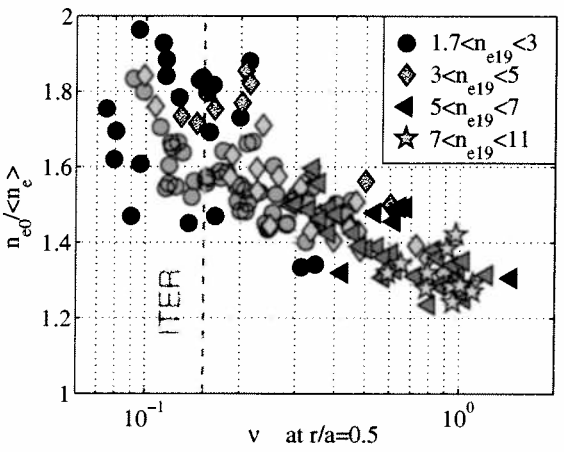

Fig. 5 As fig. 3, resolved by line average density.

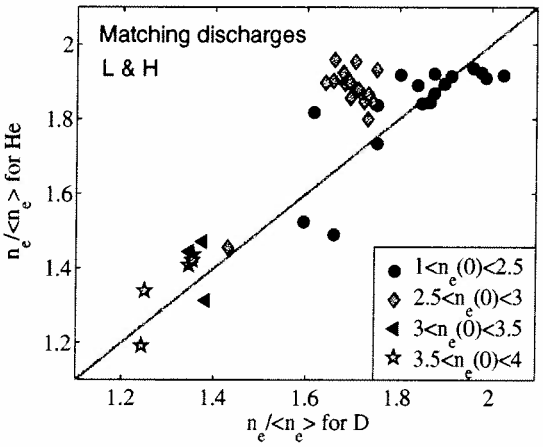

Fig. 6 Comparison of peaking factors in deuterium plasmas with their counterparts in He.

If density profiles were determined by the sole balance of the particle source and diffusion, they would only depend on the plasma density and the mixture of edge (shallow) and beam (deep) fuelling. We notice that a class of samples with $\bar{n}_e$~$4\times10^{19}m^{-3}$ (green diamonds) has peaking factors ranging from 1.3 to 1.8, in contradiction with the assumption of purely diffusive transport and a fixed source profile. We also note that in the interval $0.3<\nu_{eff}<0.4$, densities range from 2.5 to $6\times10^{19}m^{-3}$, yet they have the same peaking factor. Similarly, the flux of beam neutrals ($\propto P_{NBI}$) and its weight in the particle balance ($\propto P_{NBI}/<n_e>$) vary by a factor of four in this interval, without incidence on the density peaking factor. Corroborating evidence for the absence of source effects was obtained in a recent campaign using He as the

working gas, where He twins of previous D discharges were produced. He neutral penetration is strongly reduced by the low cross section for double CX, reducing the CX chain length by a factor of ~10 with respect to deuterium. Again, if edge neutral penetration mattered, He plasmas should be much flatter than their deuterium counterparts. As seen in fig.6, the density profiles in He plasmas are, if different at all, a hint more peaked in some cases. A third element stems from the comparison of AUG and JET. If neutral penetration mattered, density profiles in the smaller AUG device would, contrary to observation, be more peaked than those in JET.

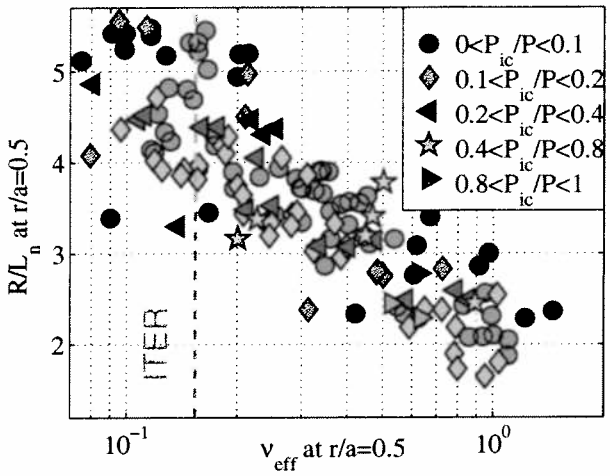

Fig. 7 H-mode density gradients resolved by fraction of ICRH heating power.

Central RF heating by ICRH and ECH has been observed to flatten the density profiles in TCV [7] and AUG [13][14]. In the latter it also led to a reduction of the central heavy impurity content. Two different mechanisms may concur to produce for this phenomenon. In the first, the pinch responsible for peaking is assumed to be the Ware pinch. The flattening is then attributed to a rise of particle diffusivity proportional to the rise in core heat diffusivity resulting from the additional heat flux [13]. The second mechanism, based on drift wave turbulence theory, attributes the peaking of the density profiles to anomalous pinches and their flattening in the presence of electron heating to the destabilisation of trapped electron modes (TEM), which produce a strong outward thermodiffusive particle convection counteracting the inward convection produced by the curvature pinch [3][14][15]. In the steady state density profile database presented here, there is no evidence for a significant effect of P_{ICRH} on electron density (fig.7). We note however that severe Ar impurity accumulation in Ar seeded discharges at high $\nu_{eff}(0.5)\sim1$ can lead to the development of highly peaked core density profiles and flat temperature profiles with $R/L_n\sim7$, $R/L_T\sim0$ for $r/a<0.4$ [16]. This evolution is now routinely prevented by the application of a few MW of centrally deposited ICRH. Electron heating experiments using ion Bernstein mode conversion heating in (non-seeded) H-modes have not shown any effect of the electron heating power on the density profiles. A GS2 [17] microstability analysis of these experiments, which exhibited a clear rise in $T_e(0)/\langle T_e\rangle$, but no change in $n_e(0)/\langle n_e\rangle$, showed that these plasmas remained in the ITG regime, possibly due to a lack of electron power. In the ITG regime only weak inward thermodiffusion is expected [3].

2. Fusion performance benefit from peaked density profiles

The potential fusion performance benefit from peaked density profiles is considerable, as shown in fig. 8. The figure plots the ratio of the expected thermonuclear yield calculated for thermal particles, using the measured density and temperature profiles to the same ratio, assuming a flat fuel density profiles with $n_e=n_e(0.9)$ and using the approximation $R_{DT}\sim n_D n_T T_i^2$, valid for $7<T_i<20$keV. The symbols refer to the Greenwald number N_G. The gain is nearly a factor 3, on average, for the ITER collisionality domain and nearly a factor 2 with respect to the weakly peaked plasmas at the high collisionality end. This advantage may however be entirely 'consumed' to compensate for a reduction of fusion performance, if the density limit is lower than expected.

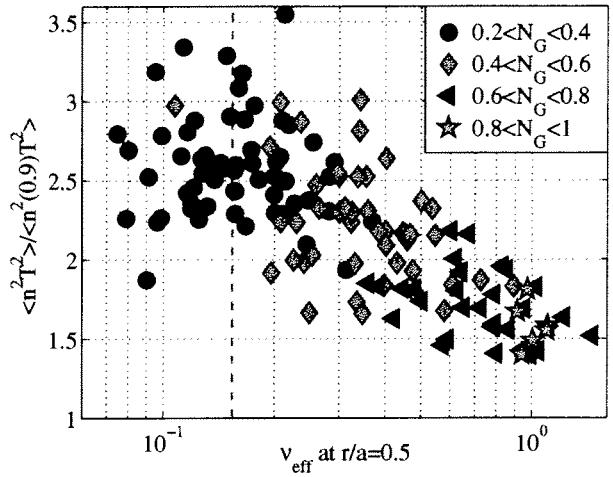

Fig. 8 Increase of expected thermonuclear yield over plasma with flat density profile clamped at $n_e(0.9)$.

The density limit has been related to the pedestal density in JET and AUG H-modes and has recently produced the alarming prediction that the density limit in ITER may be as low as half of the density of ITER reference H-mode [2]. If this lower limit (Borrass limit), rather than the Greenwald limit [18], applies to ITER, the loss in thermonuclear power would be at least a factor of two. This can be estimated, assuming $<n_eT_e> \propto \tau_E \propto <n_e>^{-0.4}$, as expected from ITERH.DB3 ELMy H-mode scaling [19]. The reduction will be more important still due to the unfavourable effect of the equipartition, as a result of which ions temperatures would lag significantly behind electron temperatures at low density. The gain from peaked density may compensate for the reduction of thermonuclear power that would result if the Borrass, rather than the Greenwald limit, applied to ITER. (Other caveats of low density operation, such the inability to achieve divertor detachment, are beyond the scope of this contribution).

3. Density profiles in L-modes

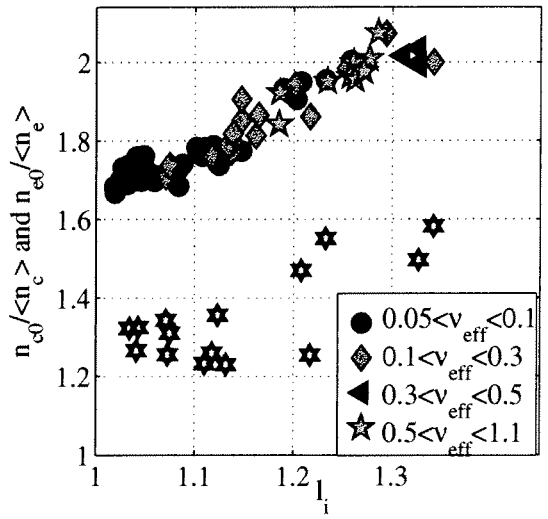

Fig. 9. Density peaking in LHCD L-modes versus internal inductance, resolved by effective collisionality at r/a=0.5. Stars: Carbon impurities.

In source-free MHD-quiescent L-mode plasmas with LHCD and with $q_0>1$, the density profile varies as $n_{e0}/\langle n_e \rangle \cong 1.6 l_i$, (fig.9, coloured symbols) independently of ν_{eff}. A range of $P_{LHCD} \leq 3.6MW$, deposited typically around $r/a \sim 0.4$, provided this scan of l_i at fixed $q_{95} \sim 8$. These experiments, reported in [8], have been reanalysed using the SVD-I method [4], showing that the peaking factor was previously underestimated by 25%. The density profiles remain peaked at $V_{loop}=0$ and negligible core particle source, as determined by KN1D [12], confirming investigations in fully current driven discharges in Tore Supra [20] and TCV [7]. As in the above H-modes, no dependence on L_{Te} was found. A GS2 analysis showed that the sign of the mode frequency is very sensitive to input parameters. This may indicate that the discharges are in a mixed ITG/TEM regime, where little or no anomalous thermodiffusion, and hence no L_{Te} dependence, is expected [14]. The l_i dependence is consistent with an anomalous pinch resulting from Turbulent EquiPartition [5]. Transport simulations using JETTO on a small number of L-mode discharges (not part of the above LHCD set) have also concluded that an anomalous pinch is present in L-modes [9].

4. Impurity density profiles and accumulation

Peaked density profiles, as found in many L-modes and in H-modes at low collisionality, raise the concern of neoclassical impurity accumulation, especially of the proposed ITER divertor material tungsten. Radial neoclassical impurity convection results from an inward term due to the main ion density gradient and an ion temperature gradient contribution which depends on the overall ion collisionality ν^*_{ib} (b stands for the background ions) [21] and may partly or fully counteract ('screen') the inward convection if $\nu^*_{ib}<1$, as expected for the ITER reference H-mode ($\nu^*_{ib}\sim0.4$ at r/a=0.5). For a heavy impurity in a hydrogen plasma with a typical light impurity concentration, the relevant background collisionality is dominated by that of the light impurities. In the current dataset, the possibility of some screening is limited to the lower end of the ν_{eff} range where $\nu^*_{i6}\sim1$ at r/a=0.5, calculated on the basis of the plasma deuterium and carbon content. At $\nu_{eff}>0.7$, $\nu^*_{i6}>3$ (typically), and the ion temperature gradient somewhat reinforces the inward convection [21]. Recent calculations using the Weiland model also show that anomalous inward convection, which scales as 1/Z, is lower for carbon than for deuterium.

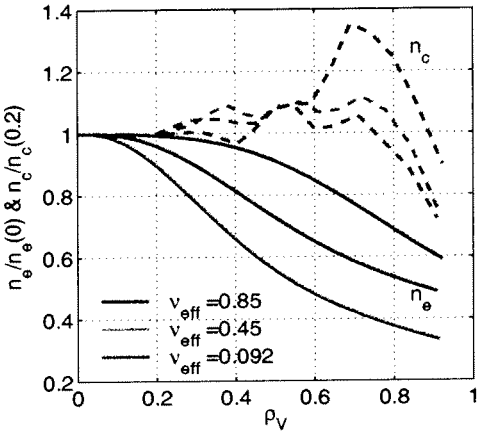

Fig. 10 Normalised H-mode electron (-) and carbon impurity density (--) profiles for three different ν_{eff} and $q_{95}\sim3$.

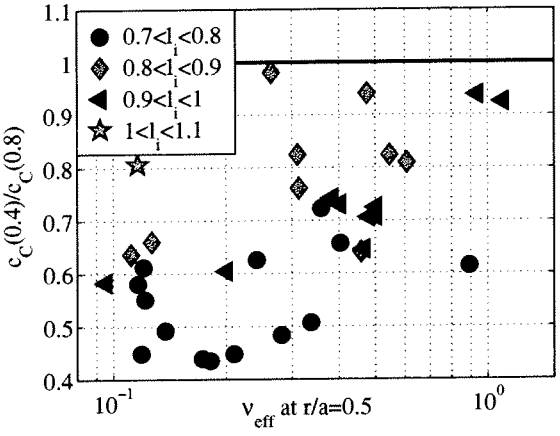

Fig. 11 Ratio of carbon concentrations at r/a=0.4 and 0.8 as function of ν_{eff} in H-modes.

Fig.9 shows that in L-mode, the carbon density profile from CXS, is significantly less peaked than the electron density profile. In H-mode, carbon density profiles are rather flat or slightly hollow, as seen for three examples with different collisionalities in fig.10. As a result, carbon concentration, n_c/n_e, profiles are hollow inside $r/a\sim0.7$, especially at low collisionality, when density profiles are most peaked (fig.11). Neon gas puff experiments in hybrid H-modes have provided transport coefficients such that v/D are similar to those of intrinsic carbon ($v_i/D_i=d/dn_i/dr$ in source free regions in steady state) [22]. The slight hollowness of light impurity density profiles exceeds theoretical expectations ($V\propto1/Z$) and raises the question wether NC ion temperature screening may contribute. This appears to be impossible in view of the high diffusion coefficients (D~1-4m^2/s, two orders of magnitude beyond NC) obtained for Ne and Ar in the confinement region [22]. The complex structure and large magnitude of the convective velocity in impurity transport simulations [22][23] is also at odds with NC theory.
Ar seeding has been used in high density discharges to simultaneously obtain high density, good confinement and an edge radiation belt. Ar in these H-mode discharges, which had $\nu_{eff}>0.6$ and $\nu^*_{i6}>3$, was prone to a process of slow, but severe, central accumulation, often developing highly peaked electron and Ar densities and high core radiation losses, especially at low triangularity [16][23][24]. These radiation losses and lack of net heating power in the core led to core shear reversal with $q_{min}>1$ and the suppression of sawteeth, thereby worsening the accumulation. A few MW of central ICRH was sufficient for maintaining sawteeth (or

sometimes a (1,1) MHD mode), for flattening the core electron and Ar density profiles, allowing access to stationary high performance discharges [16].

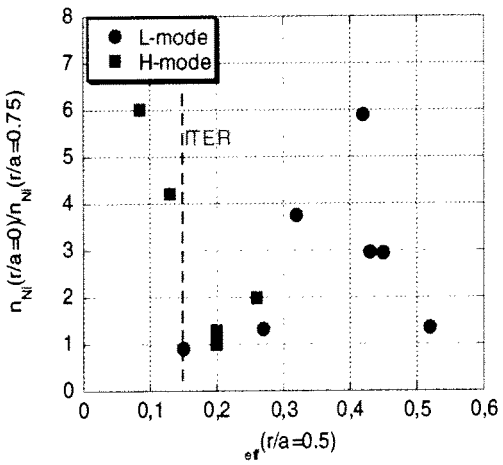

Fig. 12 Peaking of laser-ablated Nickel density profiles (transient).

Results for laser ablated, transient Ni injection are shown in fig.12. The figure shows peaking factors extrapolated to steady state, as deduced from X-ray measurements and modelled using an ionisation equilibrium code to provide radially resolved transport parameters. Steady-state profiles were then reconstructed from v(r) and D(r), assuming a constant edge source. Some of these are considerably more peaked than the electron density profiles, with most of the impurities concentrated near the magnetic axis, inside r/a<0.25, while outside this region, Ni concentrations were constant. In the confinement zone, Ni diffusion coefficients in H-mode ($1<D<4 m^2/s$, depending on the discharge) and L-mode ($2<D<7 m^2/s$) were clearly anomalous and much lower towards the axis and near the edge in H-mode. These observations, as others (e.g.[25]), support the view that in the core, where anomalous transport is low in the absence of sawteeth, heavy impurity transport is dominated by NC processes. In particular, the observation that Ni profiles can be strongly peaked in the core at low ν_{eff}, reinforces our concerns about tungsten accumulation in ITER.

5. Discussion and summary.

The above observations pose welcome constraints on the theoretical understanding and on ongoing modelling efforts. Some observations can be related to existing theories. The ν_{eff} dependence in H-modes, which are largely in the ITG regime, is in agreement with fluid modelling [3]. Positive shear L-modes and H-modes at low ν_{eff} have profiles which are consistent with Turbulent EquiPartition [5], as expected from purely diffusive transport of trapped particles in poloidal flux space, i.e $\Delta N/\Delta \Psi$ ~constant (where ΔN is the number of particles in the interval $\Delta \Psi$) over most of the cross section. A theoretical difficulty is the existence of peaked density profiles at high ν_{eff} in L-modes, while, for high values of ν_{eff}, H-mode profiles are much flatter. Another difficulty is to understand why there is no evidence for a shear dependence for H-modes at $\nu_{eff}>0.2$, despite the expectance that the curvature pinch is the dominant convective mechanism when ITG's dominate [14].

It seems reasonable to assume that the differences are somehow linked to the nature of the underlying turbulence (ITG or TEM). The fundamental difference between L and H-modes is the edge pedestal, which appears to lead to flatter core density profiles, which is stabilising TEMs and destabilising for ITGs. At $\nu_{eff}<0.2$, however, the significant density gradient in H-mode would reduce ITG growth rates and contribute to destabilising TEMs, which may explain why a shear dependence similar to that of L-modes is observed. (Recent observations in TCV and AUG also suggest that the domains where scaling with ν_{eff}, respectively shear, is observed do not coincide neatly with the H and L-mode regimes). The L-modes reported above appear to be in a mixed ITG/TEM regime, not however dominated by TEMs, as can be produced in devices equipped with high power electron heating such as TCV and AUG, where density profiles have been observed to flatten in response to central electron heating [13][20][14].

The agreement between JET and AUG, together with the lack of significant dependencies on dimensionless parameters other than ν_{eff} (and l_i at the lowest ν_{eff}), suggests that an extrapolation to ITER H-modes should be possible. Assuming otherwise similar conditions, we expect $n_{e0}/\langle n_e \rangle \approx 1.5 \pm 0.2$ for the collisionality of the ITER reference H-mode, corresponding to $R/L_n \approx 4 \pm 1$ at mid-radius. We expect this prediction to apply to the initial, non-active phase of operation when hydrogen or helium will be used as working gases. This peaking would also imply a boost in thermonuclear fusion yield of nearly a factor of 3 over a flat density profile with density clamped at r/a=0.9. This may compensate for a possible lower density limit in ITER [2]. Extrapolation to ignited conditions is uncertain, because the large electron heating power deposited in the core by α-particles may destabilise TEMs, leading to flatter density profiles. A positive effect may however be a concomitant reduction of the core impurity content. The amount of net electron heating and their effect on TEMs will however be reduced by electron-ion coupling, for which smaller devices with high local electron heating power densities are not necessarily representative. The non-observation, so far, of density flattening in JET should not be taken as an indication that the phenomenon disappears in large enough devices, since it may be also due to a lack of electron heating power available in JET. The issue calls for dedicated experiments at low ν_{eff}, where the central electron heating is tailored as to emulate the net electron heating profile in ITER.

Acknowledgement: This work was partly supported by the Swiss *Fonds National de la Recherche Scientifique*.

References

[1] V. MUKHOVATOV et al, Plasma Phys. Contr. Fusion **45** (2003) A235
[2] K. BORRASS et al., Nuclear Fusion **44** (2004) 752
[3] C. ANGIONI et al, Phys. Rev. Lett. **90** (2003) 205003
[4] I. FURNO et al, Plasma Phys. Contr. Fusion **46** (2004), accepted, due Dec. 2004
[5] D.R. BAKER et al, Nuclear Fusion **40** (2000) 1003
[6] H. WEISEN et al, Nuclear Fusion **42** (2002) 136
[7]A. ZABOLOTSKY et al, Plasma Phys. Contr. Fusion **45** (2003) 735
[8] H. WEISEN et al, Plasma Phys. Contr. Fusion **46** (2004) 751
[9]L. GARZOTTI et al, Nucl. Fusion **43** (2003) 1829
[10] X. GARBET et al (2004), accepted for Plasma Phys. Contr. Fusion (invited EPS 2004)
[11] M. VALOVIC et al, 2004, accepted for Plasma Phys. Contr. Fusion
[12] B. LABOMBARD, MIT PSFC report **PSFC-RR-01-03** (2001)
[13] J. STOBER et al., Nuclear Fusion **41** (2001) 1535
[14] C. ANGIONI et al, Nuclear Fusion **44** (2004) 827
[15]X. GARBET et al, Phys. Rev. Lett. **91** (2003) 35001
[16] M.F.F. NAVE et al, Nuclear Fusion **43** (2003) 1204
[17] M. KOTSCHENREUTHER et al, Comput. Phys. Commun. **88** (1995) 128
[18] M. GREENWALD et al, Nucl. Fusion **28** (1988) 2199
[19] ITER EXPERT GROUPS et al, ITER Physics Basis, chap 2, Nucl. Fusion **39** (1999) 2175
[20] G.T. HOANG et al, Phys. Rev. Lett. **90** (2003) 155002
[21]S.P. HIRSHMAN AND D.J. SIGMAR, Nuclear Fusion **21** (1981) 1079
[22] C. GIROUD et al, 31st EPS on Plasma Physics, London (2004) P1.144
[23] M.E. PUIATTI et al, Plasma Phys. Contr. Fusion **45** (2003) 2011
[24] M.Z. TOKAR et al, Nucl. Fusion **37** (1997) 1691
[25]R. DUX, Fusion Science and Technology **44** (2003) FST-11 276903